AWARD NUMBER: W81XWH-19-1-0428

TITLE: Genetically Dissecting Basal Forebrain Circuits Underlying Eating Disorders

PRINCIPAL INVESTIGATOR: Benjamin Arenkiel

CONTRACTING ORGANIZATION: Baylor College of Medicine, Houston, TX

REPORT DATE: October 2021

TYPE OF REPORT: Annual report

PREPARED FOR: U.S. Army Medical Research and Materiel Command
Fort Detrick, Maryland 21702-5012

DISTRIBUTION STATEMENT: Approved for Public Release;
Distribution Unlimited

The views, opinions and/or findings contained in this report are those of the author(s) and should not be construed as an official Department of the Army position, policy or decision unless so designated by other documentation.

REPORT DOCUMENTATION PAGE

Form Approved
OMB No. 0704-0188

Public reporting burden for this collection of information is estimated to average 1 hour per response, including the time for reviewing instructions, searching existing data sources, gathering and maintaining the data needed, and completing and reviewing this collection of information. Send comments regarding this burden estimate or any other aspect of this collection of information, including suggestions for reducing this burden to Department of Defense, Washington Headquarters Services, Directorate for Information Operations and Reports (0704-0188), 1215 Jefferson Davis Highway, Suite 1204, Arlington, VA 22202-4302. Respondents should be aware that notwithstanding any other provision of law, no person shall be subject to any penalty for failing to comply with a collection of information if it does not display a currently valid OMB control number. **PLEASE DO NOT RETURN YOUR FORM TO THE ABOVE ADDRESS.**

1. REPORT DATE	2. REPORT TYPE	3. DATES COVERED
October 2021	Annual report	01Sep2020-31Aug2021

4. TITLE AND SUBTITLE

Genetically Dissecting Basal Forebrain Circuits Underlying Eating Disorders

5a. CONTRACT NUMBER
W81XWH-19-1-0428

5b. GRANT NUMBER
W81XWH-19-1-0428

5c. PROGRAM ELEMENT NUMBER
N/A

6. AUTHOR(S)

Arenkiel, Benjamin R., Ph.D.

5d. PROJECT NUMBER
0011327909

5e. TASK NUMBER
N/A

5f. WORK UNIT NUMBER
N/A

7. PERFORMING ORGANIZATION NAME(S) AND ADDRESS(ES)

Baylor College of Medicine
One Baylor Plaza
Houston, TX 77030

8. PERFORMING ORGANIZATION REPORT NUMBER
N/A

9. SPONSORING / MONITORING AGENCY NAME(S) AND ADDRESS(ES)
U.S. Army Medical Research and Materiel Command
Fort Detrick, Maryland 21702-5012

10. SPONSOR/MONITOR'S ACRONYM(S)
CDMRP

11. SPONSOR/MONITOR'S REPORT NUMBER(S)
N/A

12. DISTRIBUTION / AVAILABILITY STATEMENT

Approved for Public Release; Distribution Unlimited

13. SUPPLEMENTARY NOTES
None.

14. ABSTRACT

Abnormal eating habits that drive excessive food seeking- or avoidance, can manifest as health-threatening and socially impactful eating disorders. We have previously reported a potent role for basal forebrain cholinergic neurons in regulating feeding behavior, and recently discovered that cell type-specific manipulations of their immediate downstream targets, i.e. Glutamatergic (Glu+) neurons, are capable of directly toggling a spectrum of eating-associated behaviors that range from increased food seeking and excessive food consumption to severe hypophagia, overt food avoidance, and starvation. Continuing on the achievements in the previous report, we have accomplished experiments showing that Glu+ neurons are direct downstream target of cholinergic neurons, the cholinergic receptor types on the Glu+ neurons, Glu+ neuron responses to a variety of external cues including food odors, and potent inhibition on feeding behaviors by activation of Glu+ neurons. In addition, we have also made significant progress in other goals including experiments aimed at testing the effects of loss of function of forebrain Glu+ neurons, the roles of LH neurons in mediating the action of forebrain Glu+ neurons in feeding behaviors, as well as the effect of the forebrain Glu+ neurons on obesity from leptin deficiency, all of which have laid a solid foundation for the planned goals in year 3. Our discoveries to date provide intriguing insight into a previously unknown circuit that links the cholinergic basal forebrain, which is known for its role in attention, wakefulness, and sensory processing, to value based components of eating. Experiments designed in this award will elucidate the mechanisms by which basal forebrain circuits govern food seeking and/or food aversion.

15. SUBJECT TERMS
Basal forebrain, eating disorder, glutamate, acetylcholine, lateral hypothalamus, optogenetics, in vivo Ca2+ imaging, metabolism

16. SECURITY CLASSIFICATION OF:			17. LIMITATION OF ABSTRACT	18. NUMBER OF PAGES	19a. NAME OF RESPONSIBLE PERSON
Unclassified					USAMRMC
a. REPORT	b. ABSTRACT	c. THIS PAGE			19b. TELEPHONE NUMBER *(include area code)*
Unclassified	Unclassified	Unclassified	Unclassified	56	

TABLE OF CONTENTS

	Page
1. Introduction	1
2. Keywords	1
3. Accomplishments	1-5
4. Impact	6
5. Changes/Problems	6
6. Products	6
7. Participants & Other Collaborating Organizations	7
8. Special Reporting Requirements	8
9. Appendices	8

INTRODUCTION

Abnormal eating habits that drive excessive food seeking- or avoidance can manifest as health-threatening and socially impactful eating disorders. To date, studies investigating the neural contribution to eating habits and body weight control have focused largely on neuropeptidergic signaling in the hypothalamus, a key brain region involved in feeding behavior. Although signaling from extra-hypothalamic brain regions has also been implicated in regulating nutrient metabolism, appetite, and satiety, it is unclear which brain regions and pathways are involved. We previously found that cholinergic (ACh+) neurons within the basal forebrain make synaptic connections onto neighboring glutamatergic (Glu+) projection neurons, which in turn directly govern feeding behavior. Our preliminary data identify prominent targets of basal forebrain Glu+ neurons within the lateral hypothalamus, an area associated with feeding, reward processing, and addiction. Based on these findings, we aim to test whether basal forebrain glutamatergic projection neurons serve as a primary circuit node to govern eating-related behaviors. The scope of research includes 3 main aims: 1) to determine how basal forebrain ACh+ and Glu+ neurons are connected; 2) to determine how Glu+ neurons in the basal forebrain influence feeding behavior; and 3) to identify downstream targets of basal forebrain Glu+ neurons that govern feeding behavior. The results of the supported work will provide insights on how basal forebrain ACh+ and Glu+ neurons are connected, how Glu+ neurons in the basal forebrain influence feeding behavior and related behaviors and identify the downstream targets that mediate basal forebrain Glu+ neurons in regulating eating and related behaviors.

Specifically for this report period, we have accomplished the major goals planned for this period. Regarding completion of major goals stated from the onset of the proposed research, we have made significant progress towards accomplishing major goals associated with major goals 1-6, and have also made significant progress towards the other remaining major goals.

KEYWORDS

Basal forebrain, eating disorder, glutamate, acetylcholine, lateral hypothalamus, optogenetics, in vivo Ca2+ imaging, metabolism

ACCOMPLISHMENTS

Major goals

Major goal 1: identify subtypes of basal forebrain neurons responding to eating; SOW completion date and site: 1-12 months in Site 1 (Dr. Arenkiel). This goal has been accomplished 1-12 months and included in the last report.

Major goal 2: map local inputs onto basal forebrain Glu+ neurons; SOW completion data and site: 3-12 months in Site 2 (Dr. Tong). This goal has been delayed because of unavailability of SAD rabies virus during the pandemic. We have generated the required animal models and the rabies virus has just recently arrived, and we will resume the experiment immediately. This goal will be accomplished 1-24 months.

Major goal 3: Profile Ach receptor expression in basal forebrain Glu+ neurons; SOW completion data and site: 1-12 months in Site 1 (Dr. Arenkiel). This goal has been partially accomplished. Initial expression analysis has been conducted using FISH, but we are still confirming basal forebrain cell types of expression. This has been delayed due to the pandemic, but is currently underway.

Major goal 4: Decipher the nature of neurotransmitter between basal forebrain Ach+ neurons and Glu+ neurons; SOW completion date and site: 3-12 months in Site 1 (Dr. Arenkiel). This goal has been accomplished 3-12 months and included in the last report.

Major goal 5: Image basal forebrain Glu+ neurons *in vivo* responses to eating; SOW completion data and site: 6-20 months in Site 1 (Dr. Arenkiel). This goal has been accomplished 6-20 months

Major goal 6: Modulate basal forebrain Glu+ neuron activity and assess impact on feeding and physiology; SOW completion date and site: 6-24 months and Site 2 (Dr. Tong). This goal has been accomplished 6-24 months.

Major goal 7: Inhibition of basal forebrain Glu+ neurons and impact on feeding; SOW completion date and site: 12-28 months and both Sites 1 and 2 (Drs. Arenkiel and Tong). This goal has been accomplished 60%, and is currently a focus of our efforts.

Major goal 8: Modulate basal forebrain Glu+ neuron activity and assess feeding; SOW completion date and site: 12-28 months and Site 2 (Dr. Tong). This goal has accomplished 50%, and is currently underway.

Major goal 9: Evaluate roles for basal forebrain Glu+ neurons mediating the action of Ach+ neurons in feeding regulation and body weight; SOW complete date and site: 12-36 months and Site 2 (Dr. Tong). This goal has been accomplished 20%.

Major goal 10: Genetic rescue of obesity; SOW completion date and site: 6-36 months and Site 1 (Dr. Arenkiel). This goal has been accomplished approximately 50%.

Major goal 11: Evaluate downstream targets of basal forebrain Glu+ neurons that govern feeding behavior; SOW completion date and site: 18-36 months and both Sites 1 and 2 (Drs. Arenkiel and Tong). This goal has been accomplished 20%, and is currently a primary focus of both labs.

Major goal 12: Decipher basal forebrain Glu+ neuron to LH neuron projection in feeding motivation; SOW completion date and site: 12-30 months and Site 2 (Dr. Tong). This goal has been accomplished 30%, and is currently underway.

Major goal 13: Determine whether LH Glu+ neurons are directly downstream of basal forebrain Glu+ neurons; SOW completion date and stie: 6-18 months and Site 1 (Dr. Arenkiel). This goal has been accomplished (6-18 months).

Major goal 14: Determine whether LH Glu+ neurons mediate the effect of basal forebrain Glu+ neurons in feeding regulation; SOW completion date and site: 6-36 months and Site 2 (Dr. Tong). This goal has been accomplished approximately 20%.

Accomplishment during the reporting period:

In the previous report, we have accomplished major goals 1 and 4. During the reporting period, we have accomplished major goals 2-3 and 5-6, and also made significant progress in major goals 7-8, and 10.

Major goal 2 (Dr. Tong): Here the goal is to determine whether ChAT neurons in the basal forebrain send monosynaptic projections to Glu+ neurons. We plan to use monosynaptic pseudotyped rabies viral approach to trace monosynaptic upstream neurons. Toward this, we have prepared *Vglut2-Cre* models, in which AAV-Flex-TVA-mCherry and AAV-Flex-G viral vectors will be injected into the basal forebrains of these mice. One week later, SADdeltaG-GFP virus will be injected to the same location. Two

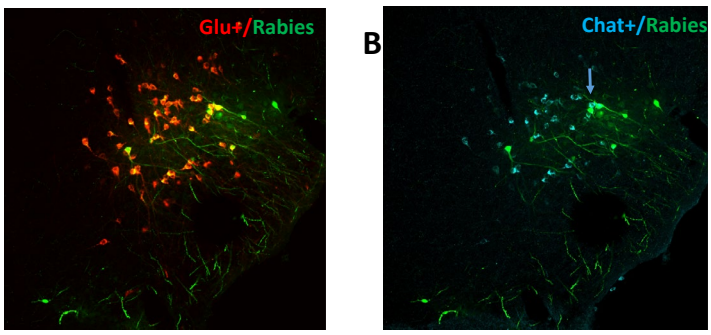


Fig. 1

weeks later, mice will be perfused to document the viral expression. However, due to the pandemic, the viral core for the pseudotyped rabies virus SADdeltaG-GFP had been shut down and the experiments had to be delayed from year 1 to year 2. We have accomplished this experiment in year 2 (Fig. 1, arrow identifies ChAT+ neurons positive for rabies viral expression). However, we only found a limited number of neurons that are presynaptically traced. The low efficiency of this pseudorabies monosynaptic viral tracing has been reported previously. We just learned a new method based on the tracing ability of heavy chain of tetanus toxin for much more effective tracing from neuromodulatory cell types, and we will use this method to confirm the pseudotyped rabies virus tracing.

Major goal 3 (Dr. Arenkiel): Here the goal is to analyze ACH receptors in basal forebrain Glu+ neurons. Toward this, RNA probes have been synthesized, tested for efficacy, and initial expression analysis has been completed. Due to the shutdown we are now just resuming further experimentation to validate the cell type-specific patterns of AChR expression. New approaches towards single cell sequencing of basal forebrain material is currently underway.

Major goal 5 (Dr. Arenkiel): Here the goal is to determine the *in vivo* responses of basal forebrain Glu+ neurons to fed, fasting, and food-related odors. We have prepared *Vglut2-Cre* mice, delivered AAV-Flex-GCamP6m virus, and successfully implanted GRIN lenses into these animals. We have observed that GCamp6m signaling in the forebrain region responded to various external signals (Fig. 2A, traces for Butryric Acid and 2-Methylbutylamine) and found that, interestingly, these neurons responded to different food-related odors, but not to the mineral oil control (Fig. 2A, food odor versus mineral oil). These responses were rapid and reversable (Fig. 2B), suggesting a direct relevance of these neurons to feeding. This goal has been accomplished within the set time frame.

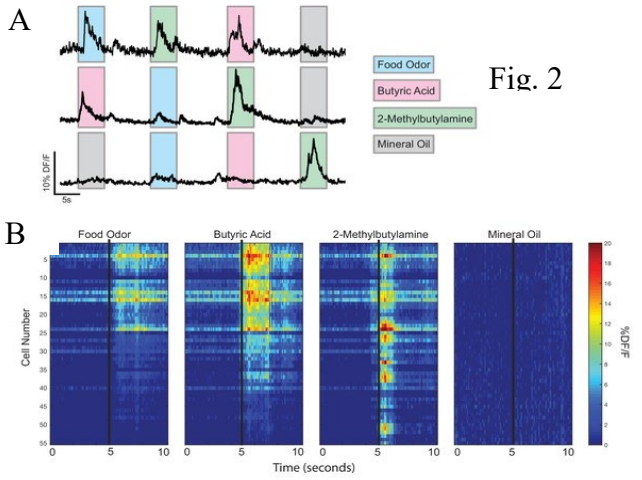


Fig. 2

Major goal 6 (Dr. Tong): Here the goal is to determine feeding and body weight in mice with basal forebrain Glu+ neurons expressing NaChBac. In the last report, we have prepared *Vglut2-Cre* mice and delivered AAV-Flex-NaChBac virus or control GFP virus to the basal forebrain (Fig. 3A). We found that NaChBac injected mice exhibited rapid body weight reduction (Fig. 3B and 3C), due to dramatic reduction of feeding (Fig. 3C).

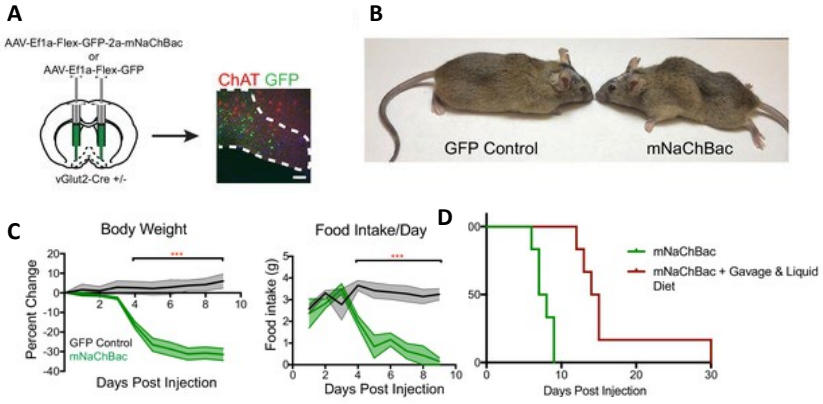


Fig. 3

The remaining experiments in this major goal are to test whether reduced food intake and associated reduced body weight can be rescued by forced feeding with food gavage. We found that by liquid food gavage, the survival rate of the animal with NaChBac expression was significantly improved, but was not fully rescued (Fig. 3D). This goal has been accomplished within the planned time frame.

Major goal 7 (Drs. Arenkiel and Tong): Here we seek to determine the effect of loss of function of basal forebrain Glu+ neurons on feeding (Dr. Arenkiel) and energy expenditure (Dr. Tong) by eliminating neurotransmitter release via expression of tetanus toxin light chain (TeNT). AAV-Flex-TeNT-p2A-GFP virus has been delivered to the forebrains of *Vglut2-Cre* mice, and we monitored feeding and body weight. However, we did not observe obvious differences in feeding, body weight, or O2 consumption and/or locomotion.

Ongoing efforts are focused on verification of injection and expression, and confirmation of TeNT achieving loss of Glu release. It is projected that the specified goal will be accomplished within the planned time frame.

Major goal 8 (Dr. Tong): Here we set out to determine effects on feeding via manipulation of forebrain Glu+ neurons activated with ChR2 or inhibited with eNpHR3.0. Towards this, we delivered AAV-Flex-ChR2-GFP virus to the forebrains of *Vglut2-Cre* mice, and at the same time implanted optic fibers. We found that delivery of blue light significantly reduced fasting-induced refeeding (Fig. 4), suggesting an importance of forebrain Glu+ neurons in feeding control. However, when we delivered AAV-Flex-eNpHR3.0 virus to the same neurons with light stimulation, we failed to observe significant effects on fasting refeeding. Currently, we are verifying the anatomy of accurate delivery and expression of the virus, as well as the effect of light delivery. It is estimated that we will accomplish the planned goal within the set time frame.

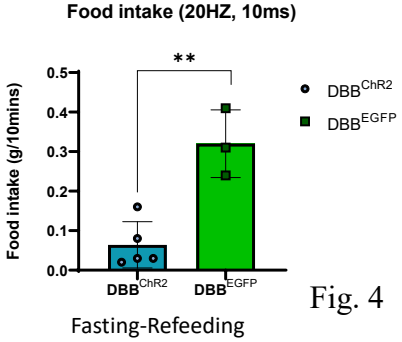


Fig. 4

Major goal 9 (Dr. Tong): Here the goal is to determine whether basal forebrain Glu+ neurons mediate the action of ACh+ neurons in feeding and body weight. Towards this, we have crossed *ChAT-Cre* mice with *Vglut2-Flp* mice to obtain *ChAT-Cre::Vglut2-Flp* models, in which we delivered AAV-Flex-ChR2-GFP and AAV-fDIO-hM4Di-mCherry, or control AAV-fDIO-mCherry viruses to the forebrain. Future experiments are planned to evaluate effects of light stimulation on feeding with or without CNO administration. It is estimated that these experiments can be accomplished within the planned time frame.

Major goal 10 (Dr. Arenkiel): Here the goal is to determine whether hypophagia by basal forebrain Glu+ neuron activation can rescue the ob/ob obesity. *Vglut2-Cre*::ob/ob mice have been generated and the AAV-Flex-NaChBac-GFP or control AAV-Flex-GFP virus has been delivered to the basal forebrain region of some of these mice. Experiments are planned to measure weekly body weight and feeding of these mice. It is estimated that the milestone in this goal will be met within the planned time window.

Major goal 11 (Drs. Arenkiel and Tong): Here the goal is to determine whether LH functions as a key downstream target that mediates hypophagia (Dr. Arenkiel) or aversion (Dr. Tong) induced by forebrain Glu+ neuron activation. Stereotaxic surgery has been performed to deliver AAV-Flex-ChR2 virus to the forebrains of *Vglut2-Cre* mice and at the same time, optic fibers implantation at the LH. The mice that received surgery are ready to be assayed for feeding or place preference with light delivery to the LH. It is estimated that this goal will be accomplished within the planned time frame.

Major goal 12 (Dr. Tong): the goal is to determine whether inhibition of basal forebrain Glu+ neuron projections to the LH promote motivation to eat. Delivery of AAV-Flex-eNpHR3.0 virus has been made to bilateral basal forebrain regions of Vglut2-Cre and optic fibers have also been implanted targeting the LH. These mice are scheduled to receive training session in a nose poke chamber and then will test wither light delivery will test to measure correct nose pokes and latency to nose poke. It is estimated that the goal will be achieved within the planned time frame.

Major goal 13 (Dr. Arenkiel): Here the goal is to determine whether LH Glu+ neurons are direct downstream targets of basal forebrain Glu+ neurons. Towards this, AAV-Flex-ChR2-GFP virus has been delivered to the basal forebrain and AAV-Flex-GFP virus has been delivered to the LH of *Vglut2-Cre* mice. We have finished the feeding experiments and as shown in Fig. 5,

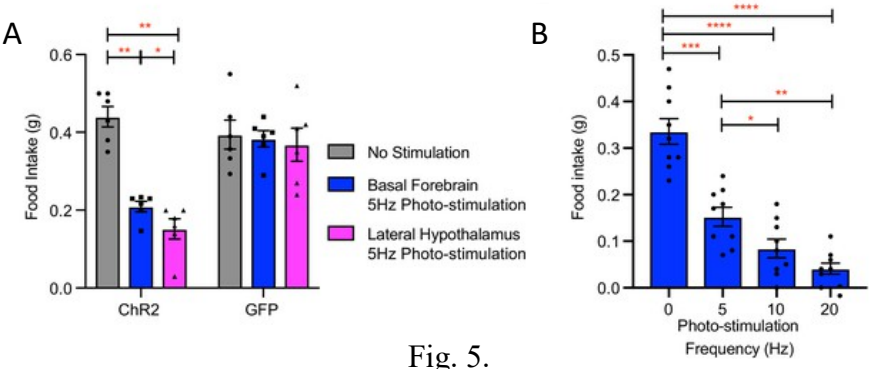


Fig. 5.

local photostimulation in the LH potently inhibited feeding, the extent of which is similar to that observed with direct activation of basal forebrain Glu+ neurons (Fig. 5A). Of note, the effect on feeding inhibition was dependent on laser frequency (Fig. 5B). Ongoing studies are focused on verification of accurate viral delivery and induction of c-Fos in the LH neurons after photostimulation. It is estimated that the milestone in this goal will be met within the planned time window.

Major goal 14 (Dr. Tong): Here the goal is to determine whether LH Glu+ neurons mediate the effect of basal forebrain Glu+ neurons in feeding. *Vglut2-Cre* mice were prepared and AAV-Flex-ChR2 virus has been delivered to the basal forebrain, while at the same time AAV-Flex-hM4Di-mCherry delivered to the LH. Initial experiments on verification of viral delivery have been confirmed. New mice have been prepared, and studies are ongoing to examine effects on feeding. It is projected that the milestone in this goal will be met within the set time window.

Training and professional development

Dr. Zhiying Jiang, a postdoc and Ms. Jing Cai, a graduate student (Site 2, Dr. Tong) are currently involved in this project, and are supported by this funding. Both of them are required to attend our departmental and center seminar series. The departmental seminar series invites well-known scientists across the US to present their new findings and the center seminar series will mainly presented by postdocs and students from each lab to share their research. Thus, both of them will have the opportunities to be exposed to research outside the campus and to present their own ongoing research. In addition, Ms. Cai will have planned activity and training classed within the graduate school, including required committee meetings in which Dr. Arenkiel is a committee member. We also have a regular lab meeting in which all lab members require to present their own research as well present a journal club on the papers from peers. Importantly, both of them have regular weekly meeting with me. Through these various platforms, they will get trainings in research. With the pandemic, almost all seminar series with the UT and TMC use virtual format, in which they regularly attend. Unfortunately, with the impact of the pandemic, it is not easy for us to go to local/national meetings and we are trying to participate virtual meetings organized by various research foundations and other institutions, in order to get better exposure to peers. Of note, Ms. Cai and Dr. Tong have been scheduled to attend this year's SfN meeting in November 2021 at Chicago.

Lab personnel in Arenkiel lab include Ms. Mayuri Patel, Ms. Peyshyuan Chin. Both are current graduate students focused on this project as part of their thesis work. Mayuri and Peyshyuan have received direct training in *in vivo* imaging, electrophysiological, and behavioral analysis, and have also been learning imaging and in vivo electrophysiological recording methods. They are utilizing these skills towards the proposed studies. All are making excellent progress towards the stated project goals, and have maintained timely committee meeting progress reports. Also, as partial contributors, Mr. Benjamin Belfort and Mr. Suyang Bao (two new students to the laboratory) are serving as support and collaborators to the individuals focusing 100% effort towards the project. Although practical research experimentation has been paused during the funding period due to the pandemic, the listed personnel were able to continue analysis of existing data, and reinitiate new experimentation. Additionally, the Arenkiel Lab members have been actively involved with a program called the McNair Teaching Fellows program, where they interface with high school teachers and their classrooms in North Carolina to host lectures and virtual lab tours on their projects. This has been highly beneficial towards them gaining practical teaching experience and to share current scientific findings associated with their work.

Dissemination to community

Nothing to report

Plan for the next reporting period

We will execute the research plan outlined in SOW. There might be a slowdown in research progress because the required mouse colony reduction during the mandatory lockdown period of the pandemic. We will fully attempt to achieve the planned milestones, with some consideration of the delayed research plan.

IMPACT

Impact on development of principle disciplines

Nothing to report

Impact on other disciplines

Nothing to report

Impact on technology transfer

Nothing to report

Impact on society beyond science and technology

Nothing to report

CHANGES/PROBLEMS

It is not anticipated that there is a significant change in the approach or use of animals. However, due to the current pandemic, there might be a change in time to accomplish the planned and stated milestones. Unfortunately, during the initial lockdown, it was mandatory for us to significantly reduce mouse breeding/cages, which has caused a major delay in the availability of mouse study subjects. In addition, we are operating at a reduced personnel effort to achieve effective social distancing, which also delays the progress of research and associated research expenditure. Also due to school/daycare shut down with online course at home, the time spent on experiments on lab members with young kids has also been reduced. Despite facing these adversaries, we have managed to make the planned progress. However, it might be potential that a significant foreseeable change to the project is that we may need additional time to complete all proposed work.

PRODUCTS

During the course this funding period, we have published the following papers which indirectly benefited from this funding.

1. A neural basis for brain leptin action on reducing type 1 diabetic hyperglycemia. Fan S, Xu Y, Lu Y, Jiang Z, Li H, Morrill JC, Cai J, Wu Q, Xu Y, Xue M, Arenkiel BR, Huang C, Tong Q. Nat Commun. 2021 May 11;12(1):2662. doi: 10.1038/s41467-021-22940-4. PMID: 33976218; Acknowledgement of the federal support: Yes.

2. Centrally circulating α-klotho inversely correlates with human obesity and modulates arcuate cell populations in mice. Landry T, Li P, Shookster D, Jiang Z, Li H, Laing BT, Bunner W, Langton T, Tong Q, Huang H. Mol Metab. 2021 Feb;44:101136. doi: 10.1016/j.molmet.2020.101136. Epub 2020 Dec 7. PMID: 33301986; Acknowledgement of the federal support: Yes.

3. Corticotropin Releasing Hormone Signaling in the Bed Nuclei of the Stria Terminalis as a Link to Maladaptive Behaviors. Young CE, Tong Q. Front Neurosci. 2021 Mar 19;15:642379. doi:

10.3389/fnins.2021.642379. eCollection 2021. PMID: 33867924 Acknowledgement of the federal support: Yes.

Nothing to report on products in other categories listed in the report instruction.

PARTICIPANTS & OTHER COLLABORATING ORGANIZATIONS

Name	Benjamin Arenkiel
Project Role:	PI
ORCID ID	0000-0001-9047-2420
Nearest person month worked	12
Contribution to project	Supervision
Funding Support	This Award and NIH grants

Name	Qingchun Tong
Project Role:	PI
ORCID ID	0000-0002-4561-2540
Nearest person month worked	4
Contribution to project	Supervision
Funding Support	This Award and NIH grants

Name	Zhiying Jiang (Site 2)
Project Role:	Postdoctoral researcher
ORCID ID	0000-0002-3838-2791
Nearest person month worked	11
Contribution to project	Viral injections, feeding, body weight and recording
Funding Support	This Award

Name	Jing Cai (Site 2)
Project Role:	Graduate student
ORCID ID	Not available
Nearest person month worked	6
Contribution to project	Viral injections, body weight, feeding
Funding Support	This Award

Name	Mayuri Patel
Project Role:	Graduate student
ORCID ID	Not available
Nearest person month worked	12
Contribution to project	Circuit labeling, viral injections, and behavioral analysis.
Funding Support	This Award

Name	Peyshyuan Chin
Project Role:	Graduate student
ORCID ID	Not available
Nearest person month worked	12
Contribution to project	Circuit labeling, viral injections, and behavioral analysis.
Funding Support	This Award

Name	Benjamin Belfort
Project Role:	Graduate Student

ORCID ID	Not available
Nearest person month worked	3
Contribution to project	Imaging, viral labeling, circuit analysis
Funding Support	This Award

Name	Suyang Bao
Project Role:	Graduate student
ORCID ID	Not available
Nearest person month worked	6
Contribution to project	Circuit labeling, cellular analysis, and behavioral analysis.
Funding Support	This Award

There is no change in PI or key personnel during the reporting period.

Nothing to report on other organization involved as partners.

SPECIAL REPORTING REQUIREMENTS

Nothing to report

APPENDICES:

3 reprints of publications. Additional manuscripts are under review and will be reported in the next report.

LOG NUMBER:PR180451P1 TITLE: Genetically Dissecting Basal Forebrain Circuits Underlying Eating Disorders

PI: Benjamin Arenkiel, Baylor College of Medicine

Budget: $1,144,713.00 **Topic Area:** Eating Disorders **Mechanism:** FY 2018 Peer Reviewed Medical Research Program Investigator-Initiated Research Award

Research Area: 1400 **Award Status:** 01 Sept 2020 – 31 Aug 2021

Study Goals:

The study is designed to test whether basal forebrain glutamatergic projection neurons serve as a primary circuit node to govern eating-related behaviors and the goal is to elucidate the mechanisms by which basal forebrain circuits govern food seeking and/or food aversion.

Specific Aims:

To accomplish the study goal, experiments are designed to 1) (Aim 1) determine how basal forebrain ACh+ and Glu+ neurons are connected in we will decipher how ACh+ neurons communicate with local Glu+ neurons is critical towards understanding the cholinergic basal forebrain circuit mechanisms that underlie eating behavior; 2)
(Aim 2): determine how Glu+ neurons in the basal forebrain influence feeding behavior, in which we will test how food cues influence basal forebrain Glu+ neurons and how perturbations to these cells influence feeding behavior; and 3) (Aim 3): reveal downstream targets of basal forebrain Glu+ neurons that govern feeding behavior, in which we will test the function of LH neurons in mediating basal forebrain-linked feeding output.

Key Accomplishments & Outcomes:

Publications:

1. Ung K, Huang TW, Lozzi B, Woo J, Hanson E, Pekarek B, Tepe B, Sardar D, Cheng YT, Liu G, Deneen B, Arenkiel BR. Olfactory bulb astrocytes mediate sensory circuit processing through Sox9 in the mouse brain. *Nat Commun*. 2021 Sep 1;12(1):5230.
2. Fan S, Xu Y, Lu Y, Jiang Z, Li H, Morrill JC, Cai J, Wu Q, Xu Y, Xue M, Arenkiel BR, Huang C, Tong Q. A neural basis for brain leptin action on reducing type 1 diabetic hyperglycemia. *Nat Commun.* 2021 May 11;12(1):2662. doi: 10.1038/s41467-021-22940-4.PMID: 33976218
3. Pekarek BT, Hunt PJ, Belfort BDW, Liu G, Arenkiel BR. Imaging and Quantification of Intact Neuronal Dendrites via CLARITY Tissue Clearing. *J Vis Exp.* 2021 Apr 20;(170). doi: 10.3791/62532.PMID: 33970138
4. Hanson E, Brandel-Ankrapp K, and Arenkiel BR. Dynamic cholinergic tone in the basal forebrain reflects reward-seeking and reinforcement during olfactory behavior. *Front Cell Neurosci.* 2021 Feb 2, https://doi.org/10.3389/fncel.2021.635837

Patents: Nothing to report

Funding Obtained: Nothing to report

nature COMMUNICATIONS

ARTICLE

https://doi.org/10.1038/s41467-021-25444-3 OPEN

Olfactory bulb astrocytes mediate sensory circuit processing through Sox9 in the mouse brain

Kevin Ung[1,8], Teng-Wei Huang[2,8], Brittney Lozzi[2], Junsung Woo[2], Elizabeth Hanson[3], Brandon Pekarek[3], Burak Tepe[1], Debosmita Sardar[2], Yi-Ting Cheng[1,2], Gary Liu[1,4], Benjamin Deneen[1,2,5,6]✉ & Benjamin R. Arenkiel[1,3,5,7]✉

The role of transcription factors during astrocyte development and their subsequent effects on neuronal development has been well studied. Less is known about astrocytes contributions towards circuits and behavior in the adult brain. Astrocytes play important roles in synaptic development and modulation, however their contributions towards neuronal sensory function and maintenance of neuronal circuit architecture remain unclear. Here, we show that loss of the transcription factor *Sox9* results in both anatomical and functional changes in adult mouse olfactory bulb (OB) astrocytes, affecting sensory processing. Indeed, astrocyte-specific deletion of *Sox9* in the OB results in decreased odor detection thresholds and discrimination and it is associated with aberrant neuronal sensory response maps. At functional level, loss of astrocytic *Sox9* impairs the electrophysiological properties of mitral and tufted neurons. RNA-sequencing analysis reveals widespread changes in the gene expression profiles of OB astrocytes. In particular, we observe reduced GLT-1 expression and consequential alterations in glutamate transport. Our findings reveal that astrocytes are required for physiological sensory processing and we identify astrocytic *Sox9* as an essential transcriptional regulator of mature astrocyte function in the mouse OB.

[1] Program in Developmental Biology, Baylor College of Medicine, Houston, TX, USA. [2] Center for Cell and Gene Therapy, Baylor College of Medicine, Houston, TX, USA. [3] Department of Molecular and Human Genetics, Baylor College of Medicine, Houston, TX, USA. [4] Medical Scientist Training Program, Baylor College of Medicine, Houston, TX, USA. [5] Department of Neuroscience, Baylor College of Medicine, Houston, TX, USA. [6] Department of Neurosurgery, Baylor College of Medicine, Houston, TX, USA. [7] Jan and Dan Duncan Neurological Research Institute at Texas Children's Hospital, Houston, TX, USA. [8] These authors contributed equally: Kevin Ung, Teng-Wei Huang. ✉email: deneen@bcm.edu; arenkiel@bcm.edu

Astrocytes execute an array of roles that are essential for normal brain function[1]. Classically, astrocytes have been considered primarily a support cell, by providing metabolic balance to neurons[2], potassium buffering[3–6], neurovascular coupling[7,8], glutamate recycling[9,10], and regulating extracellular osmotic space[11]. More recently astrocytes have been recognized as active participants in synaptic neurotransmission[12,13]. Synaptic complexes that comprise astrocytic perisynaptic processes, neuronal presynaptic boutons, and postsynaptic dendritic spines form "tripartite" synapses, in which all three elements collectively operate to regulate synaptic signaling[14–17]. Nevertheless, despite their essential contributions to neuronal circuitry, specialized roles for astrocytes in region-specific circuits have only recently been appreciated, and is an emerging feature of astrocyte biology that remains relatively nascent[18–20].

The rodent olfactory system exhibits well-defined anatomy, with astrocytes abundantly localizing at synapse-rich areas of the olfactory bulb (OB) where sensory processing initially occurs. As such, the mouse OB is a good model for investigating astrocyte-neuron interactions. During olfaction, volatile odorant molecules bind to receptors on olfactory sensory neurons (OSNs) that project to distinct glomeruli in the OB[21], each of which are innervated by OSNs that express common olfactory receptors[22–26]. Within glomeruli, OSNs synapse with subsets of sister mitral and tufted cells (M/Ts), where OSN stimulation results in the activation of spatially-defined populations of M/T(s) that can be visualized as discrete odor response sensory maps[27–29]. This representation of external stimuli has typically been studied with attention towards the neuronal constituents of olfactory circuitry[30–32]. Interestingly, OSN activity at OB glomeruli additionally leads to activity of glomerular astrocytes and subsequent functional hyperemia[8]. Despite this known input-output relationship of glomerular astrocytes to OSN activity, the molecular and transcriptional mechanisms that underlie astrocytic contributions to olfactory circuits remain elusive.

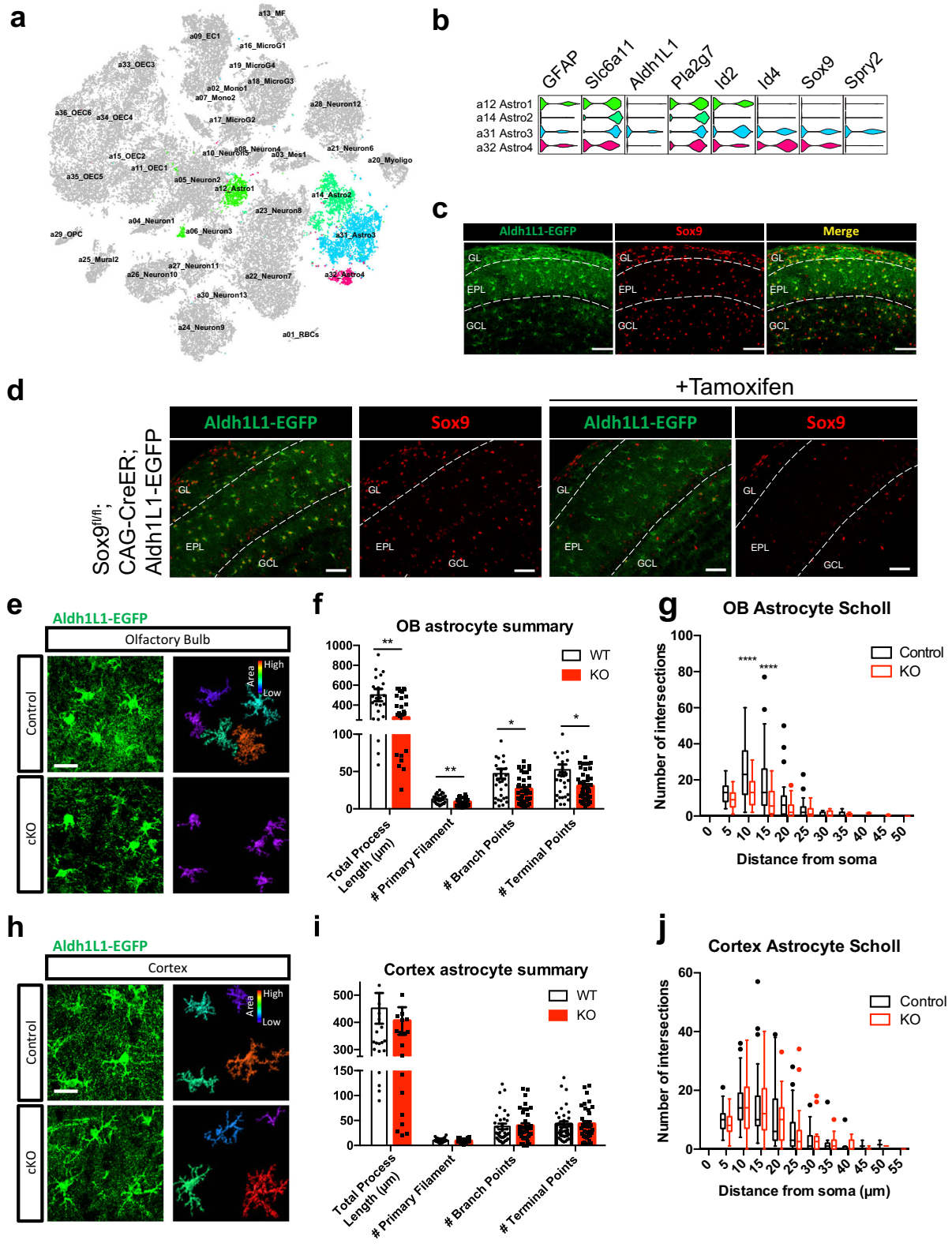
Here we sought to investigate roles for mature astrocytes in the adult mouse olfactory system. Single-cell sequencing revealed that the transcription factor *Sox9* is selectively expressed in astrocyte populations in the OB. While *Sox9* is an established regulator of glial development[33,34], its role in mature astrocytes remains undefined. Therefore we examined the role of *Sox9* in adult OB astrocytes, finding that its deletion drastically altered astrocyte morphology and calcium handling activity. These in vivo manipulations of astrocytes affected olfactory behaviors in mice, influencing both odor detection thresholds and odor discrimination. These observed alterations were accompanied by changes to neuronal sensory response maps, electrophysiological properties of M/T cells, and increased OSN innervation. Finally, the gene expression profiles of *Sox9*-deficient astrocytes were directly affected, highlighted by a reduction in GLT-1 and reduced glutamate transporter currents. Knockdown of GLT-1 in the OB via shRNAi generated phenotypes similar to those observed in *Sox9* KO animals, including altered astrocyte morphology and decreased odor discrimination. Together, these studies illustrate the critical contributions of astrocytes to olfactory information processing, and further define a role for *Sox9* in adult astrocytes of the OB.

Results

Previously, our lab performed single-cell sequencing (Drop-seq) to determine the transcriptional profiles of different populations of cells within the adult mouse olfactory bulb[35]. To screen for prospective regulators of adult astrocyte functions, we performed unbiased clustering based on unsupervised principal-component analysis and visualization using t-distributed stochastic neighbor embedding (t-SNE) and identified 4 distinct astrocyte clusters from a total of 36 populations (Fig. 1a, S1a). We examined the first 500 highly enriched genes that showed robust expression profiles, and subsequently filtered for candidate transcription factors. Setting a threshold for 2-fold increased expression over other cell populations, filtering criteria revealed four TFs: *Id2*, *Id4*, *Sox9*, and *Spry2*. While *Id2* and *Spry2* were expressed in multiple cell type clusters, *Id4* and *Sox9* were only detected in two shared clusters, both within astrocytes and coexpressed with Aldh1L1 (Fig. 1b), a pan-astrocyte marker[36]. Immunohistochemical staining in *Aldh1L1-EGFP* BAC transgenic mice, an established mouse line that labels astrocytes with EGFP[37], showed that expression of *Sox9* in adult animals colocalized exclusively with EGFP in the OB, indicating that its expression is restricted to astrocytes (Fig. 1c). These observations implicate *Sox9* as a key transcriptional regulator of mature astrocyte function, and thus prompted us to focus our studies on roles for *Sox9* in mature astrocytes.

Given the important role of *Sox9* during glial development and astrocyte precursors[34], we sought to determine whether it played a separate and/or additional roles in adult OB astrocytes. Towards this, we generated mice that harbored a conditional floxed *Sox9* allele and a tamoxifen-inducible Cre driven by the CAG promoter (CAG-CreER). Due to the restricted expression of *Sox9* in astrocytes of adult brain tissue[38], this mouse line enabled selective deletion of *Sox9* in adult astrocytes. For conditional mutagenesis, adult mice were treated with tamoxifen twice daily (150 mg/kg each) for a total of 10 days to induce genetic recombination of LoxP sites flanking *Sox9* exons 2-3[39]. Analysis of the OB 6 weeks after tamoxifen treatment confirmed efficient deletion of *Sox9* in OB astrocytes, as well as degradation and loss of existing Sox9 protein (Fig. 1d, S2a). Notably, *Sox9* deletion did not result in a reduction in the overall number of astrocytes (Fig. S2b). Given that astrocyte morphology is linked to their functions related to synaptic modulation, we sought to assess their morphological features after *Sox9* deletion. To visualize astrocyte morphology, we crossed *Sox9* conditional KO mice with Aldh1L1-EGFP BAC transgenic mice, creating a three-allele conditional reporter model (*Sox9* cKO: $Sox9^{fl/fl}$; *CAG-CreER; Aldh1L1-EGFP* and control: $Sox9^{fl/fl}$; *Aldh1L1-EGFP*). Upon tamoxifen-induced KO of *Sox9*, we performed multi-plane confocal imaging for surface rendering and reconstruction of OB astrocyte morphology (Fig. 1e) and observed a reduction in the number of primary filaments (13.121 ± 0.976 in WT vs 9.1 ± 0.724 in KO), branch points (47.000 ± 6.585 in WT vs 26.200 ± 2.911 in KO), terminal points (52.242 ± 7.073 in WT vs 30.275 ± 3.080 in KO), and total process length (500.791 ± 61.890 µm in WT vs 273.148 ± 27.171 µm in KO) (Fig. 1f). Moreover, Sholl analysis revealed a decrease in morphological complexity (Fig. 1g). In contrast, astrocyte morphology in the cortex was largely unaffected (number of primary filaments: 9.879 ± 0.616 in WT vs 8.486 ± 0.668 in KO, branch points: 37.949 ± 5.579 in WT vs 39.057 ± 5.431 in KO, terminal points: 42.385 ± 5.903 in WT vs 42.771 ± 5.589 in KO, and total process length: 451.685 ± 56.622 µm in WT vs 405.389 ± 50.626 µm in KO) (Fig. 1h–j). The differences we detected with *Sox9* KO between astrocyte morphologies in the OB versus the cortex suggest region-specific transcriptional dependencies on *Sox9*. These data indicate that *Sox9* is essential in the homeostatic maintenance of astrocyte morphology in the adult OB.

We sought to further examine *Sox9* function in astrocytes from the OB. Astrocyte calcium activity is considered a key component that mediates their interactions with neurons[40–42]. To evaluate the calcium dynamics in OB astrocytes, we co-injected a viral mixture of an AAV with the astrocyte-specific GFAP promoter driving Cre expression (AAV-GFAP-iCre-P2A-TurboRFP) and a



conditional AAV-GFAP-flex-GCaMP6m into the OB of *Sox9*$^{fl/fl}$ mice to drive genetic deletion of *Sox9* as well as targeted expression of GCaMP6m (Fig. 2a). Similar injections into C57BL/6 J mice (WT) served as controls. Injection in the OB resulted in high efficiency KO of *Sox9* (39.14 ± 5.381% Sox9+; Aldh1L1-EGFP+ astrocytes in *Sox9*$^{fl/fl}$; Aldh1L1-EGFP animals vs 86.51 ± 4.67% in Aldh1L1-EGFP controls) (Fig. S2c–e) as well as comparable changes in morphology seen through tamoxifen-induced KO (Fig. S3a–d). We harvested OB slices 4 weeks after injections and imaged calcium transients via two-photon microscopy (Fig. 2b (left), E) in both controls and *Sox9*$^{fl/fl}$ mice ($n = 3$ and 4 mice of each genotype respectively). To analyze calcium events for all cells within the fields of view, we used the previously reported GECIquant software[43] to generate semi-automated

Fig. 1 RNA-seq identified Sox9 as an important transcription factor in mature, adult astrocytes. a Cellular composition of the OB was visualized using t-distributed stochastic neighbor embedding (t-SNE). Single-cell sequencing allowed unbiased clustering of cell populations in the OB, revealing 36 distinct populations. Astrocyte clusters are highlighted for identification. **b** Of the 36 populations, 4 astrocyte populations were found based on expression of known astrocyte markers (Aldh1L1 and GFAP). Violin plots show common astrocyte markers along with 4 transcription factors found to be highly expressed across astrocyte populations. **c** Representative images from coronal sections from the Aldh1L1-EGFP BAC transgenic mouse line showed that immunohistochemical staining of *Sox9* colocalizes with astrocytes in the OB. $N = 3$ mice. Scale bar, 50 μm. **d** Representative images from coronal sections from the OB showing *Sox9* expression in control animals (left) and tamoxifen-induced KO of *Sox9* (right). $N = 3$ mice. Scale bar, 50 μm. **e–g** High-resolution imaging and surface rendering of astrocytes in OB shows a decrease in morphological branching in *Sox9* KO vs controls. $n = 33$ cells (control) and $n = 40$ cells (*Sox9* KO) from $N = 3$ mice, respectively. Adjusted $p = 0.0021$, 0.0046, 0.0219, and 0.0230 for total process length, # primary filament, # branch points, and # terminal points, respectively; 2-way ANOVA with Sidak's multiple comparison correction. Data are presented as box plots displaying interquartile range and medians displaying interquartile range and median with Tukey whiskers. Scale bar, 20 μm. **h–j** High-resolution imaging and surface rendering of astrocytes in cortex shows no significant change in morphological branching in *Sox9* KO vs controls. $n = 39$ cells (control) and $n = 35$ cells (*Sox9* KO) from $N = 3$ mice, respectively. 2-way ANOVA with Sidak's multiple comparison correction. Control in E-J is $Sox9^{fl/fl}$; Aldh1L1-EGFP. Data are presented as box plots displaying interquartile range and median with Tukey whiskers. Scale bar, 20 μm.

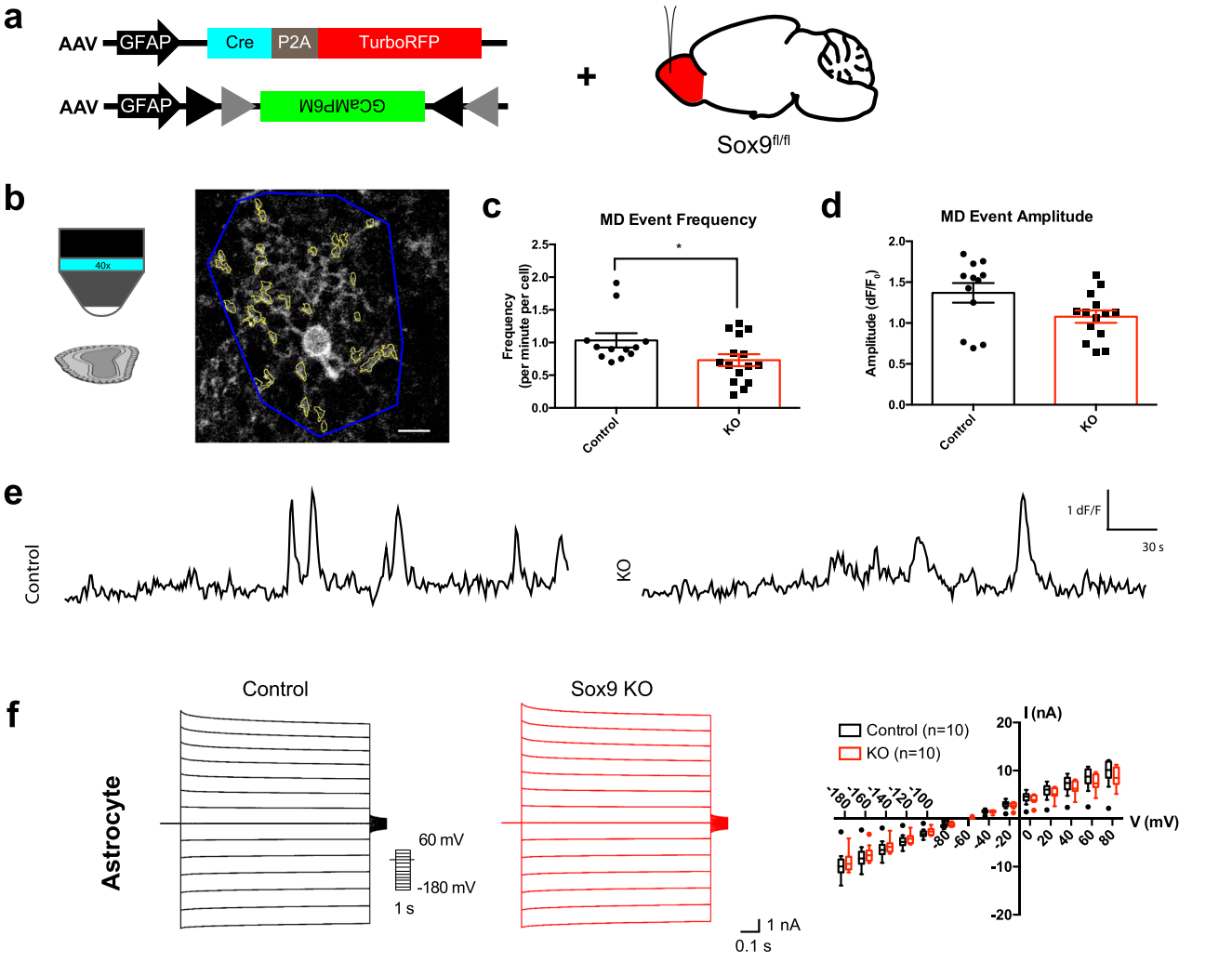


Fig. 2 Sox9 deletion disrupted cell intrinsic properties in astrocytes. a Schematic of virally-induced *Sox9* KO approach and targeted expression of GCaMP in astrocytes with *Sox9* deleted. **b** Schematic of two-photon imaging of GCaMP6m from an ex vivo slice from $Sox9^{fl/fl}$ animals injected with a GFAP-driven Cre virus. Images were captured at ~1 Hz over 5 min. Approximate astrocyte territory (outlined in blue) defined the range for a single astrocyte and contained multiple astrocyte microdomains (outlined in yellow). Scale bar, 10 μm. **c**, **d** Quantification of calcium events in microdomains (MDs) of astrocyte processes. Astrocytes with *Sox9* KO have a lower frequency of calcium events in microdomains but no change in amplitude. $^*p = 0.0435$ Unpaired two-sided t-test. $n = 12$ cells from $N = 3$ control mice and $n = 15$ cells from $N = 4$ *Sox9* KO mice. Data are presented as mean values ± SEM. **e** Example traces of GCaMP6m signal in microdomains of astrocytes in control and *Sox9* KO astrocytes. **f** Whole-cell patch clamp electrophysiology of astrocytes show no changes in the I-V curve of astrocytes with stepped current injections in *Sox9* KO vs controls. $n = 10$ cells (control) and $n = 10$ cells (*Sox9* KO) from $N = 3$ mice, respectively. Data are presented as box plots displaying interquartile range and median with Tukey whiskers. Controls are C57BL/6 J injected with AAV-GFAP-iCre-P2a-TurboRFP + AAV-GFAP-flex-GCaMP6m.

detection of regions of interest (ROIs) (Fig. 2b, right). While astrocyte somas showed no changes in calcium events, we found that *Sox9*-deleted astrocytes displayed a significant decrease in frequency of calcium events normalized specifically across the regions of microdomains (1.056 ± 0.128 events per minute in KO vs 0.730 ± 0.092 events per minute in control), and no significant change in event amplitude (Fig. 2c–e). The reduction in astrocyte microdomain calcium events are congruent with the observed changes in astrocyte morphology. Together, the defects in gross morphology and changes in astrocyte microdomain calcium activity validated functional aberrations in the cellular properties of *Sox9* KO astrocytes.

To measure whether *Sox9* KO affected biophysical properties in astrocytes, we next performed electrophysiological whole-cell patch clamp recordings. For this we injected $Sox9^{fl/fl}$ animals or C57BL/6 J controls with AAV-GFAP-iCre-P2a-TurboRFP and, allowing 4 weeks for viral expression, recombination, and degradation of *Sox9* protein. Stepped current injections revealed no differences in the current-voltage relationship between *Sox9* KO and control cells, displaying characteristic linear IV curve with similar slopes (Fig. 2f), suggesting that deletion of *Sox9* in astrocytes did not affect their general membrane properties.

Calcium activity in astrocytes is considered an indirect measure of astrocyte-neuron interactions, that can ultimately influence neuronal activity[44,45]. Therefore, the observed defects in calcium activity in astrocytes lacking Sox9 raised the question of whether astrocyte-neuron signaling is altered by deletion of *Sox9* in OB astrocytes. To address this, we first assayed animals for potential alterations in olfactory related behaviors by injecting AAV-GFAP-iCre-P2a-TurboRFP into $Sox9^{fl/fl}$ mice to selectively knock-out *Sox9* in OB astrocytes, or into C57BL/6 J mice as controls. Four weeks after injection, allowing ample time for viral expression, recombination, and degradation of Sox9 protein, we performed odor detection and olfactory habituation/dishabituation assays using a 3-compartment place preference assay (3PP). Mice were habituated to a 3-compartment chamber where the outer compartments contained mineral oil and the middle compartment served as a neutral barrier. After habituation, we swapped mineral oil with a novel odorant ((R)-Limonene) in one compartment in a four-step ascending concentration series and measured the time that mice spent in that compartment investigating the odor versus mineral oil. Control mice investigated both mineral oil and (R)-Limonene compartments equally until odor concentrations of 10^{-3} (v/v) of (R)-Limonene, in which control mice then spent more time in the compartment with the odor (Zone preference index = 0.198 ± 0.096)(Fig. 3a, b), suggesting novel odor detection. Somewhat surprisingly, *Sox9* KO mice spent more time investigating odorants at concentrations at dilutions to 10^{-5} (v/v) (Zone preference index = 0.279 ± 0.122). Similar detection results were obtained when (+)-Carvone was tested (Fig. S4a) with *Sox9* KO mice trending towards increased odor sensitivity compared to controls. With isoamyl acetate, a non-preferred odor, mice spent more time investigating the compartment with mineral oil upon odor detection but showed no significant changes in odor sensitivity at the concentrations tested in *Sox9* KO mice as compared to controls (Fig. S4b). Together, these data suggest that mice with *Sox9* deleted from olfactory bulb astrocytes exhibit decreased olfactory detection thresholds and thus increased odor sensitivity.

Next, to assay for detection of differences in olfactory discrimination[46], we used a related paradigm to examine fine odor discrimination by introducing the novel, but structurally similar odorant (S)-Limonene. Upon habituating mice to (R)-Limonene (10^{-3}), we then introduced (S)-Limonene (10^{-3}). In the presence of (S)-Limonene, control mice spent significantly more time in the compartment investigating the novel odor (Zone preference index = −0.104 ± 0.102 for (R)-Limonene vs 0.199 ± 0.131 for (S)-Limonene), whereas *Sox9* KO mice showed no significant differences in compartment preference (Zone preference index = 0.045 ± 0.130 for (R)-Limonene vs 0.138 ± 0.157 for (S)-Limonene) (Fig. 3c). Together, these data suggest that *Sox9* KO mice have more sensitive odor detection thresholds, but are deficient in their ability to discriminate between chemically similar but perceivably different odors. These observations indicate that Sox9 plays a critical role in astrocyte regulation of circuit-level sensory processing and the behavioral outcomes associated with olfactory circuit function.

The observed aberrant olfactory behavioral phenotypes next led us to investigate whether olfactory bulb neurons and their circuits are impacted non-cell-autonomously by *Sox9* KO in OB astrocytes. We first examined whether *Sox9* deletion in OB astrocytes altered olfactory sensory response maps. Towards this, we generated $Sox9^{fl/fl}$; Thy1-GCaMP3 mice, that expressed the genetically-encoded calcium indicator GCaMP3 in M/T cells, and used the viral-based approaches described above to selectively knock-out (KO) *Sox9* in OB astrocytes while monitoring odor-evoked calcium responses in M/T cells. After injecting AAV-GFAP-iCre-P2a-TurboRFP into $Sox9^{fl/fl}$; Thy1-GCaMP3 mice to selectively KO *Sox9* in OB astrocytes or Thy1-GCaMP3 mice[47] as controls, we imaged the dorsal surface of the olfactory bulb for potential changes in sensory response map properties to a panel of different odorants (Fig. 3d). Notably, we found aberrant changes to the area of activation of the imaged neuronal odor sensory maps in the *Sox9*-KO OB compared to controls (Fig. 3e, f). By implementing automated maximum entropy thresholding approaches, we observed that the area activated by odorants significantly increased (Fig. 3e), along with a decrease in the number of centroids (Fig. 3f) in experimental animals compared to controls, suggesting altered activated domains and OB sensory maps. Given the changes in sensory response maps of M/T cells in *Sox9* KO mice, we sought to determine if glomerular olfactory maps were altered by loss of *Sox9*. To observe glomerular olfactory maps, we examined OSN inputs by staining for olfactory marker protein (OMP), a key marker of mature OSNs important in regulating formation and refinement of glomeruli[48]. In coronal sections of the OB, we observed an increase in the OMP density per glomerulus (37,821 ± 3,155 μm^3/glomerulus in control mice vs 59,621 ± 4,384 μm^3/glomerulus in *Sox9* KO mice), as well as increased glomerular size (37,821 ± 3,155 μm^3 in control mice vs 59,621 ± 4,384 μm^3 in *Sox9* KO mice) in *Sox9* KO mice (Fig. S4c–h), suggesting increased OSN innervation into glomeruli after *Sox9* deletion in OB astrocytes. Together, these data implicate Sox9 as an important molecular player in astrocytes in regulating neuronal sensory maps in the OB and support the notion that neuron-astrocyte coordination is disrupted in the absence of Sox9.

The previous data illustrate both altered astrocyte function and astrocyte-neuron communication, which led us to evaluate whether electrophysiological properties of neurons were also affected when *Sox9* was deleted from astrocytes. Towards this, we injected AAV-GFAP-iCre-P2a-TurboRFP into the OB of $Sox9^{fl/fl}$ mice to selectively knock out *Sox9* in OB astrocytes, or into C57BL/6 J mice as controls. We performed whole-cell recordings from M/T cells since these cells directly receive odor information from olfactory sensory neurons and serve as the primary neuronal output from the OB to higher order brain regions involved in odor processing. To determine if other active response properties were affected, we applied stepped current injections at 20 pA increments. In animals with *Sox9* deletion, M/T cells showed a significant decrease in the number of evoked action potentials during both short (50 ms, Fig. 4a, b) and long (500 ms, Fig. 4c, d) pulses compared to controls. These data reveal that M/T cell function is altered in the presence of *Sox9*-KO astrocytes, indicating that the alterations in astrocyte

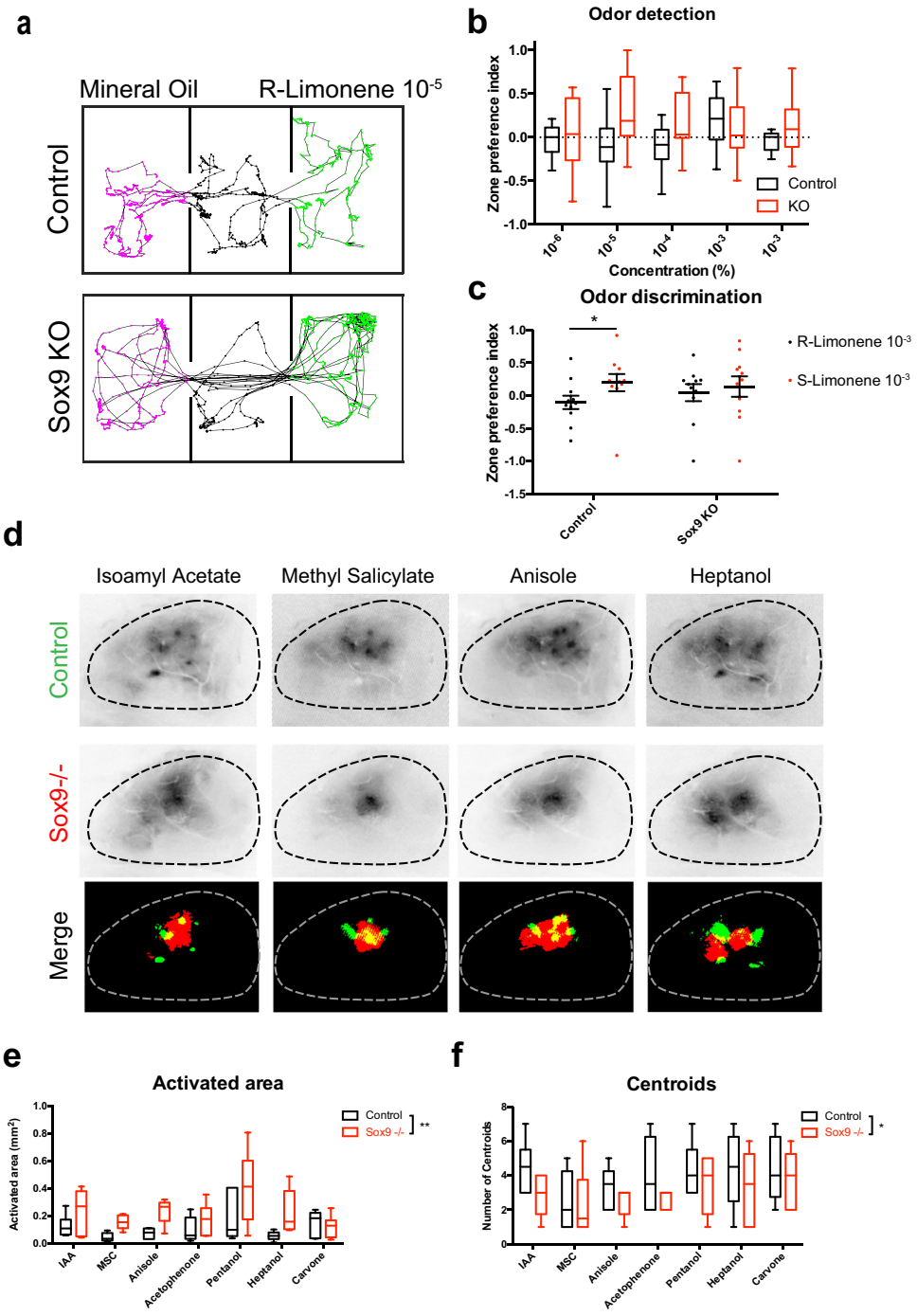


Fig. 3 Deletion of the astrocyte specific marker Sox9 dysregulated olfactory behaviors and sensory maps. a Schematics of live mouse tracking during three compartment place preference assay. Top represents a control mouse investigating the both chambers equally with the odor present at 10^{-5}. Bottom represents a *Sox9* KO mouse preferentially investigating the odor chamber at 10^{-5}. **b** Quantification of (**a**). $n = 11$ (*Sox9* KO) and $n = 11$ (Control). Two-way RM ANOVA with Bonferroni's multiple comparison test (main effect of group, $F(1,20) = 1.913$, $p = 0.1819$; group X concentration interaction, $F(3,60) = 3.385$, $p = 0.0238$). Data are presented as box plots displaying interquartile range and median with Tukey whiskers. **c** Whisker plot quantifying three chamber place preference during odor discrimination. $n = 11$ (*Sox9* KO) and $n = 11$ (Control). Two-way RM ANOVA with Bonferroni's multiple comparison test (main effect of odor, $F(1,20) = 5.895$, $p = 0.0247$; group X odor interaction, $F(1,20) = 1.660$, $p = 0.2123$). Data are shown as mean ± s.e.m. **d** Representative images of neuronal olfactory sensory maps from 4 different odorants of control animals vs astrocyte *Sox9* KO animals. Merged image shows changes in olfactory sensory maps after binary thresholding. **e**, **f** Quantification of change in activated area (main effect of group, $F(1,67) = 9.056$, $p = 0.0037$) and number of centroids (main effect of group, $F(1,70) = 6.235$, $p = 0.0149$) in *Sox9* KO animals vs controls. $n = 6$ mice per group. Two-way ANOVA with Sidak's multiple comparison correction. Data are presented as box plots displaying interquartile range and median with Tukey whiskers. Control in A-C is C57BL/6 J injected with AAV-GFAP-iCre-P2a-TurboRFP; control in **d**–**f** is Thy1-GCaMP3 injected with AAV-GFAP-iCre-P2a-TurboRFP.

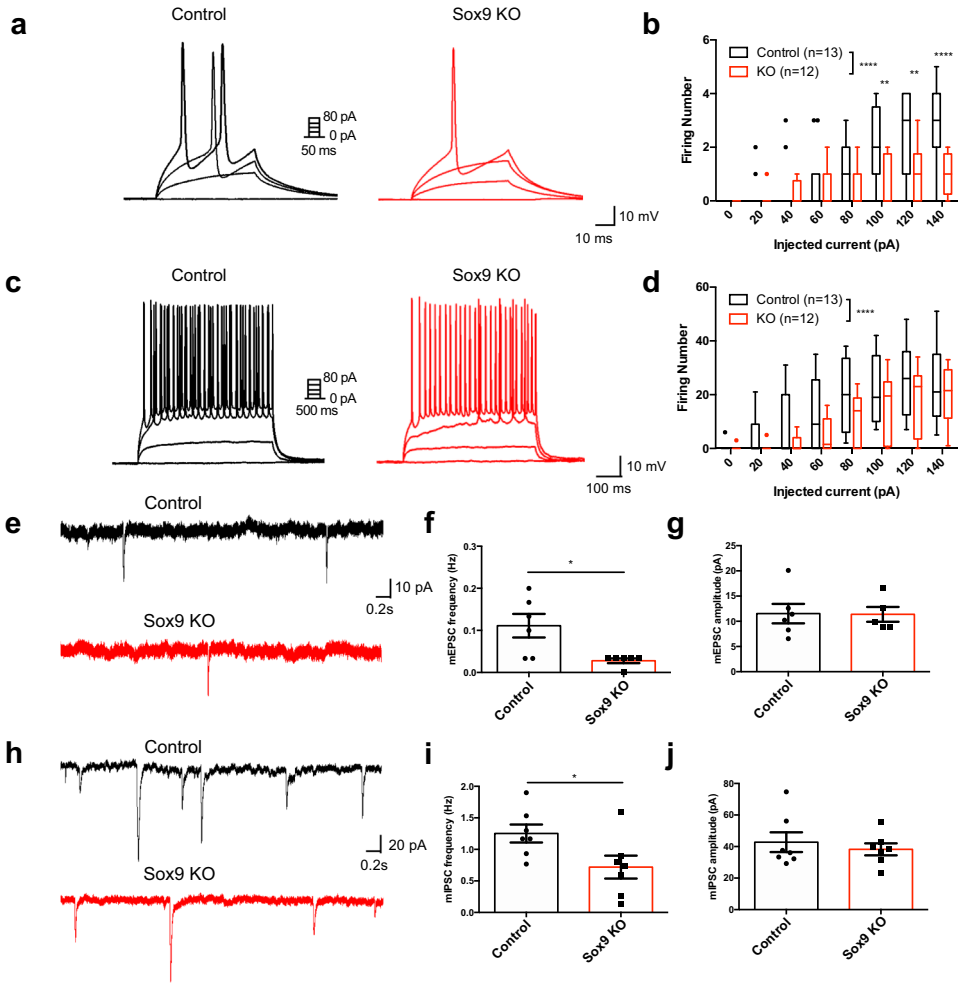


Fig. 4 Electrophysiological recordings showed a reduction in evoked APs in M/T as well as altered synaptic properties. (**a**–**d**) Whole-cell patch clamp electrophysiology of M/T cells revealed a reduction in firing number from stepped current injections with *Sox9* KO in astrocytes vs control astrocytes. $n = 13$ cells (control) and $n = 12$ cells (*Sox9* KO) from $N = 3$ mice, respectively. $^{**}p = 0.0023$ and 0.0014 for 100 and 120 pA current injections, respectively; $^{****}p < 0.0001$; Two-way ANOVA with Sidak's multiple comparison correction. Data are presented as box plots displaying interquartile range and median with Tukey whiskers. **e** Example traces of mEPSC recordings in M/T cells with control astrocytes (top) and *Sox9* KO astrocytes (bottom). **f** M/T cells with *Sox9* KO astrocytes show a significant decrease in mEPSC frequency compared to control astrocytes. $n = 8$ cells (control) and $n = 7$ cells (*Sox9* KO) from $N = 3$ mice, respectively. $^{*}p = 0.0156$. Two-tailed Student's t-test. Data are presented as mean values ± SEM. **g** M/T cells show no changes in mEPSC amplitude with *Sox9* KO in astrocytes. $n = 8$ cells (control) and $n = 7$ cells (*Sox9* KO) from $N = 3$ mice, respectively. Two-tailed Student's t-test. **h** Example traces of mIPSC recordings in M/T cells with control astrocytes (top) and *Sox9* KO astrocytes (bottom). Data are presented as mean values ± SEM. **i** M/T cells with *Sox9* KO astrocytes show a significant decrease in mIPSC frequency compared to control astrocytes. $n = 7$ cells (control) and $n = 7$ cells (*Sox9* KO) from $N = 3$ mice, respectively. $^{*}p = 0.0392$. Two-tailed Student's t-test. Data are presented as mean values ± SEM. **j** M/T cells show no changes in mIPSC amplitude with *Sox9* KO in astrocytes. $n = 7$ cells (control) and $n = 7$ cells (*Sox9* KO) from $N = 3$ mice, respectively. Two-tailed Student's t-test. Control is C57BL/6 J injected with AAV-GFAP-iCre-P2a-TurboRFP. Data are presented as mean values ± SEM.

properties driven by *Sox9* have direct effects on neuronal substrates within the OB. Given that M/T cell physiological properties were affected, and that astrocytes contribute to synaptic function, we next examined if synaptic properties were affected. Notably, while performing targeted whole cell recordings in M/T cells we found that mEPSC and mIPSC frequencies were reduced (mEPSC: 0.1111 ± 0.0281 Hz in controls vs 0.0277 ± 0.0055 Hz in *Sox9* KO; mIPSC: 1.252 ± 0.1425 Hz in controls vs 0.7190 ± 0.1811 Hz in *Sox9* KO) with no observable changes in amplitudes (Fig. 4e–j), indicating fewer synaptic connections following *Sox9* KO.

Detecting altered synaptic properties in M/T cells associated with Sox9-deficient astrocytes, we next queried the specificity of this effect by examining whether other neuronal subtypes in the OB were affected. Granule cells are the most prevalent interneuron cell-type in the OB, and are known to make dendrodendritic connections with M/T cells[49,50]. We observed no significant changes in the electrophysiological properties of granule cells (Fig. S5a, b), indicating that *Sox9* deletion affected neuron-astrocyte interactions in a cell-type specific manner within the OB, with pronounced effects manifesting in M/T cells.

The observed changes in astrocyte morphology and calcium activity (Figs. 1 and 2), coupled with Sox9's role as a potent transcription factor, suggest that Sox9-deficient astrocytes exhibit widespread changes in gene expression. To assay for such changes in gene expression, and assess the impact on astrocyte-neuron interactions, we next performed whole-transcriptome RNA-seq expression analysis on fluorescence-activated cell sorting (FACS)-isolated *Sox9* KO astrocytes from the OB[51]. AAV-GFAP-iCre-P2a-TurboRFP was injected into $Sox9^{fl/fl}$ mice or C57BL/6 J control mice. After 4 weeks to allow for deletion of *Sox9* DNA and degradation of *Sox9* mRNA and protein, astrocytes were FACS-isolated using TurboRFP as a marker for astrocytes. RNA-seq

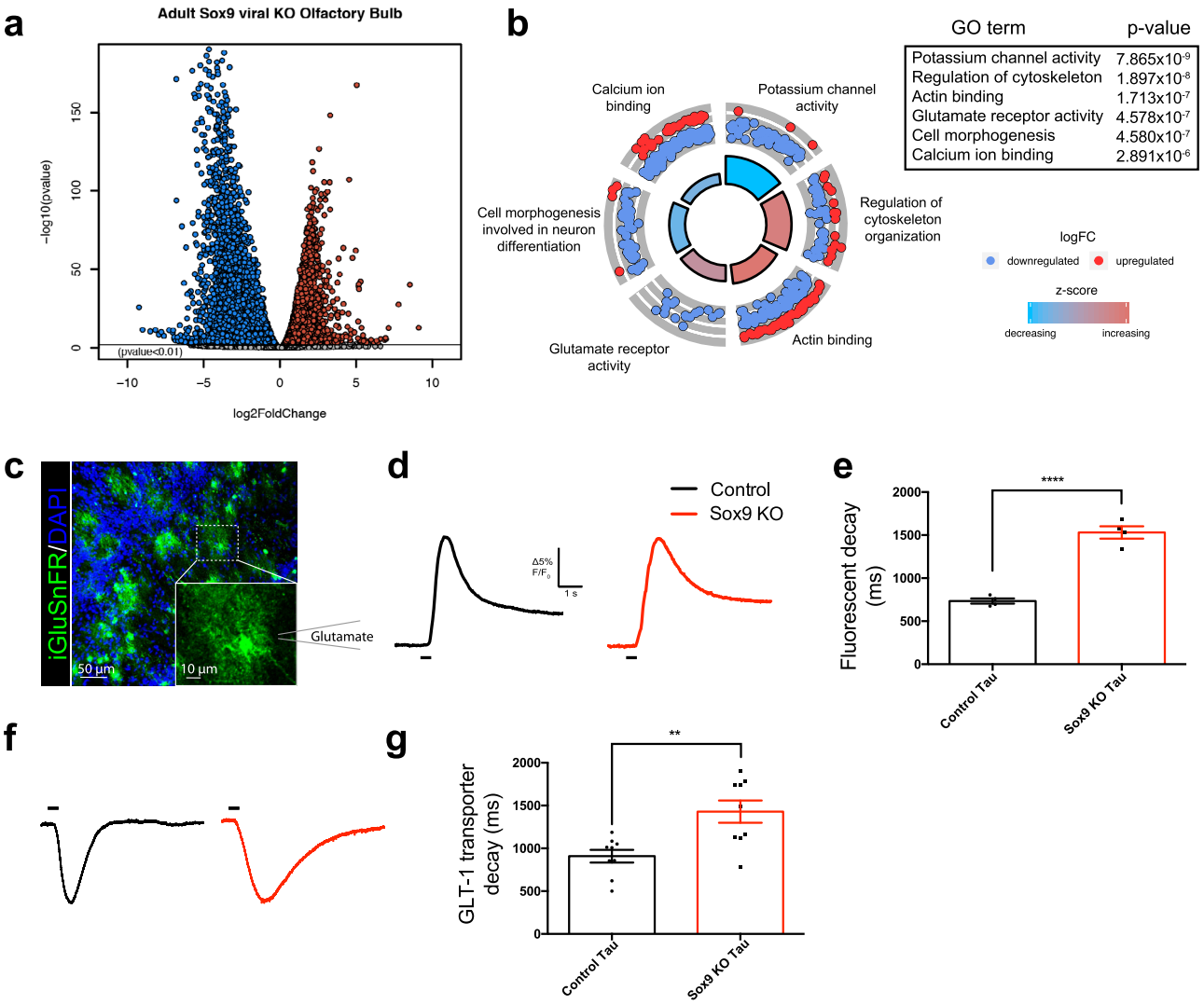


Fig. 5 RNAseq revealed a significant change in transcription profile of adult, Sox9-deleted astrocytes. a Volcano plot of genes significantly upregulated (red dots) and downregulated (blue dots) in *Sox9*-deleted astrocytes compared to controls. **b** Downregulated genes from *Sox9* deletion revealed GO terms associated with neurotransmitter receptor and ion channel activity, as well as cellular morphology. **c** Representative high resolution image of iGluSnFR expressed in astrocytes in the OB. $N = 4$ mice. Inset: high magnification of a single astrocyte with schematic of glutamate puffer nearby astrocyte. **d** Example trace of iGluSnFR signal from control and *Sox9* KO astrocytes after puffing glutamate [534 mM]. Black line indicates duration of glutamate puff. **e** Quantification of (**d**). *Sox9* KO astrocytes had a significantly increased decay after puffing glutamate. $n = 37$ cells (control) and $n = 35$ cells (*Sox9* KO) from $N = 4$ mice, respectively. $^{****}p < 0.0001$. Two-tailed Student's t-test. Data are presented as mean values ± SEM. **f** Example peak normalized traces from whole cell electrophysiological recordings of glutamate transporter currents in astrocytes. Black line indicates duration of glutamate puff. **g** Quantification of (**f**). *Sox9* KO astrocytes had a significantly increased decay after puffing glutamate. $n = 9$ cells (control) and $n = 9$ cells (*Sox9* KO) cells from $N = 4$ and 3 mice, respectively. $^{**}p = 0.0032$. Two-tailed Student's t-test. Controls in A-B and F-G are C57BL/6 J injected with AAV-GFAP-iCre-P2a-TurboRFP; controls in C-E are C57BL/6 J injected with AAV-GFAP-iGluSnFR. Data are presented as mean values ± SEM.

expression analysis revealed pronounced dysregulation of gene expression; using $p < 0.05$ and a threshold of 1.5-fold change in expression, our analysis identified over 2,500 differentially expressed genes (407 upregulated in KO and 2,057 downregulated in KO) (Fig. 5a). From the list of significantly upregulated or downregulated genes, further analysis of the expression profile of *Sox9* deleted astrocytes with gene ontology (GO) revealed a significant reduction in expression in genes related to channel activity, ion balance, calcium signaling, and importantly, the response to neuronal circuit activity (Fig. 5b; Fig. S6c). This analysis revealed that *Sox9*-deleted astrocytes significantly downregulated genes associated with physiological processes essential for neuronal function, astrocyte cellular structure, and astrocyte morphology. Importantly, the observed changes in gene expression were congruent with phenotypic analysis of *Sox9*-deficient astrocytes, as they exhibited notable changes in cellular morphology (Fig. 1e–g) and suppression of calcium activity (Fig. 2b–d). Alterations in astrocyte form and function subsequently exert themselves onto neurons manifesting in the OB as M/T cell activity disruption, further suggesting that *Sox9* KO may exhibit defects in neuron-astrocyte coordination and/or communication in the OB. qPCR verification of select target genes encoding astrocyte receptors and channels responsible for neuronal synaptic responses and homeostatic scaling mechanisms confirmed the changes in gene expression revealed by RNA-seq (Fig. S6d).

Further analysis of the RNA-seq data revealed downregulation of genes such as Syt11, which is a known factor that regulates membrane trafficking and exocytosis[52–54], and Slc1a2 (GLT-1),

the predominant glutamate transporter in astrocytes that participates in reuptake of glutamate from the synaptic cleft. Given these transcriptional changes, the observed changes in sensory responses, and altered M/T cell synaptic function, we next queried if these phenotypes may be linked to altered astrocytic glutamate handling. Towards this, we employed the glutamate-sensing reporter iGluSnFR[55] to assay for potential changes in *Sox9* KO astrocyte glutamate uptake from the reduction of GLT-1 RNA. We injected AAV-GFAP-iCre-P2a-TurboRFP with AAV-GFAP-iGluSnFR into $Sox9^{fl/fl}$ animals to selectively express iGluSnFR in *Sox9* KO astrocytes, or AAV-GFAP-iGluSnFR alone into C57BL/6 J animals as controls. With iGluSnFR expressed in *Sox9* KO astrocytes or controls, respectively, we performed widefield ex vivo imaging with puff administration of glutamate (500 mM in ACSF) to observe responses to extracellular glutamate (Fig. 5c). Each puff of glutamate evoked robust and short-lived iGluSnFR fluorescent signals (Fig. 5d). We assessed the rate of glutamate uptake by measuring the rate of decay of iGluSnFR signal, and observed that the signal decay was far slower in *Sox9* KO astrocytes compared to that observed in control astrocytes (Fig. 5e), suggesting altered and slower glutamate uptake with loss of Sox9.

To independently confirm the results of the iGluSnFR optical sensor, we next performed targeted electrophysiological studies. Using whole-cell patch clamp recordings from control and *Sox9* KO astrocytes, we applied local puffs of glutamate (500 mM in ACSF) adjacent to recorded astrocytes. We recorded baseline glutamate mediated currents, followed by currents after application of TBOA to block glutamate transporters (Fig. 5f), and observed that indeed the decay constant of the subtracted glutamate transport was significantly longer in *Sox9* KO astrocytes compared to controls (1429 ± 130.0 ms vs 908.4 ± 74.81 ms, respectively) (Fig. 5g).

Given that loss of *Sox9* results changes in glutamate uptake, we sought to address the contributions of GLT-1 dysregulation on the previously identified phenotypes. To determine the impact of downregulation of GLT-1 on these other phenotypes, we used viral delivered GLT-1 shRNA to selectively knockdown GLT-1 transcription[56]. After viral injection and recovery, viral delivered shGLT1 with EFi1-driven TurboRFP marker resulted in a significant reduction in GLT-1 mRNA normalized to GAPDH, and compared to shScramble-injected controls (Fig. S6e). We next injected AAV-shGLT-1 or AAV-shScramble controls into the OB of Aldh1L1-EGFP animals. After allowing 5 weeks for efficient knockdown of GLT-1 mRNA, we assayed for changes in astrocyte morphology by performing multi-plane confocal imaging and reconstruction. Similarly to *Sox9* KO astrocytes, we observed a significant reduction in the number of branch points (46.397 ± 3.161in shScramble injected animals vs 22.543 1.052 in shGLT1 injected animals), terminal points (50.463 ± 3.276 in shScramble vs 26.421 ± 1.14 in shGLT1), and total process length (419.517 ± 24.782 µm in shScramble vs 197.307 ± 8.069 µm in shGLT1) (Fig. 6a, b). Sholl analysis also revealed a significant reduction in morphological complexity (Fig. 6c).

To determine the effects of GLT-1 knockdown in the OB, we next examined for potential changes in synaptic properties. We found decrease mEPSC frequencies, but mIPSC frequencies were increased (mEPSC: 0.6905 ± 0.2117 Hz in controls vs 0.0750 ± 0.0225 Hz in shGLT1; mIPSC: 0.8100 ± 0.1568 Hz in controls vs 1.742 ± 1.068 Hz in shGLT1). With no observable changes in amplitudes (Fig. 6d–i), knock down of GLT-1 exerted differing effects on inhibitory and excitatory synapses in the OB.

With the changes in astrocyte morphology and synaptic connections in the OB following GLT-1 KD, we next sought to determine the effects of olfactory sensitivity and discrimination using the 3 compartment place preference assay as described above. In control mice injected with shScramble in the OB, mineral oil and (R)-Limonene compartments were investigated equally until odor concentrations of 10^{-4} (v/v) of (R)-Limonene, in which control mice then spent more time in the compartment with the odor (Zone preference index = 0.364 ± 0.130), suggesting novel odor detection. Mice injected with shGLT1 spent more time investigating odorants at concentrations at dilutions to 10^{-3} (v/v) (Zone preference index = 0.294 ± 0.133) (Fig. 6j). However, two-way repeated measures ANOVA revealed no significant differences by factor of group, odor, or interaction.

To assay for odor discrimination, we habituated mice to (R)-Limonene before introducing (S)-Limonene. In the presence of (S)-Limonene, control mice spent more time in the compartment investigating the novel odor (Zone preference index = 0.2119 ± 0.1887 for (R)-Limonene vs 0.4129 ± 0.09874 for (S)-Limonene), whereas GLT-1 KD mice showed no significant differences in compartment preference (Zone preference index = 0.1801 ± 0.1419 for (R)-Limonene vs −0.05538 ± 0.09721 for (S)-Limonene) (Fig. 6k). Two-way repeated measures ANOVA revealed a significant interaction between both group and odor. Together, these data suggest that GLT-1 KD mice have no change to odor detection thresholds compared to scrambled controls, but have altered ability to discriminate between chemically similar but perceivably different odors. Collectively, these findings reveal that astrocytes play an important role in sensory processing through neuron-astrocyte interactions. The specific phenotypes of altered neuronal properties and abnormal odor discrimination that are similar to *Sox9* KO mice suggests that altered glutamate handling contributes to the observed phenotypic abnormalities in *Sox9* KO mice.

Discussion

Here we performed astrocyte-specific KO of *Sox9* in the mouse olfactory bulb, and identify roles for astrocytes in direct modulation of sensory circuits. Combining genetic and viral manipulations, electrophysiological recordings, and in vivo imaging methods, we found that Sox9 plays an important role in maintaining proper function and transcriptional maintenance of mature, adult astrocytes. Notably, we found that astrocytic modulation of neurons not only affected their activity, but also behavioral output associated with both odor detection and odor discrimination tasks. Together these data reveal a role for Sox9 in governing mature astrocyte function, and more broadly, supports diverse roles for astrocyte-neuron coordination in sensory processing system.

Sox9 associates with the gliogenic switch that causes neural progenitors to transit from neurogenesis to gliogenesis[33,34]. Despite well-known functions for *Sox9* in embryonic glial development and the perdurance of Sox9 expression in the adult brain[38], roles for *Sox9* in mature adult astrocytes remain broadly unstudied. The approaches utilized here to selectively investigate astrocytes (tamoxifen-inducible and viral) enabled us to bypass Sox9's role in development and interrogate its function in the adult brain, where we found that Sox9 exerts key roles in maintaining astrocyte morphology and communication with OB neurons. In addition, GO analysis of transcriptome data revealed downregulation of many genes related to maintaining cellular morphology and governing physiological responses, both of which are key roles in the supportive functions of astrocytes. These observations, coupled with phenotypic analysis of Sox9-deficient astrocytes, illustrate that Sox9 regulates the expression of many genes that are essential for the homeostatic function of adult astrocytes, and that these functions are critical to normal neuronal output and sensory processing. Noticably, we observed varying effects on astrocyte morphology from deletion of *Sox9*

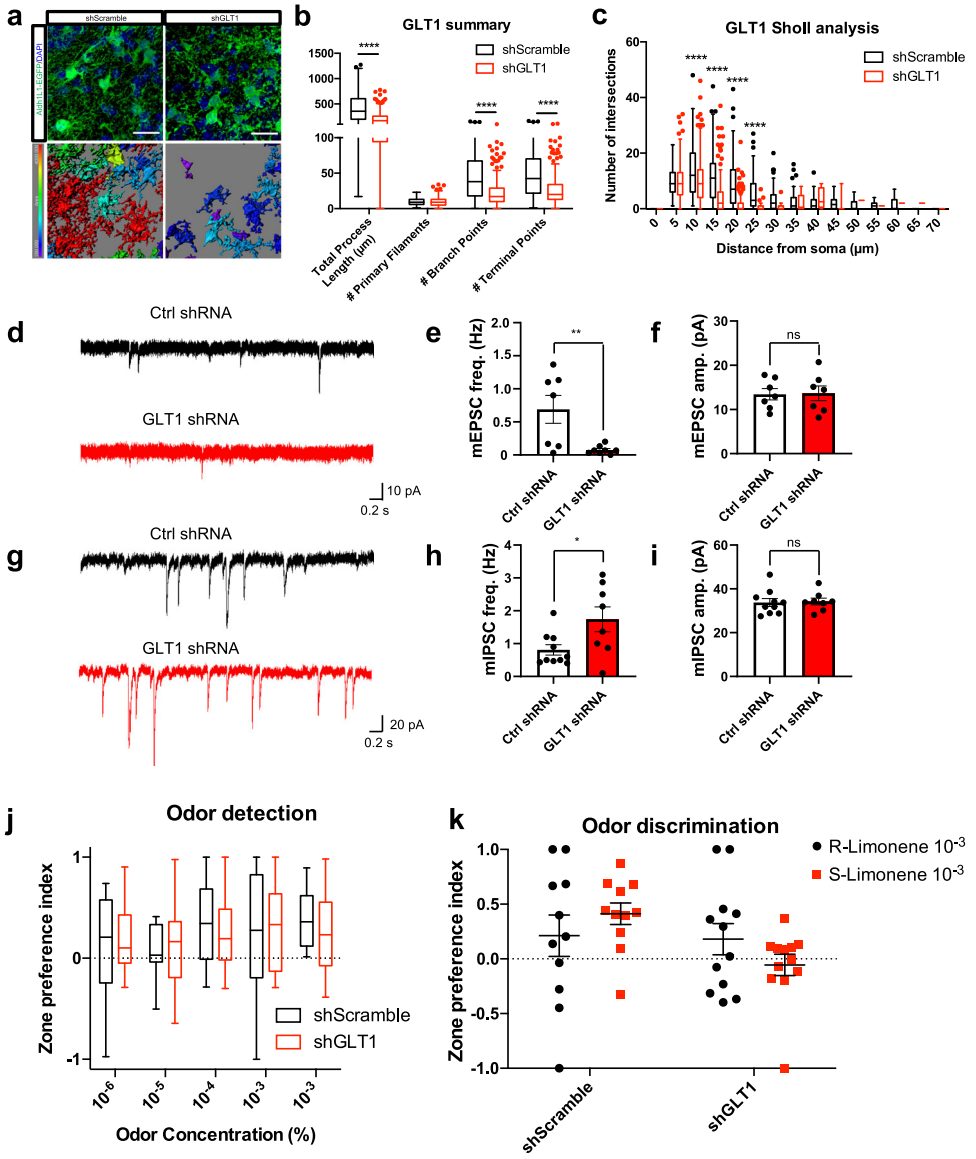


Fig. 6 GLT-1 knockdown partially recapitulates Sox9 KO phenotypes. a–c High-resolution imaging and surface rendering of astrocytes in OB shows a decrease in morphological branching in shGLT1 vs shScramble. $n = 256$ cells (shGLT1) and $n = 138$ cells (shScramble) from $N = 3$ mice, respectively. ****$p < 0.0001$; 2-way ANOVA with Sidak's multiple comparison correction. Quantification of (**a**) represented by box plots displaying interquartile range and median with Tukey whiskers. Data are presented as mean values ± SEM. Scale bar, 20 µm. **d** Example traces of mEPSC recordings in M/T cells with shScramble control injections (top) and shGLT1 KD injections (bottom). **e** M/T cells with shGLT1 injections show a significant decrease in mEPSC frequency compared to control injections. n = 7 cells (shScramble) and $n = 7$ cells (shGLT1) from $N = 4$ mice, respectively. **$p = 0.0084$. Two-tailed Student's t-test. Data are presented as mean values ± SEM. **f** M/T cells show no changes in mEPSC amplitude with shGLT1 injections. $n = 7$ cells (shScramble) and $n = 7$ cells (shGLT1) from $N = 4$ mice, respectively. Two-tailed Student's t-test. Data are presented as mean values ± SEM. **g** Example traces of mIPSC recordings in M/T cells with shScramble control injections (top) and shGLT1 KD injections (bottom). **h** M/T cells with shGLT1 injections show a significant increase in mIPSC frequency compared to control injections. $n = 10$ cells (shScramble) and $n = 7$ cells (shGLT1) from $N = 4$ mice, respectively. *$p = 0.0257$. Two-tailed Student's t-test. Data are presented as mean values ± SEM. (**i**) M/T cells show no changes in mIPSC amplitude with Sox9 KO in astrocytes. $n = 10$ cells (shScramble) and n = 7 cells (shGLT1) from $N = 4$ mice, respectively. Data are presented as mean values ± SEM. **j** Quantification of 3 compartment place preference assay. $n = 12$ (shGLT1) and n = 11 (shScramble). Two-way RM ANOVA with Bonferroni's multiple comparison test (main effect of group, $F(1,21) = 0.0002768$, $p = 0.9869$; group X concentration interaction, $F(4,84) = 0.2148$, $p = 0.9295$). Data are presented as box plots displaying interquartile range and median with Tukey whiskers. **k** Whisker plot quantifying three chamber place preference during odor discrimination. $n = 12$ (shGLT1) and $n = 11$ (shScramble). Two-way RM ANOVA with Bonferroni's multiple comparison test (main effect of odor, $F(1,21) = 0.02911$, $p = 0.8662$; group X odor interaction, $F(1,21) = 4.663$, $p = 0.0425$). Data are shown as mean ± s.e.m.

between the OB and cortex, suggesting that Sox9 may play alternative roles in astrocytes across brain regions. Indeed recent studies from our group revealed that NFIA plays a selective role in maintaining astrocyte function in the adult hippocampus, but not in the OB, cortex, or brainstem[20]. Together, these findings suggest that astrocyte function is regulated by region-sepcific transcriptional codes, where astrocytes from diverse brain regions exhibit unique transcriptional dependencies.

Nevertheless, the downregulation of genes linked to key physiological and homeostatic functions of astrocytes (Fig. 5a, b)

indicates that Sox9 continues to play a key role in astrocyte function through adulthood (Figs. 2–4). The consequences of such Sox9-dependent transcriptional changes extend beyond the cell autonomous functions of astrocytes, as neuronal properties within the olfactory circuit, sensory response maps, and ultimately olfactory behaviors were altered. Together, these findings provide a molecular, cellular, and physiological framework for dissecting how transcriptional mechanisms within astrocytes influence neuronal circuit processing that can likely be extended to other brain regions. Critically, how diverse cellular functions of astrocytes are regulated at the transcriptional level have remained poorly defined. Recent studies have highlighted the regional and local diversity of astrocytes[18,44,51,57], and it will be important to decipher whether this diversity is encoded in part, by specific transcription factors.

Sensory maps are established and maintained through multiple mechanisms[58], ranging from developmental molecular signaling cues to activity-dependent refinement underlying synaptic plasticity. Our studies reveal a potential role for astrocytes in sensory response maps within the OB. We observed that *Sox9* KO resulted in increased OSN density at glomeruli accompanied by olfactory behavior characterized by increased olfactory sensitivity and decreased discrimination. It is well established that Sox9 expression is exclusively expressed in duct/gland cells in the olfactory epithelium but not in OSNs in both rodent and human[59–61]. Increased innervation from OSNs to glomeruli after *Sox9* cKO in OB astrocytes suggests that OSNs are also under astrocyte-mediated regulation. The increased OSN innervation may contribute to the increased olfactory sensitivity because of the increased signal input[62–64].

Glomerular structures include astrocyte cell bodies that reside along their periphery, astrocytic processes enclosing neuropil in a central-synaptic subcompartment[65]. Astrocytes of the same glomerulus form a large multicellular syncytium through gap junctions located at their perisynaptic processes[66], which can lead to single unit functional glial network responses characterized by calcium waves that propagate through astrocyte clusters within odor-activated glomeruli[67,68]. The anatomical arrangement of astrocytes at glomeruli coupled via glial networks may serve to constrain M/T cells responses, as revealed through a decrease in current-evoked firing rate of M/T cells (Fig. 4a–d) as well as synaptic events (Fig. 4e–j). However, we also observed increased activated area of M/T cells (Fig. 3d–f) which is counterintuitive to the decreased firing rate. The decrease in inhibitory inputs (Fig. 4h–i) may explain these contrasting results, as inhibitory inputs contribute to M/T cell selectivity[69] and are closely tied to lateral inhibition and contrast enhancement[32,50]. Overall synchrony between astrocyte anatomy, spatial localization, and range of functions may coordinate effects onto neurons at the cellular level through neuron-astrocyte interactions, which then manifests into circuit-level phenomena.

From these data, we consider a model in which central astrocyte transcriptional regulation is important in maintaining sensory circuits through expression of receptors and transporters for homeostatic mechanisms to threshold neuronal responses. Upon *Sox9* deletion, we observed altered sensory maps and behavioral phenotypes. These roles may be maintained by a combination of precise glomerular structure, synaptic stability, and the reuptake of glutamate from the synaptic cleft. With a decrease in morphological complexity and a reduction in GLT-1 expression, reuptake of glutamate is impaired. The clearance of extracellular glutamate is mostly the responsibility of glial glutamate transporters[70,71]. Knockdown of GLT-1 confirmed that some of the phenotypes seen in *Sox9* KO such as loss of morphological complexity (Figs. 1e–g and 6a–c) and excitatory synaptic stability (Figs. 4e–g and 6d–f) is, in part, due to the loss of GLT-1. The imperfect phenocopy of GLT-1 KD to *Sox9* KO phenotypes highlights the widespread effects of loss of a key transcription factor via dysregulation of its downstream targets and the concomitant compensatory mechanisms. Interestingly, GLT-1 KD also resulted in independent compensatory mechanisms as seen by an increase in inhibitory synaptic stability (Fig. 6g–i). A possible consideration is that although previous studies indicate neuronal GLT-1 KO mice have normal perfomances on a wide variety of behavior tests[72], non-specific expression of GLT-1 shRNA and Ef1a-turboRFP might result in certain level of the metabolic stress in both astrocytes and neurons[73], and introduce extra variations into the astrocyte-neuron coordination.

Taken together, these experiments expand our current understanding of the roles for Sox9 in mature, adult astrocytes and their functions in neuronal circuit processing; rather than a neurocentric view, sensory circuits include a functional and cooperative role for astrocytes and their neuronal constituents in establishing and regulating the integration of sensory input in a multidimensional system. Overall, our study reinforces the need to examine interactions between multiple cell types toward unraveling how these interactions contribute towards sensory circuit function. To fully understand the complexity of how the brain shapes behavior, further investigation into glia subtypes and their interactions with neurons is imperative for processing the wide array of inputs into neuronal circuits.

Methods

Experimental mouse model. All procedures performed on mice were carried out in accordance with the ethical guidelines of the National Institutes of Health and approved by the institutional review board (IACUC Baylor College of Medicine) under protocol #AN-5596. All mice were housed with food and water available ad libitum in a 12-h light/dark environment. Both male and female mice were used for all experiments, and mice were randomly allocated to experimental groups. For ex vivo and in vivo experiments, adult mice aged >8 weeks were used, unless otherwise described.

Method details

Plasmid generation. For GLT-1 shRNAi knockdown experiments, AAV shRNA delivery plasmids were designed based on a previous study[20]. In summary, AAV shRNA delivery backbone was acquired from Addgene (Addgene #85741)[74]. For GLT-1 RNAi, the dsDNA fragment containing target sequence against mouse GLT-1 (5′- GCTCTCACTGACTGTGTTT-3′)[56] and the EFi1 promoter sequence followed by TurboRFP coding region were synthesized and cloned into BamHI and EcoRV sites of parental backbone next to the U6 promoter, resulting in the shGLT1 construct. For the Scramble control, original scramble sequence (5′-GTTCA-GATGTGCGGCGAGT-3′) under the U6 promoter was retained, but the EF1a promoter sequence followed by turboRFP coding region were cloned into SalI and EcoRV sites of parental backbone.

Stereotaxic microinjection of adeno-associated viruses. Surgical procedures were conducted under general anesthesia using Ketamine/dexdormitor (75 mg/kg and 0.5 mg/kg respectively) induction and maintenance under volatile isoflurane inhalation (maintenance at 1–2.5% v/v). Depth of anesthesia was monitored continuously and adjusted when necessary. Following induction of anesthesia, the mice were fitted into a stereotaxic frame with their heads secured by blunt ear bars and their noses placed into an anesthesia and ventilation system. Mice were administered 5 mg/kg of meloxicam subcutaneously prior to surgery. The surgical site was then cleaned three times with 10% iodine and 70% isopropanol (v/v). Skin incisions were made, followed by craniotomies of 2–3 mm in diameter above the olfactory bulb using a small steel burr (Hager & Meisinger GmbH) powered by a high-speed drill (Vector Mega Torque). Bilateral viral injections in the olfactory bulb were carried out by using a stereotaxic apparatus (Leica Biosystems) to guide the placement (from bregma: ML, ±0.9 mm; AP, 3.82 mm; and 0.65 mm down from the surface of the OB) of beveled glass pipettes (3-000-203-G/X, Drummond Scientific Company). Adeno-associated viruses (AAVs) were injected by using a syringe pump (Nanoject II, Drummond Scientific Company) at a rate of 69 nL/s at 25 s intervals 10 times to obtain uniform labeling of astrocytes. Glass pipettes were left in place for at least 5 min prior to slow withdraw. Surgical wounds were closed with surgical nylon monofilament sutures. Mice were allowed to recover overnight in cages placed partially on a low-voltage heating pad. Meloxicam was administered once a day for 3 days after surgery. Virus injected mice were euthanized two to three weeks post-surgery for in vivo widefield imaging, live slice imaging, or perfused for immunohistochemistry. AAVs encoding flexed-GCaMP6m, iCre-P2a-TurboRFP, or iGluSnFR under the GFAP promoter (serotype 2/9 or DJ8,

~2.5×10^{12} genome copies/mL), shScramble or shGLT1 (serotype 2/9, ~1.5×10^{12} genome copies/mL) were cloned and packaged in house.

Tamoxifen treatment. For the experiments, Tamoxifen (Sigma, T5648) was dissolved in corn oil (Sigma, C8267) at 30 mg/ml. At 4 weeks old, 150 mg/kg Tamoxifen was given to both control and cKO mice by oral gavage twice a day for 5 days. Mice were allowed to recover for a week, and then 150 mg/kg Tamoxifen were given twice a day for another 5 days.

Immunohistochemistry and confocal imaging. For confocal imaging, animals were deeply anesthetized using isoflurane, followed by intracardial perfusion of phosphate buffered saline (PBS) and 4% PFA in PBS (pH 7.35). Brains were harvested immediately after perfusion. The tissues were then fixed for 8 h in 4% PFA in PBS and cryopreserved by overnight incubations in 20% sucrose. Tissues were embedded in OCT compound (Fisher HealthCare) and sectioned. For immunohistochemistry analysis of different brain regions, 30 µm sections were collected with a cryostat and stained as floating sections. For antigen retrieval, sections were incubated in Sodium Citrate Buffer (10 mM, 0.05% Tween 20, pH 6.0) at 75 °C for 15 min. Sections were then blocked for 20 min in 10% goat serum or donkey serum in PBS with 0.3% Triton X-100, followed by incubation with primary antibody dilutions in blocking buffer at 4 °C overnight. Primary antibodies were used at the following concentrations: anti-GFP (ab13970, abcam, 1:1000), α-Sox9 (Ab5535, Millipore, 1:1000), and α-OMP (019-22291, Wako, 1:8000). Secondary antibody incubation (647 α-goat, #A21477, Lot 2045332, Life Technologies, 1:500;647 α-chicken, #A-21449, ThermoFisher, 1:500; 647 α-rabbit, #A21244, Lot 1990307, LifeTechnologies, 1:500) was performed in the blocking solution with 0.1% Triton X-100 at room temperature for 1 hr. Sections were washed between incubations with PBS containing 0.1% Triton X-100. DAPI was included in the penultimate wash. Imaging for morphological analysis was performed using Zeiss Imager M2 and Z1 fluorescence microscope equipped with a Zeiss AxioCam camera. Analysis was performed using ZEN 3.1 and ImageJ software.

To measure astrocyte morphology, fluorescent images were acquired using a Zeiss LSM 880 laser scanning confocal microscope with 63× oil immersion objective with frame size at 1024 × 1024 and bit depth at 12. Serial images in the z-axis were taken at an optical step of 1 mm, with overall z-axis range encompassing the whole section. Images were imported to Imaris Bitplane software, and only astrocytes with their soma between the z-axis range were chosen for further analysis. We performed 3D surface rendering (Figs. 1e, h, 6a, and S3a) using the Imaris Surface module. Morphological analysis was performed using the Imaris Filament module. Astrocyte branches and processes were outlined by Autopath with starting point set at 8 mm and seed point set at 0.5 mm. Data were generated from 3 brain sections per region per mouse with 3 mice per genotype. For viral-mediated KO or KD animals, only viral infected cells were selected for the morphology analysis. To analyze number of astrocytes, fluorescent images were acquired using a Zeiss LSM 880 laser scanning confocal microscope with 20× objective. Cell numbers were quantified by the QuPath software Cell Detection function[75].

Olfactory marker protein (OMP) was quantified using Imaris 9.7 from 40 µm z-stacks. Briefly, a mask was drawn to include only the glomerular layer of the olfactory bulb within each section. OMP was detected by thresholding fluorescence intensity values within this mask. A 3D surface object encompassing the thresholded OMP was created. This surface was then normalized using either total number of distinct glomeruli (counted by the researcher) or by DAPI+ cells quantified by Imaris within the glomerular layer mask. Normalized values were then graphed using GraphPad Prism version 9.1

Calcium imaging. In vivo wide-field calcium imaging was performed in anesthetized (urethane, 1.2 µm/kg) head-fixed animals (8–14 weeks old) through thinned skulls 2–3 weeks after viral injection. Animals were kept warm with a portable heating pad and a local anesthetic (bupivicane, 0.5%) was applied to the incision areas. Sensory evoked responses were acquired with a Leica M205FA microscope at 6x magnification, a GFP filter set and a Leica FL6000 fluorescence light source. Optical signals were recorded for 10 s per trial at 464 × 346 pixel resolution. A CCD camera (DFC360 FX, Leica) captured images at a frame rate of 10 Hz and videos were digitized at 12 bits using Leica Application Suite software. Odorants were presented using a custom-made olfactometer (stimulus duration, 3 s) with separate lines and were presented as ~1% saturated vapor, adjusted for vapor pressure. The odors were presented in a random order with at least three trials per odorant at interstimulus intervals ≥60 s.

For two-photon calcium imaging, mice were deeply anesthetized with isoflurane and then perfused with cold artificial cerebrospinal fluid (ACSF, in mM:125 NaCl, 25 glucose, 25 $NaHCO_3$, 2.5 KCl, 2 $CaCl_2$, 1.25 NaH_2PO_4, and 1 $MgCl_2$, pH 7.3, 310–320 mOsm). The brain was dissected, embedded in low melting point agarose, and placed in an ice-cold sucrose-based cutting solution (in mM: 87 NaCl, 2.5 KCl, 1.6 NaH_2PO_4, 25 $NaHCO_3$, 75 sucrose, 10 glucose, 1.3 ascorbic acid, 0.5 $CaCl_2$, 7 $MgCl_2$). 300 µm thick coronal olfactory bulb slices were sectioned on a vibratome (VT1200, Leica). Slices were then recovered in oxygenated ACSF (37 °C) for 15 min and allowed to acclimate to room temperature for at least 15 min before imaging.

We recorded calcium traces using a two-photon resonant microscope equipped with a Chameleon Ultra (II) Ti-sapphire laser (Coherent) tuned to 900 nm through a 20×, 1.0 NA Zeiss objective. Calcium activity was typically sampled at ~1 Hz. Optical signals were recorded for ~5 min per trial at 1024 × 1024 pixel resolution. We recorded data from astrocytes at depths of ~30 µm below the surface. All multiphoton imaging experiments were performed within 2–4 h of slicing.

For ex vivo wide-field imaging, slices were prepared as described above for two-photon imaging. Optical signals were recorded for 10 s per trial at 1392 × 1040 resolution with 4 × 4 binning. A CCD camera (QIcam Fast 1934, QImaging) capture images at a frame rate of ~35 Hz and videos were digitized at 8 bit using Q Capture Pro 7. Glutamate (500 mM in ACSF) was presented through puff application using a FemtoJet 4× with Pi = 1.5 psi and $P_c = 0.07$ psi for 500 ms. Data were analyzed in ImageJ by measuring the intensity of a region of interest (ROI) exhibiting a response from glutamate and in MATLAB with the Curve Fitting Toolbox.

Whole-cell patch clamp electrophysiology. Animals were deeply anesthetized with halothane. After decapitation, the brain was quickly excised from the skull and submerged in an ice-cold cutting solution (in mM: 130 NaCl, 24 $NaHCO_3$, 1.25 NaH_2PO_4, 3.5 KCl, 1.5 $CaCl_2$, 1.5 $MgCl_2$, and 10 D(+)-glucose, pH 7.4). 300 µm sagittal slices were cut using a vibratome (DSK Linear Slicer, Kyoto, Japan) with a blade (DORCO, Seoul, Korea) and transferred to oxygenated ACSF solution (in mM: 130 NaCl, 24 $NaHCO_3$, 1.25 NaH_2PO_4, 3.5 KCl, 1.5 $CaCl_2$, 1.5 $MgCl_2$, and 10 D(+)-glucose, pH 7.4).

Whole-cell recordings were made from mitral, granule cells, and astrocytes somata located in the olfactory bulb. For action potential measurement, mitral and granule cells were patched with an internal solution (in mM): 140 K-gluconate, 10 HEPES, 7 NaCl, and 2 MgATP adjusted to pH 7.4 with CsOH and their membrane potential were set at −60 mV. The current was injected from 0 to 80 pA for 50 and 500 ms. For passive conductance measurement, astrocytes were patched with an internal solution (in mM): 140 K-gluconate, 10 HEPES, 7 NaCl, and 2 MgATP adjusted to pH 7.4 with CsOH and their membrane potential were set at −60 mV. The voltage was injected from −120 to 120 mV for 1 s. For miniature excitatory postsynaptic currents (mEPSCs), M/T cells in oxygenated ACSF containing 0.5 µM TTX and 20 µM Bicuculline were patched with an internal solution (in mM): 135 $CeMeSO_4$, 8 NaCl, 10 HEPES, 0.25 EGTA, 1 Mg-ATP, 0.25 Na_2-GTP, and 30 QX-314 adjusted to pH 7.2 with CsOH. For miniature inhibitory postsynaptic currents (mIPSCs), M/T cells in oxygenated ACSF containing 0.5 µM TTX, 50 µM AVP, and 20 µM CNQX were patched with an internal solution (in mM): 135 CsCl, 4 NaCl, 0.5 $CaCl_2$, 10 HEPES, 5 EGTA, 2 Mg-ATP, 0.5 Na_2-GTP, and 30 QX-314 adjusted to pH 7.2 with CsOH. mEPSCs and mIPSCs were recorded in the presence of TTX. Pipette resistance was typically 4–6 MΩ. Electrical signals were digitized and sampled at 50 µs intervals with Digidata 1550B and Multiclamp 700B amplifier (Molecular Devices) using pCLAMP 10.4 software. Data were filtered at 2 kHz.

For astrocyte glutamate transporter current recording, $Sox9^{fl/fl}$ and $Sox9^{+/+}$ mice with AAV-GFAP-iCre-P2a-TurboRFP injection in olfactory bulbs were used. Slices were prepared as described above for two-photon. RFP + astrocytes were patched in whole-cell voltage clamp configuration with an internal solution (in mM): 120 K-Gluconate, 20 HEPES, 10 EGTA, 2 MgATP, and 0.2 NaGTP adjusted to pH 7.2 and 295 mOsm. Pipette resistance was 6–8 MΩ. ACSF included CNQX (20 µM), APV (50 µM), BIC (10 µM), and TTX (1 µM). Astrocytes (~50–75 µm deep from surface) were held at −80 mV and continually monitored for changes in access resistance. Recordings with a change in access resistance of more than 25% were excluded. To evoke transporter currents, glutamate (500 mM in ACSF) was presented through puff application perpendicular to flow of ACSF using a FemtoJet 4x with $_{Pi} = 0.2–0.8$ psi and $P_c = 0–0.07$ psi for 500 ms at 50–100 µm from the patched astrocyte soma in the same plane. Glass pipettes for delivering the puff solution had resistances of 1–2 MΩ. In total 10–20 trials were recorded at baseline then TBOA (100 µM) was applied to block glutamate transporter currents. Transporter currents were quantified as the average of the trials after complete wash on of TBOA subtracted from the average of the trials before TBOA application. Kinetics of the puff-evoked transporter currents were quantified as the fast time constant of a biexponential fit of the subtracted current.

Single cell RNA-seq analysis. For single cell sequencing analysis, we have used our previously published dataset with the accession number GEO: GSE121891[35]. Matrices from each experiment were imported into Seurat (version 2.2.1)[76]. The minimum gene per cell threshold was set to 200 and maximum gene per cell threshold was set to 2500 for inclusion into the final digital expression matrix. Immediate early genes were removed from differentially expressed genes[77] before canonical correlation analysis (CCA) which was used to scale and merge datasets from each experimental batch to account for batch effects[76]. Two-dimensional visualization of the multi-dimensional data set was done with t-SNE. Differential expression of the individual clusters was performed using the likelihood-ratio test for single cell gene expression (Seurat FindMarkers function, default parameters).

Cell dissociation and FAC-sorting of astrocytes. $Sox9^{fl/fl}$ and $Sox9^{+/+}$ mice with AAV-GFAP-iCre-P2a-TurboRFP injection in olfactory bulbs were used to isolate astrocytes by fluorescence-activated cell sorting (FACS). Four weeks after the injection, olfactory bulbs from the mice were dissociated following published protocols[51] with slight modifications. Briefly, the olfactory bulbs from 6 mice (3 control and 3 KO males) were dissected and digested for 15 min at 37 °C with

0.5 mL papain solution (1x EBSS (Worthington), 230 U/ml DNase (Worthington), 25 U/ml papain (Worthington)) in 1.5 mL microcentrifuge tubes on the thermomixer with 1400 rpm shaking for agitation. After digestion, the tissue was neutralized with DMEM/F12 + 10% FBS solution (ThermoFisher) and centrifuged at RT at 4200 × *g* for 5 min. The resultant pellet was washed by PBS and re-suspended in FACS buffer (Leibovitz's L-15 Medium with 0.01 M HEPES, 0.0025% DNaseI), and filtered with tubes with cell-strainer caps (FALCON). FACS was performed in a FACSAria I (BD Bioscience, 100-µm nozzle and 20-p.s.i. setting), and astrocytes were separated by TurboRFP. FAC-sorted cells were collected in RLT lysis buffer (QIAGEN) with 1% beta-mercaptoethanol.

Bulk RNA extraction, library preparation, and sequencing. RNA was extracted from FACS pelleted cells using RNeasy Micro Kit (Cat. No. 74004, QIAGEN). RNA integrity (RIN ≥ 8.0) was confirmed using the High Sensitivity RNA Analysis Kit (DNF-472-0500, Agilent formerly AATI) on a 12-Capillary Fragment Analyzer. Illumina sequencing libraries with 8-bp single indices were constructed from 10 ng total RNA using the Trio RNA-Seq System (0507-96, NuGEN). The resulting libraries were validated using the Standard Sensitivity NGS Fragment Analysis Kit (DNF-473-0500, Agilent formerly AATI) on a 12-Capillary Fragment Analyzer. Equal concentrations (2 nM) of libraries were pooled and subjected to sequencing of approximately 40 million reads per sample using the High Output v2 kit (FC-404-2002, Illumina) on a NextSeq550 following the manufacturer's instructions.

qRT-PCR. Real time quantitative PCR was carried out using Powerup SYBR green master mix (A25742, ThermoFisher) and a Quant Studio 3 real-time thermo cycler (Applied Biosystems). Primer sets listed in Supplementary Table 1 were used to specifically amplify their respective targets. Each sample was run in triplicate and with negative control (without cDNA). Sample amplification curves were filtered based on internal quality control parameters for specificity and passive reference ROX dye was used normalize for optical path differences. Data analysis was done using the $\Delta\Delta C_T$ method[78] with all data normalized to ActinB or GAPDH expression.

Three compartment place preference assay. Mice received viral injections at least 4 weeks prior to behavioral experiments. Mice were acclimated and familiarized to the testing chamber for 5 min each day for three days prior to testing. For odor detection threshold, odor concentrations were tested for 2 min each in ascending order of concentration with 1 min between each. For odor discrimination, a habituation-dishabituation assay was used in which mice were habituated to an odor for 3 trials before being exposed to a novel odor. Each trial lasted 2 min with 1 min between each trial. Video was captured with a Doric GigE Behavior Tracking Camera (BTC_GigE_CO) and position tracking was performed with semi-automated analysis with OptiMouse through MATLAB. Analysis of these behavior data were performed blind and objectively through OptiMouse software in MATLAB.

Quantification and statistical analysis. For wide-field calcium imaging, all data analysis was performed with custom MATLAB scripts and processed in ImageJ. Initial data processing included averaging trials and visually aligning the region of interest (dorsal olfactory bulb). Δ*F* maps were created by temporally averaging the entire 3 s odor stimulation period and subtracting the temporal average of the 2 s immediately preceding odor onset. Δ*F*/*F* maps were additionally normalized by the first five frames of the averaged trial. There was no appreciable photobleaching of the GCaMP3 signals during the experiments. For quantification, ROIs approximately the size of a glomerulus were set over activated regions with at least 3 ROIs per odorant. For two-photon data processing, all analysis was performed in custom MATLAB scripts.

For two-photon imaging of astrocyte microdomains, ROIs were generated posthoc with GECIquant plugin in FIJI and time analysis was performed with custom MATLAB scripts.

Sequencing files were de-multiplexed and the resulting fastq files were merged. Quality control was performed using fastQC (v0.10.1) and MultiQC (v0.9). Reads were mapped to the mouse genome mm10 assembly using STAR (v2.5.0a). BAM files were normalized for sequencing depth using samtools (v.1.3). Bioconductor packages GenomicAlignments (v1.16.0) and GenomicFeatures (v1.32.2) were used to build count matrices. Differential expression and normalized count values were determined using DESeq2 (v1.20.0) in R (v 3.5.2). GO analyses were performed by Enrichr website.

Reporting summary. Further information on research design is available in the Nature Research Reporting Summary linked to this article.

Data availability

The datasets generated during and/or analyzed during the current study that are necessary to interpret, verify, and extend the research are provided in Figs. 1–6, Supplementary Figs. 1–6, Supplementary Table 1, and the Source Data file. The single-cell RNA sequencing data used in this study are available in the GEO database under accession code GSE121891. The FACS-sorted RNA sequencing data generated in this study have been deposited in the GEO database under accession code GSE180841. All other additional information and reagents will be available from the corresponding author upon reasonable request. Source data are provided with this paper.

Code availability

The code used to analyze data are freely available on Github (github.com/arenkiellab).

Received: 16 March 2020; Accepted: 11 August 2021;
Published online: 01 September 2021

References

1. Sofroniew, M. V. & Vinters, H. V. Astrocytes: biology and pathology. *Acta Neuropathol.* **119**, 7–35 (2010).
2. Magistretti, P. J. Neuron-glia metabolic coupling and plasticity. *J. Exp. Biol.* **209**, 2304–2311 (2006).
3. Higashimori, H. & Sontheimer, H. Role of Kir4.1 channels in growth control of glia. *Glia* **55**, 1668–1679 (2007).
4. Bordey, a, Hablitz, J. J. & Sontheimer, H. Reactive astrocytes show enhanced inwardly rectifying K+ currents in situ. *Neuroreport* **11**, 3151–3155 (2000).
5. Amédée, T., Robert, A. & Coles, J. A. Potassium homeostasis and glial energy metabolism. *Glia* **21**, 46–55 (1997).
6. Newman, G. C. et al. Effects of K+, pH and glutamate on 45Ca kinetics in hippocampal brain slices. *J. Neurosci. Methods* **59**, 111–120 (1995).
7. Haydon, P. G. & Carmignoto, G. Astrocyte control of synaptic transmission and neurovascular coupling. *Physiol. Rev.* **86**, 1009–1031 (2006).
8. Otsu, Y. et al. Calcium dynamics in astrocyte processes during neurovascular coupling. *Nat. Neurosci.* **18**, 210–218 (2014).
9. Schousboe, A. Metabolic signaling in the brain and the role of astrocytes in control of glutamate and GABA neurotransmission. *Neurosci. Lett.* **689**, 11–13 (2018).
10. Bergles, D. E. & Jahr, C. E. Glial contribution to glutamate uptake at Schaffer collateral-commissural synapses in the hippocampus. *J. Neurosci.* **18**, 7709–7716 (1998).
11. Vargova, L. & Sykova, E. Astrocytes in control of the biophysical properties of extracellular space. in *Astrocytes in (Patho)Physiology of the Nervous System* 225–250 (2009).
12. Eroglu, C. & Barres, B. A. Regulation of synaptic connectivity by glia. *Nature* **468**, 223–231 (2010).
13. Hanson, E. et al. Astrocytic glutamate uptake is slow and does not limit neuronal NMDA receptor activation in the neonatal neocortex. *Glia* **63**, 1784–1796 (2015).
14. Araque, a, Sanzgiri, R. P., Parpura, V. & Haydon, P. G. Astrocyte-induced modulation of synaptic transmission. *Can. J. Physiol. Pharmacol.* **77**, 7 (1999).
15. Stogsdill, J. A. et al. Astrocytic neuroligins control astrocyte morphogenesis and synaptogenesis. *Nature* **551**, 192–197 (2017).
16. Perez-Alvarez, A., Navarrete, M., Covelo, A., Martin, E. D. & Araque, A. Structural and functional plasticity of astrocyte processes and dendritic spine interactions. *J. Neurosci.* **34**, 12738–12744 (2014).
17. Perea, G., Navarrete, M. & Araque, A. Tripartite synapses: astrocytes process and control synaptic information. *Trends Neurosci.* **32**, 421–431 (2009).
18. Chai, H. et al. Neural circuit-specialized astrocytes: transcriptomic, proteomic, morphological, and functional evidence. *Neuron* **95**, 531–549.e9 (2017).
19. Haim, L. & Rowitch, D. Functional diversity of astrocytes in neural circuit regulation. *Nat. Rev. Neurosci.* **18**, 31–41 (2017).
20. Huang, A. Y. S. et al. Region-specific transcriptional control of astrocyte function oversees local circuit activities. *Neuron* **106**, 992–1008.e9 (2020).
21. Graziadei, P. P. C. & Graziadei, G. A. M. Neurogenesis and neuron regeneration in the olfactory system of mammals. I. Morphological aspects of differentiation and structural organization of the olfactory sensory neurons. *J. Neurocytol.* **8**, 1–18 (1979).
22. Hong, W. & Luo, L. Genetic control of wiring specificity in the fly olfactory system. *Genetics* **196**, 17–29 (2014).
23. Mombaerts, P. et al. Visualizing an olfactory sensory map. *Cell* **87**, 675–686 (1996).
24. Serizawa, S. et al. A neuronal identity code for the odorant receptor-specific and activity-dependent axon sorting. *Cell* **127**, 1057–1069 (2006).
25. Ishii, T. et al. Monoallelic expresion of the odourant receptor gene and axonal projection of olfactory sensory neurones. *Genes Cells* **6**, 71–78 (2001).
26. Nishizumi, H. & Sakano, H. Developmental regulation of neural map formation in the mouse olfactory system. *Dev. Neurobiol.* **75**, 594–607 (2015).
27. Bozza, T., McGann, J. P., Mombaerts, P. & Wachowiak, M. In Vivo Imaging of Neuronal Activity by Targeted Expression of a Genetically Encoded Probe in the Mouse. *Neuron* **42**, 9–21 (2004).

28. Wachowiak, M., Denk, W. & Friedrich, R. W. Functional organization of sensory input to the olfactory bulb glomerulus analyzed by two-photon calcium imaging. *Proc. Natl Acad. Sci.* **101**, 9097–9102 (2004).
29. Soucy, E. R., Albeanu, D. F., Fantana, A. L., Murthy, V. N. & Meister, M. Precision and diversity in an odor map on the olfactory bulb. *Nat. Neurosci.* **12**, 210–220 (2009).
30. Iwasato, T. et al. NMDA receptor-dependent refinement of somatotopic maps. *Neuron* **19**, 1201–1210 (1997).
31. Gordon, J. A. & Stryker, M. P. Experience-dependent plasticity of binocular responses in the primary visual cortex of the mouse. *J. Neurosci.* **16**, 3274–3286 (1996).
32. Quast, K. B. et al. Developmental broadening of inhibitory sensory maps. *Nat. Neurosci.* **20**, 189–199 (2017).
33. Stolt, C. C. The Sox9 transcription factor determines glial fate choice in the developing spinal cord. *Genes Dev.* **17**, 1677–1689 (2003).
34. Kang, P. et al. Sox9 and NFIA Coordinate a Transcriptional Regulatory Cascade during the Initiation of Gliogenesis. *Neuron* **74**, 79–94 (2012).
35. Tepe, B. et al. Single-cell RNA-seq of mouse olfactory bulb reveals cellular heterogeneity and activity- dependent molecular census of adult-born neurons article single-cell RNA-seq of mouse olfactory bulb reveals cellular heterogeneity and activity-dependent molecular C. *CellReports* **25**, 2689–2703.e3 (2018).
36. Cahoy, J. D. et al. A transcriptome database for astrocytes, neurons, and oligodendrocytes: a new resource for understanding brain development and function. *J. Neurosci.* **28**, 264–278 (2008).
37. Heintz, N. Gene Expression Nervous System Atlas (GENSAT). *Nat. Neurosci.* **7**, 483 (2004).
38. Sun, W. et al. SOX9 is an astrocyte-specific nuclear marker in the adult brain outside the neurogenic regions. *J. Neurosci.* **37**, 4493–4507 (2017).
39. Akiyama, H. The transcription factor Sox9 has essential roles in successive steps of the chondrocyte differentiation pathway and is required for expression of Sox5 and Sox6. *Genes Dev.* **16**, 2813–2828 (2002).
40. Bernardinelli, Y. et al. Astrocytes display complex and localized calcium responses to single-neuron stimulation in the hippocampus. *J. Neurosci.* **31**, 8905–8919 (2011).
41. Stobart, J. L. et al. Cortical circuit activity evokes rapid astrocyte calcium signals on a similar timescale to neurons. *Neuron* **98**, 726–735.e4 (2018).
42. Bindocci, E. et al. Three-dimensional Ca^{2+} imaging advances understanding of astrocyte biology. *Science* **356**, eaai8185 (2017).
43. Srinivasan, R. et al. Ca2+ signaling in astrocytes from Ip3r2−/− mice in brain slices and during startle responses in vivo. *Nat. Neurosci.* **18**, 708–717 (2015).
44. Khakh, B. S. & Deneen, B. The emerging nature of astrocyte diversity. *Annu. Rev. Neurosci.* **42**, 187–207 (2019).
45. Khakh, B. S. & McCarthy, K. D. Astrocyte calcium signaling: From observations to functions and the challenges therein. *Cold Spring Harb. Perspect. Biol.* **7**, a020404 (2015).
46. Clarin, T., Sandhu, S. & Apfelbach, R. Odor detection and odor discrimination in subadult and adult rats for two enantiomeric odorants supported by c-fos data. *Behav. Brain Res.* **206**, 229–235 (2010).
47. Chen, Q. et al. Imaging Neural Activity Using Thy1-GCaMP Transgenic Mice. *Neuron* **76**, 297–308 (2012).
48. Albeanu, D. F. et al. Olfactory marker protein (OMP) regulates formation and refinement of the olfactory glomerular map. *Nat. Commun.* **9**, 5073 (2018).
49. Shepherd, P. N. N. G. M., Oxford University Press, & Ralph Erskine Conrad Memorial Fund. *The Synaptic Organization of the Brain*. (Oxford University Press, 2004).
50. Shepherd, G. M., Chen, W. R., Willhite, D., Migliore, M. & Greer, C. A. The olfactory granule cell: From classical enigma to central role in olfactory processing. *Brain Res. Rev.* **55**, 373–382 (2007).
51. John Lin, C. C. et al. Identification of diverse astrocyte populations and their malignant analogs. *Nat. Neurosci.* **20**, 396–405 (2017).
52. Sreetama, S. C., Takano, T., Nedergaard, M., Simon, S. M. & Jaiswal, J. K. Injured astrocytes are repaired by Synaptotagmin XI-regulated lysosome exocytosis. *Cell Death Differ.* **23**, 596–607 (2015).
53. Li, D., Ropert, N., Koulakoff, A., Giaume, C. & Oheim, M. Lysosomes are the major vesicular compartment undergoing Ca2+-regulated exocytosis from cortical astrocytes. *J. Neurosci.* **28**, 7648–7658 (2008).
54. Verderio, C. et al. TI-VAMP/VAMP7 is the SNARE of secretory lysosomes contributing to ATP secretion from astrocytes. *Biol. Cell* **104**, 213–228 (2012).
55. Marvin, J. S. et al. An optimized fluorescent probe for visualizing glutamate neurotransmission. *Nat. Methods* **10**, 162–170 (2013).
56. Zhang, Y. et al. Generation of a Novel Mouse Model of Parkinson's Disease via Targeted Knockdown of Glutamate Transporter GLT-1 in the Substantia Nigra. *ACS Chem. Neurosci.* **11**, 406–417 (2020).
57. Morel, L. et al. Intracortical astrocyte subpopulations defined by astrocyte reporter Mice in the adult brain. *Glia* **67**, 171–181 (2018).
58. Cang, J. & Feldheim, D. A. Developmental mechanisms of topographic map formation and alignment. *Annu. Rev. Neurosci.* **36**, 51–77 (2013).
59. Holbrook, E. H., Wu, E., Curry, W. T., Lin, D. T. & Schwob, J. E. Immunohistochemical characterization of human olfactory tissue. *Laryngoscope* **121**, 1687–1701 (2011).
60. Packard, A. I., Lin, B. & Schwob, J. E. Sox2 and Pax6 Play counteracting roles in regulating neurogenesis within the murine olfactory epithelium. *PLoS ONE* **11**, e0155167 (2016).
61. Schnittke, N. et al. Transcription factor p63 controls the reserve status but not the stemness of horizontal basal cells in the olfactory epithelium. *Proc. Natl Acad. Sci. USA* **112**, E5068 LP–E5065077 (2015).
62. Youngentob, S. L. & Margolis, F. L. OMP gene deletion causes an elevation in behavioral threshold sensitivity. *Neuroreport* **10**, 15–19 (1999).
63. Youngentob, S. L., Margolis, F. L. & Youngentob, L. M. OMP gene deletion results in an alteration in odorant quality perception. *Behav. Neurosci.* **115**, 626–631 (2001).
64. Youngentob, S. L., Pyrski, M. M. & Margolis, F. L. Adenoviral vector-mediated rescue of the OMP-null behavioral phenotype: enhancement of odorant threshold sensitivity. *Behav. Neurosci.* **118**, 636–642 (2004).
65. Chao, T. I., Kasa, P. & Wolff, J. R. Distribution of astroglia in glomeruli of the rat main olfactory bulb: Exclusion from the sensory subcompartment of neuropil. *J. Comp. Neurol.* **388**, 191–210 (1997).
66. Fujii, Y., Maekawa, S. & Morita, M. Astrocyte calcium waves propagate proximally by gap junction and distally by extracellular diffusion of ATP released from volume-regulated anion channels. *Sci. Rep.* **7**, 13115 (2017).
67. Hirase, H., Qian, L., Barthó, P. & Buzsáki, G. Calcium Dynamics of Cortical Astrocytic Networks In Vivo. *PLoS Biol.* **2**, e96 (2004).
68. Roux, L., Benchenane, K., Rothstein, J. D., Bonvento, G. & Giaume, C. Plasticity of astroglial networks in olfactory glomeruli. *Proc. Natl Acad. Sci. USA* **108**, 18442–18446 (2011).
69. Tan, J., Savigner, A., Ma, M. & Luo, M. Odor Information Processing by the Olfactory Bulb Analyzed in Gene-Targeted Mice. *Neuron* **65**, 912–926 (2010).
70. Petr, G. T. et al. Conditional Deletion of the Glutamate Transporter GLT-1 Reveals That Astrocytic GLT-1 Protects against Fatal Epilepsy While Neuronal GLT-1 Contributes Significantly to Glutamate Uptake into Synaptosomes. *J. Neurosci.* **35**, 5187–5201 (2015).
71. Lehre, K., Levy, L., Ottersen, O., Storm-Mathisen, J. & Danbolt, N. Differential expression of two glial glutamate transporters in the rat brain: quantitative and immunocytochemical observations. *J. Neurosci.* **15**, 1835–1853 (1995).
72. Fischer, K. D. et al. Behavioral phenotyping and dopamine dynamics in mice with conditional deletion of the glutamate transporter GLT-1 in neurons: resistance to the acute locomotor effects of amphetamine. *Psychopharmacol. (Berl.).* **235**, 1371–1387 (2018).
73. McNair, L. F. et al. Deletion of neuronal GLT-1 in mice reveals its role in synaptic glutamate homeostasis and mitochondrial function. *J. Neurosci.* **39**, 4847–4863 (2019).
74. Yu, H. et al. Tet3 regulates synaptic transmission and homeostatic plasticity via DNA oxidation and repair. *Nat. Neurosci.* **18**, 836–843 (2015).
75. Bankhead, P. et al. QuPath: Open source software for digital pathology image analysis. *Sci. Rep.* **7**, 16878 (2017).
76. Butler, A., Hoffman, P., Smibert, P., Papalexi, E. & Satija, R. Integrating single-cell transcriptomic data across different conditions, technologies, and species. *Nat. Biotechnol.* **36**, 411–420 (2018).
77. Wu, Y. E., Pan, L., Zuo, Y., Li, X. & Hong, W. Detecting Activated Cell Populations Using Single-Cell RNA-Seq. *Neuron* **96**, 313–329.e6 (2017).
78. Schmittgen, T. D. & Livak, K. J. Analyzing real-time PCR data by the comparative CT method. *Nat. Protoc.* **3**, 1101–1108 (2008).

Acknowledgements

This work was supported by the NIH (NINDS R01NS078294 and NIDDK R01109934 to B.R.A.; NINDS NS071153, NS096096, and AG071687 to BD), the McNair Medical Institute, and the Charif Souki Fund. We thank the BCM IDDRC (U54HD083092) for viral packaging. K.U. was supported by an NIH F31 Training Fellowship (F31NS089178). E.H. was supported by an NIH T32 Training fellowship (T32NS043124-15). T.H. was supported by a research grant from NMSS (FG-1607-25417). We thank Jay Patel and Jessica Swanson for their comments on the manuscript.

Author contributions

K.U. performed the vector design and cloning, stereotaxic injections, wide-field calcium imaging, wide-field iGluSnFR imaging, two-photon calcium imaging, immunohistochemistry, behavior, analysis, designed experiments, and wrote the manuscript with help from the other authors. T.H. performed morphological analysis and RNAseq library preparation. E.H. and J.W. performed electrophysiological recordings. Y.-T.C. performed the FACS analysis. B.T. performed Drop-seq analysis. B.L. and D.S. performed RNA-Seq and bioinformatics analysis. B.P. performed qPCR and imaging. B.R.A. and B.D. conceived the project and designed experiments.

Competing interests
The authors declare no competing interests.

Additional information
Supplementary information The online version contains supplementary material available at https://doi.org/10.1038/s41467-021-25444-3.

Correspondence and requests for materials should be addressed to B.D. or B.R.A.

Peer review information *Nature Communications* thanks Matthew Grubb and the other anonymous reviewer(s) for their contribution to the peer review of this work.

Reprints and permission information is available at http://www.nature.com/reprints

Publisher's note Springer Nature remains neutral with regard to jurisdictional claims in published maps and institutional affiliations.

Open Access This article is licensed under a Creative Commons Attribution 4.0 International License, which permits use, sharing, adaptation, distribution and reproduction in any medium or format, as long as you give appropriate credit to the original author(s) and the source, provide a link to the Creative Commons license, and indicate if changes were made. The images or other third party material in this article are included in the article's Creative Commons license, unless indicated otherwise in a credit line to the material. If material is not included in the article's Creative Commons license and your intended use is not permitted by statutory regulation or exceeds the permitted use, you will need to obtain permission directly from the copyright holder. To view a copy of this license, visit http://creativecommons.org/licenses/by/4.0/.

© The Author(s) 2021

nature COMMUNICATIONS

ARTICLE

https://doi.org/10.1038/s41467-021-22940-4 OPEN

A neural basis for brain leptin action on reducing type 1 diabetic hyperglycemia

Shengjie Fan[1,2,9], Yuanzhong Xu[2,9], Yungang Lu[2], Zhiying Jiang[2], Hongli Li[2], Jessie C. Morrill[2,3], Jing Cai[2,3], Qi Wu[4], Yong Xu[4], Mingshan Xue[5,6], Benjamin R. Arenkiel[7], Cheng Huang[1]✉ & Qingchun Tong[2,3,8]✉

Central leptin action rescues type 1 diabetic (T1D) hyperglycemia; however, the underlying mechanism and the identity of mediating neurons remain elusive. Here, we show that leptin receptor (LepR)-expressing neurons in arcuate ($LepR^{Arc}$) are selectively activated in T1D. Activation of $LepR^{Arc}$ neurons, Arc GABAergic ($GABA^{Arc}$) neurons, or arcuate AgRP neurons, is able to reverse the leptin's rescuing effect. Conversely, inhibition of $GABA^{Arc}$ neurons, but not AgRP neurons, produces leptin-mimicking rescuing effects. Further, AgRP neuron function is not required for T1D hyperglycemia or leptin's rescuing effects. Finally, T1D $LepR^{Arc}$ neurons show defective nutrient sensing and signs of cellular energy deprivation, which are both restored by leptin, whereas nutrient deprivation reverses the leptin action. Our results identify aberrant activation of $LepR^{Arc}$ neurons owing to energy deprivation as the neural basis for T1D hyperglycemia and that leptin action is mediated by inhibiting $LepR^{Arc}$ neurons through reversing energy deprivation.

[1] School of Pharmacy, Shanghai University of Traditional Chinese Medicine, Shanghai, China. [2] Brown Foundation of Molecular Medicine for the Prevention of Human Diseases of McGovern Medical School, University of Texas Health Science Center at Houston, Houston, TX, USA. [3] MD Anderson Cancer Center & UT Health Graduate School for Biomedical Sciences, University of Texas Health Science at Houston, Houston, TX, USA. [4] Children's Nutrition Research Center, Department of Pediatrics, Baylor College of Medicine, One Baylor Plaza, Houston, TX, USA. [5] Department of Neuroscience and Department of Molecular and Human Genetics, Baylor College of Medicine, Houston, TX, USA. [6] The Cain Foundation Laboratories, Jan and Dan Duncan Neurological Research Institute at Texas Children's Hospital, Houston, TX, USA. [7] Department of Molecular and Human Genetics and Department of Neuroscience, Baylor College of Medicine, and Jan and Dan Duncan Neurological Research Institute, Texas Children's Hospital, Houston, TX, USA. [8] Department of Neurobiology and Anatomy of McGovern Medical School, University of Texas Health Science Center at Houston, Houston, TX, USA. [9] These authors contributed equally: Shengjie Fan, Yuanzhong Xu. ✉email: chuang@shutcm.edu.cn; Qingchun.tong@uth.tmc.edu

Patients with type 1 diabetes (T1D) suffer greatly from uncontrolled hyperglycemia, and insulin delivery remains the only treatment option, but is accompanied with obesity development and life-threatening hypoglycemia. Emerging studies have demonstrated that, in addition to its role in body weight regulation, adipocyte-derived leptin is capable of reducing T1D hyperglycemia in an insulin-independent manner[1,2]. Notably, leptin action in the brain alone is sufficient to restore euglycemia in T1D, while its action in the liver is not required[3,4]. It is generally accepted that brain leptin action on reducing T1D hyperglycemia is mediated by suppressing counter-regulatory responses (CRR)[5]. The CRR includes glucagon, HPA axis, and sympathetic nerve output, representing a major physiological response against hypoglycemic for glucose homeostasis, but is aberrantly activated in T1D. For brain leptin action on reducing glucose in T1D, a role for β-adrenergic receptor-mediated sympathetic nerve output has been ruled out[6,7]. Heightened glucagon action has been suggested to be essential[8], which is later suggested to be dependent on insulin action[9]. The HPA axis has also been suggested to be the mediator[10,11], but also is later suggested not to be a sole mediator[12,13]. It is generally thought that multiple counter-regulator responses are involved and suppression of one of them may not be sufficient in mediating the leptin action[5,12].

Previous studies have shown that leptin receptor (LepR) expression in GABAergic neurons mediates leptin action in reducing hyperglycemia in T1D[6,14]. In line with this, LepR neurons in the ventromedial hypothalamus (VMH), a major brain region containing mainly glutamatergic neurons and known to regulate glucose homeostasis, are not required for the leptin action[15]. However, as both LepR and GABAergic neurons are widely distributed in the brain, the location of GABAergic LepR neurons that mediates leptin's actions on T1D glucose handling remains elusive. Specifically, conflicting results have been obtained regarding leptin action on T1D glucose in the arcuate nucleus (Arc), a region important for glucose homeostasis and known to express abundant LepRs. The melanocortin pathway, which involves proopiomelanocortin (POMC) and agouti-related protein (AgRP) neurons, two well-characterized groups of neurons in the Arc, has been shown to play an important part in mediating leptin action on T1D glucose[16,17]. Although POMC neuron function contributes only marginally, LepRs in AgRP neurons, a group of GABAergic neurons in the Arc, have been shown to contribute significantly to the leptin action[6,18]. Consistently, LepR expression in AgRP neurons greatly reduces hyperglycemia-associated leptin deficiency[19]. In contrast, chemogenetic manipulations of AgRP neuron activity revealed no effects on the leptin action on T1D glucose[20]. Importantly, as AgRP neurons only constitute a relatively small number of the Arc neuron population[21,22], the relative importance of AgRP versus non-AgRP neurons in mediating leptin action on T1D glucose remains untested.

Despite potent effects of leptin action on reducing T1D hyperglycemia, the underlying cellular mechanism remains unclear. The LepR–STAT3 signaling pathway, known to mediate the major part of leptin action on body weight and glucose homeostasis, is required for leptin action in reducing T1D hyperglycemia[7], although other signaling pathways may also play a role[23]. Leptin either activates or inhibits LepR neurons, depending on the types of neuron and their brain location[24–26]. Specifically, most LepR^{Arc} neurons are inhibited by leptin[27,28], although studies focusing on POMC neurons showed that a subset of POMC neurons are activated by leptin[25,29], which may be mediated by direct action or indirectly through leptin inhibition of putative presynaptic inputs onto POMC neurons[21]. It is unknown whether leptin activation or inhibition on LepR neurons mediates its action on T1D glucose. Although leptin action on neuron activation is postulated to be mediated through TRPC channels[30,31], little is known on the cellular mechanisms underlying leptin action on neuronal inhibition related to nutrient supply.

This study shows that LepR^{Arc} neurons are aberrantly activated in T1D models, and that this activation is reversed by leptin. Specific activation of LepR^{Arc}, Arc AgRP neurons, or GABA^{Arc} neurons reverses or abrogates leptin action on T1D glucose handling. Conversely, specific inhibition of GABA^{Arc} neurons causes a leptin-mimicking effect on reducing T1D hyperglycemia, while inhibiting AgRP neurons has a much more attenuated effect. The presence of AgRP neurons is not required for T1D hyperglycemia or for the observed leptin action. Importantly, our results suggest that LepR^{Arc} neurons in T1D are in a state of energy deprivation and not sensitive to nutrient deprivation, both of which are reversed by leptin. Leptin action on reducing T1D hyperglycemia is reversed by nutrient deprivation or activation of nutrient deprivation signaling pathways. These results identify aberrant activation of LepR^{Arc} neurons resulting from loss in response to nutrient supply as one major central mechanism underlying T1D hyperglycemia, and reveal that leptin reduces T1D hyperglycemia through inhibition of these neurons via reversing energy deprivation.

Results

Aberrant activation of LepR^{Arc} neurons in T1D models. T1D exhibits a severe reduction in leptin levels[1,2], suggesting a significant contribution of loss of brain leptin action to the pathogenesis of T1D hyperglycemia. Given the known leptin effect on neuron activity, we explored potential changes in LepR neuron activity in T1D and its modulation by leptin. We examined the expression of c-Fos, a well-established indicator for neuron activity. LepR^{Arc} neurons in mice with severe hyperglycemia and insulin deficiency induced by STZ, a commonly used type 1 diabetes model (STZ-T1D), exhibited greatly increased c-Fos expression in the Arc compared to controls (non-T1D conditions) (Fig. 1a, b, d), even fed ad libitum. Of note, STZ-induced c-Fos expression was largely colocalized in LepR-expressing neurons in the Arc (Fig. 1b and Supplementary Fig. 1), whereas negligible colocalization was found in other brain sites with LepR expression (Supplementary Fig. 1). The c-Fos expression in LepR^{Arc} neurons was significantly reduced by i.c.v. infusion of leptin (Fig. 1c, d), suggesting a potent inhibitory action by leptin on these neurons. In addition, we also observed similar increases in c-Fos and responses to leptin treatment in another, nonobesity diabetic (NOD) model (Fig. 1e and Supplementary Fig. 2), suggesting that Arc neuron activation and its reversal by leptin represent a common feature of T1D. Interestingly, we noticed that fasting-induced c-Fos expression in the Arc was also significantly colocalized with LepR neurons (Fig. 1g, i and Supplementary Fig. 1), compared to control-fed conditions (Fig. 1f, i). Strikingly, leptin administration reduced c-Fos expression in the Arc (Fig. 1h, i), in a similar fashion to T1D. Given low leptin as a common feature of both fasting and T1D, these results suggest that LepR^{Arc} neuron activation is due to reduced leptin action. Since leptin action on reducing T1D hyperglycemia is known to be associated with restraining counter-regulatory hormone levels[10,12], we tested the effect of leptin i.c.v infusion on fasting responses. While glucose levels were not different between the fed ad libitum group and the saline treatment group with 8-h fasting (Fig. 1j), glucose levels in the leptin-treated group were rapidly reduced upon food removal, and reached to 2.5 mM (Fig. 1j), at which point the experiment was ended to avoid severe glucopenic complications. Interestingly, compared to the saline-treated control group, glucagon, a typical counter-regulatory hormone, was also reduced by leptin (Fig. 1k). Thus, T1D and fasting share a common mechanism in which heightened activation of LepR^{Arc}

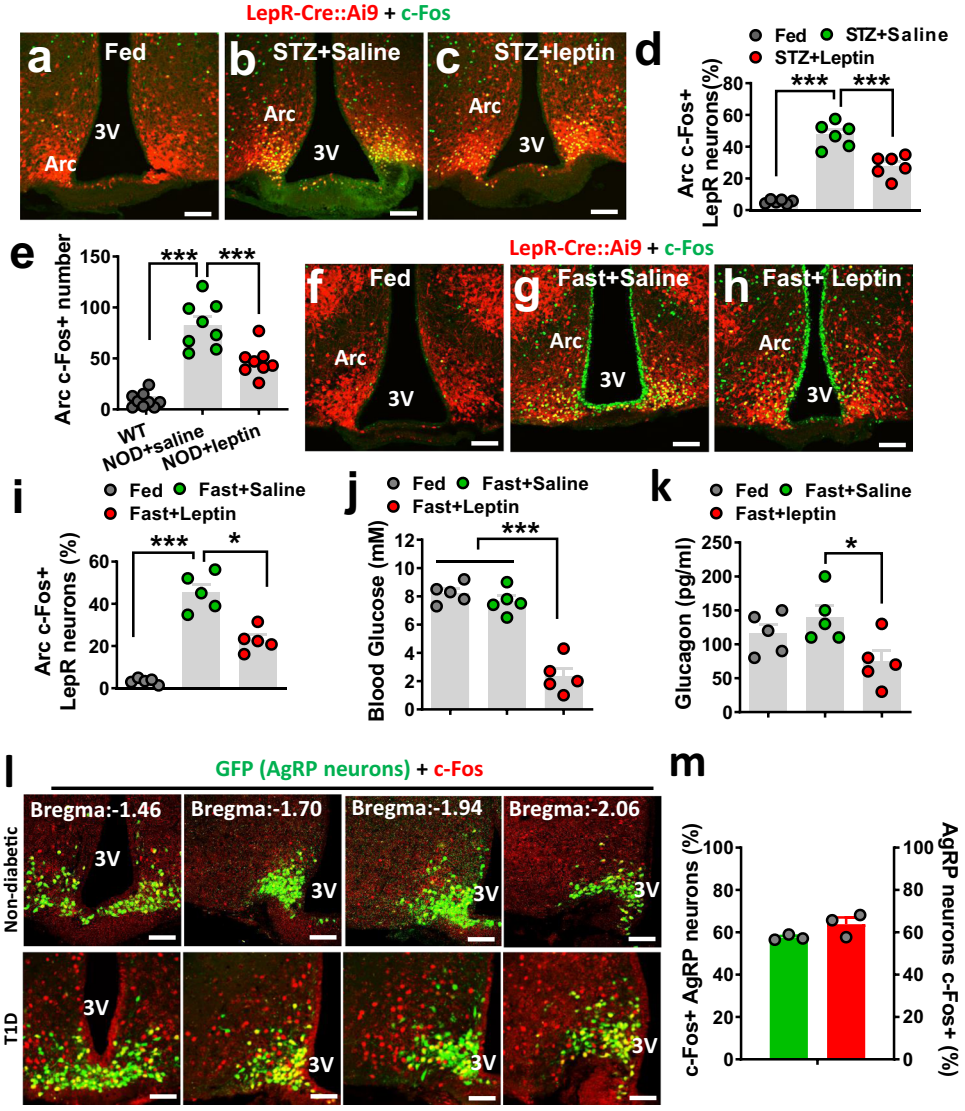
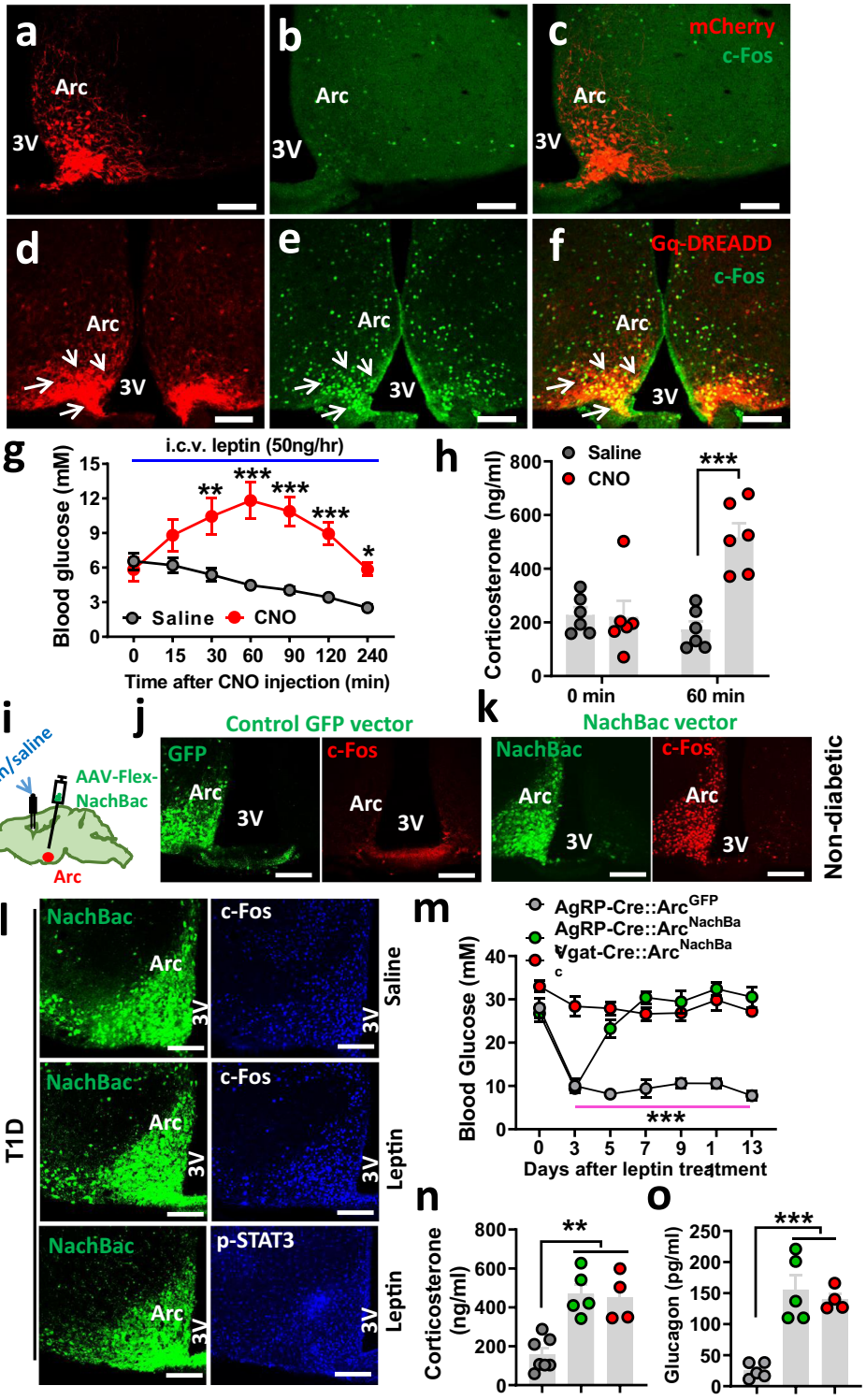


Fig. 1 Leptin suppresses counter-regulatory responses to fasting. a–i Leptin-Cre:Ai9 mice (8–10 weeks of age, males) were used as fed controls (**a**, **f**), made type 1 diabetic induced by STZ administration (**b**, **c**), subject to overnight fasting (**g**, **h**), or treated with i.c.v. leptin infusion (**c**, **h**). LepR neurons were shown by Ai9 reporter expression (red) and immunostaining was performed for c-Fos (green) (**a**–**c**, **f**–**h**). **d**–**i** Comparison in the percentage of LepR neurons with c-Fos expression among the indicated groups was shown in T1D mice (**d**, one-way ANOVA, $n = 6$/each, $F(2, 10) = 136.9$, $^{***}P < 0001$, control vs STZ-saline; $^{***}P = 0.004$, STZ-saline vs STZ-leptin) or controls (**i**, one-way ANOVA, $n = 5$/each, $F(2, 8) = 44.4$, $^{***}P < 0.0001$, fed vs fast-saline; $^{*}P = 0.0035$, fast-saline vs fast-leptin). **e** Comparison in the number of c-Fos neurons in the Arc in controls, saline, and leptin-treated nonobesity diabetic (NOD) mice (one-way ANOVA, $n = 9$ for WT and $n = 8$ for both NOD-saline and NOD-leptin, $F(2, 22) = 44.69$, $^{***}P < 0.0001$, WT vs NOD-saline; $^{***}P = 0.0006$, NOD-saline vs NOD-leptin). **j**, **k** In mice presented in panels **f**–**i**, comparisons were shown in glucose levels between fed and fasting, and between saline and leptin treatment conditions (**j**, one-way ANOVA, $n = 5$/each, $F(2, 8) = 116.6$, $^{***}P < 0.0001$, fed vs fast-leptin; $^{***}P < 0.0001$, fast-saline vs fast-leptin) and in glucagon levels between saline and leptin-treated groups (**k**, one-way ANOVA, $n = 5$/each, $F(2, 8) = 4.575$, $P = 0.1745$, fed vs fast-leptin; $^{*}P < 0.0427$, fast-saline vs fast-leptin). Blood glucose was measured between fed and 8-h fast (from early morning to late afternoon) and blood glucagon was measured at 8-h fasting. **l**, **m** In AgRP-Cre GFP-reporter mice, colocalization of c-Fos induction in STZ-T1D was shown in GFP-positive neurons in a series of sections from rostral to caudal Bregma levels (**l**) and percentage of c-Fos neurons that were colocalized in AgRP and percentage of AgRP neurons were c-Fos positive in T1D mice (**m**, $n = 3$/each). 3V the third ventricle, Arc arcuate nucleus, scale bar: 100 μM. All data presented as mean ± SEM.

neurons owing to reduced leptin action causes augmented counter-regulatory responses.

As AgRP neurons represent a subpopulation of Arc GABAergic ($GABA^{Arc}$) neurons[21,22] and have been a research focus on leptin action in T1D glucose, we also examined c-Fos expression patterns in these neurons in the STZ-T1D model. Using AgRP-Cre GFP-reporter mice to visualize AgRP neurons, we found that T1D-induced c-Fos expression was partly colocalized with AgRP neurons but also found in a large number of non-AgRP neurons (Fig. 1l, bottom panels), whereas a negligible number of c-Fos neurons was observed in control non-T1D mice (Fig. 1l, top panels). Roughly 50% of c-Fos neurons were found in AgRP neurons and >60% AgRP neurons were positive for c-Fos (Fig. 1m). These results suggest potential importance for both Arc AgRP and non-AgRP neurons in mediating the leptin action.

Leptin action on reducing T1D hyperglycemia is reversed by Arc neuron activation. Given the abundant T1D-induced c-Fos expression in the Arc, we tested the effect of direct Arc neuron



activation. We first examined whether acute activation of Arc LepR neurons reverses the leptin action. Toward this, we stereotaxically delivered control vectors (Fig. 2a) or AAV-Flex-hM3D(Gq)-mCherry vectors (Gq-DREADD) (Fig. 2d) bilaterally to the Arc of LepR-Cre mice. Selective viral targeting was verified by mCherry expression (Fig. 2a, d), and the function of Gq-DREADD was verified by CNO-induced c-Fos specifically in Arc LepR neurons (Fig. 2b, c, e, f). These mice were first made T1D and i.c.v.-treated with leptin, and then these glucose-normalized mice were divided in two groups, one treated with saline and the other with i.p. CNO. CNO effectively increased glucose compared to falling glucose levels in controls (Fig. 2g). This glucose-increasing effect lasted for nearly 4 h, within the range of duration in CNO-induced activation of DREADD receptors. CNO-induced glucose increase was accompanied by increased corticosterone (cort) levels (Fig. 2h), an opposite response to leptin treatment effects in T1D. To rule out a potential nonspecific effect of CNO in the observed glucose-increasing effects, we generated a new group of STZ-T1D mice with glucose normalized by i.c.v. leptin treatment (Supplementary Fig. 3a), and found that CNO injections had no effect on the glucose level in these mice (Supplementary Fig. 3b). Thus, acute activation of Arc LepR neurons is

Fig. 2 Activation of Arc neurons reverses leptin action on reducing T1D hyperglycemia. a–f DREADD-mediated acute activation of Arc LepR neurons reverses the leptin action. LepR-Cre mice were injected with AAV-Flex-mCherry control vectors (**a**–**c**) and AAV-DIO-h3MD(Gq)-mCherry (**d**–**f**) to bilateral Arc, and expression of mCherry (**a**, **d**) and CNO-induced c-Fos (**b**, **e**) were confirmed in the Arc. Representative pictures of 6 repeats as shown in **g** and **h**. **g**, **h** Effects on glucose with single i.p. injection of CNO in T1D LepR-Cre mice with Gq-DREADD delivery to bilateral Arc and euglycemia restoration via i.c.v. leptin infusion (**g**, two-way ANOVA, $n = 6$/each, $F(1, 70) = 79.47$, $^{***}P < 0.0001$ (at the 60-min time point); $^{**}P = 0.0001$ (at the 120-min time point), and comparison in glucagon levels between saline and leptin-treated groups (**h**, two-way ANOVA, $n = 6$/each, $F(1, 20) = 13.97$, $^{***}P < 0.0001$, saline vs CNO at the 90-min time point). **i–n** Effects of NachBac-mediated chronic activation of Arc neurons on the leptin action. **i** Diagram showing injections of NachBac/or control GFP vectors in AgRP or GABA^{Arc} neurons through the delivery of respective vectors to the Arc of AgRP or Vgat-Cre mice, and expression of GFP (green) and c-Fos (red) with one side of the Arc receiving vector injections for control GFP vectors (**j**) and NachBac vectors (**k**). **l** In Vgat-Cre mice that were made T1D and received NachBac vector injections to bilateral Arc with i.c.v. pumps infusing saline or leptin as indicated, representative NachBac expression (GFP, left panels), and c-Fos/p-STAT3 (blue, right panels) are shown. Pictures in (**j–l**) are representative of three repeats. **m** Effects on glucose levels in response to i.c.v. infusion of leptin in the indicated groups of mice (two-way ANOVA, $n = 6$ for AgRP-GFP or AgRP-NachBac, and $n = 4$ for Vgat-NachBac, $F(2, 91) = 190.6$, $P = 0.9647$, AgRP-GFP vs AgRP-NachBac at day 3; $^{***}P < 0.0001$, AgRP-GFP vs Vgat-Nachbac at day 3). **n**, **o** Measurements and comparison of cort (**n**, one-way ANOVA, $n = 7$ for AgRP-GFP, $n = 5$ for AgRP-NachBac and $n = 4$ for Vgat-NachBac, $F(2, 13) = 16.52$, $^{**}P = 0.006$, AgRP-GFP vs AgRP-NachBac; $^{**}P = 0.0017$, AgRP-GFP vs Vgat-NachBac) and glucagon (**o**, one-way ANOVA, $n = 5$ for AgRP-GFP and AgRP-NachBac, and $n = 4$ for Vgat-NachBac, $F(2, 11) = 21.89$, $^{***}P = 0.0002$, AgRP-GFP vs AgRP-NachBac; $^{***}P = 0.001$, AgRP-GFP vs Vgat-NachBac) levels in the blood at day 13 of i.c.v. leptin infusion shown in panel **m**. 3V the third ventricle, Arc arcuate nucleus, scale bar: 100 μM. All data presented as mean ± SEM.

sufficient to cause a transient blocking effect on leptin in reducing glucose and counter-regulatory responses.

We next examined the effect of chronic activation of Arc neurons on leptin action. Toward this, we bilaterally delivered an AAV-EF1a-Flex-EGFP-P2A-mNachBac vector to the Arc (Fig. 2i). The vector conditionally expresses, in a Cre-dependent manner, a type of sodium channel from bacteria (NachBac) that has a low membrane threshold for action potential firing and slow inactivation kinetics, and has been used to effectively elevate neuron activity without a need of ligand administration[32–34]. Given the technical difficulty in achieving specific targeting Arc LepR neurons with stereotaxic delivery to the Arc of LepR-Cre mice owing to abundant Cre expression in the nearby regions including VMH, we switched to Vgat-Cre mice, which have been used previously to specifically target Arc neurons and avoid surrounding glutamatergic neurons[32]. As leptin action on T1D glucose is known to be mediated by GABAergic neurons[6], using Vgat-Cre will be able to capture Arc neurons that mediate the leptin action. Delivery of NachBac vectors to one side of the Arc of Vgat-Cre mice led to the abundant expression of c-Fos in the injected side compared to the noninjected side (Fig. 2k), where no differences were observed in mice with control GFP vector injections (Fig. 2j), confirming that NachBac expression led to increased neuron activity levels. We then generated STZ-induced T1D in AgRP-Cre or Vgat-Cre mice. After establishing stable T1D hyperglycemia, we delivered NachBac or control vectors bilaterally to the Arc of these mice, and at the same time implanted osmotic minipumps (2-week duration) for i.c.v. infusion of leptin or saline. In contrast to severe obesity demonstrated previously[32], NachBac expression in Arc AgRP or Vgat neurons in T1D mice failed to cause body weight changes, which is likely due to already-elevated neuron activity of these neurons in the T1D condition. Consistent with the aforementioned data, in control mice with GFP vector expression, leptin treatment effectively reduced c-Fos induction in the Arc of T1D, which was associated with increased p-STAT3 expression (Supplementary Fig. 4). In contrast, leptin failed to reduce c-Fos in NachBac-expressing GABA^{Arc} neurons (Fig. 2l, middle panels), compared to the saline treatment group (Fig. 2j, top panels). We validated that failure to reduce c-Fos expression was not due to failed delivery of leptin, given that we observed abundant p-STAT3 induction in the Arc (Fig. 2j, bottom rows). Similar results were also observed in NachBac-expressing AgRP neurons (Supplementary Fig. 5). Strikingly, i.c.v. leptin infusion failed to reduce T1D hyperglycemia in NachBac-injected Vgat-Cre mice, while it maintained its normal effects in reducing glucose in GFP-injected Vgat-Cre mice (Fig. 2m). Interestingly, in NachBac-injected AgRP mice, leptin initially reduced glucose to a normal level, which was reversed around day 5 during the leptin treatment (Fig. 2m). The delayed reversal of the leptin action may reflect a delay in NachBac expression in a small number of Arc neurons (i.e., AgRP neurons) and rapid pharmacological action of leptin. Consistently, leptin infusion failed to reduce blood cort levels in the groups with failed reduction of T1D hyperglycemia (Fig. 2n). The changes in glucose were not caused by changes in body weight as there was no body weight difference among mouse groups (Supplementary Fig.6a). Consistent with the reversal of T1D-reduced glucose, the control group exhibited a significant reduction in feeding (Supplementary Fig. 6b). Together, these results demonstrate that leptin action on reducing T1D hyperglycemia is mediated through inhibition of GABA^{Arc} neurons, and that aberrant activation of Arc neurons, including AgRP neurons, contributes significantly to both pathogenesis of T1D hyperglycemia and leptin action on reversal of T1D hyperglycemia.

Acute inhibition of Arc neurons on T1D hyperglycemia. Given the aforementioned data that when leptin failed to reduce c-Fos in the Arc it failed to reduce T1D hyperglycemia, we examined whether inhibition of Arc neurons caused a leptin-mimicking effect on reducing T1D hyperglycemia. For this, we delivered AAV-Flex-h4MGi-mCherry (Gi-DREADD) bilaterally to the Arc of AgRP-Cre or Vgat-Cre mice. To verify the effects of Gi-DREADD, we generated STZ-induced T1D in these mice. Abundant c-Fos expression was found in the Arc of control STZ-T1D mice (Fig. 3a). Consistent with differences in the number of AgRP and GABA^{Arc} neurons, in CNO-injected AgRP-Cre mice, there was no obvious colocalization between c-Fos and AgRP neurons (Fig. 3b) and CNO reduced the majority of c-Fos expression in T1D Vgat-Cre mice (Fig. 3c), suggesting an effective action of CNO-induced neuron inhibition. Interestingly, a 3-day injection protocol of CNO effectively reduced T1D hyperglycemia in Vgat-Cre mice, but had no effects on either AgRP-Cre mice or "missed-targeted" mice (Fig. 3d). Notably, the reduction in glucose was transient, and the glucose levels gradually went up to control levels at day 3 after the CNO treatment protocol. No difference in body weight (Supplementary Fig. 6c) or feeding (Supplementary Fig. 6d) was observed in these mice. The

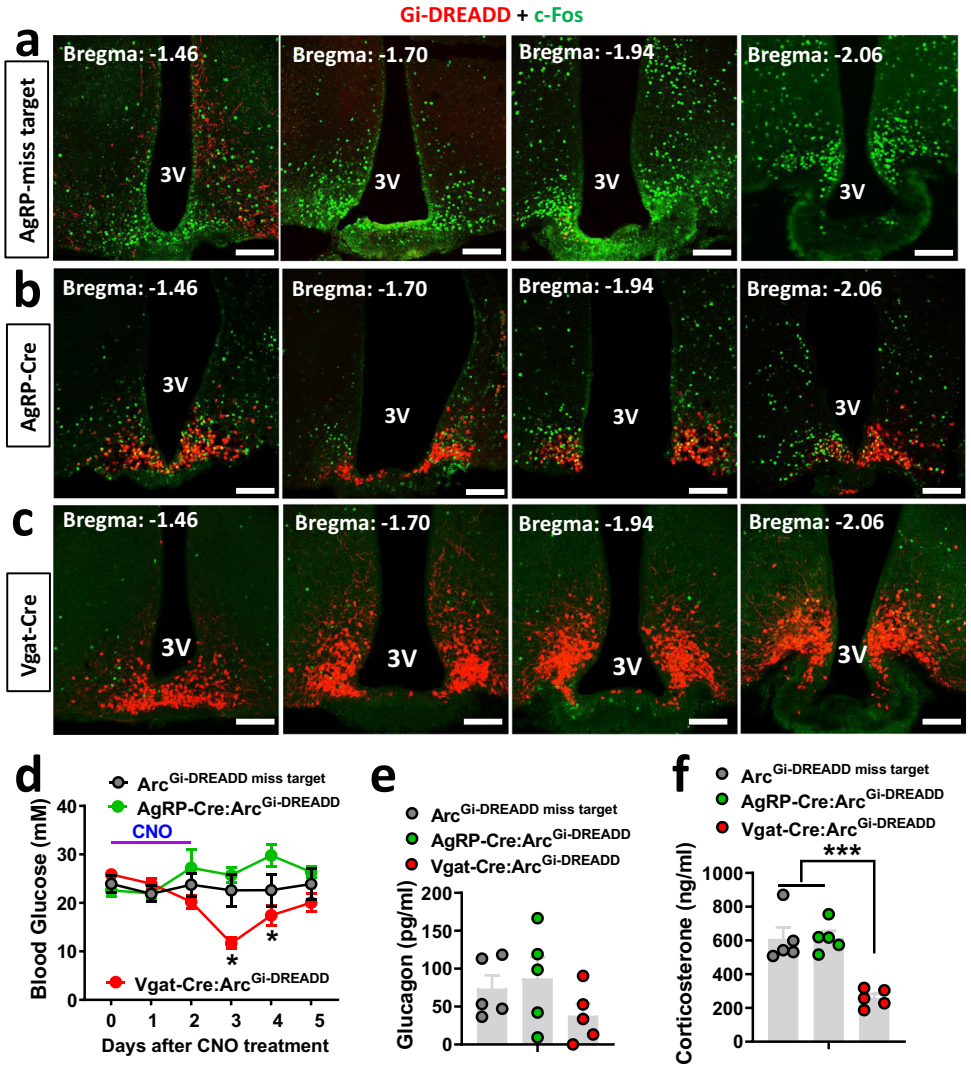


Fig. 3 Acute inhibition of Arc neurons on T1D glucose. AgRP-Cre or Vgat-Cre mice were injected with AAV-DIO-h4MD(Gi)-mCherry vectors to bilateral Arc and then were made STZ-T1D. **a**–**c** Series of sections spanning the Arc showing specific expression of viral vector expression (red) and c-Fos expression (green) in mistargeted mice (**a**), AgRP-Cre (**b**), and Vgat-Cre mice (**c**). Representative pictures over 3 repeats. **d**–**f** Comparisons in blood glucose in the indicated groups of mice in response to a 3-day CNO treatment protocol (twice daily for 3 days) (**d**, two-way ANOVA, $n = 5$/each, $F(2, 75) = 16.41$, $^{*}P < 0.0001$, AgRP-Gi-DREADD vs Vgat-Cre-Gi-DREADD at day 3; $^{*}P < 0.0001$, missed vs Vgat-Cre-Gi-DREADD at day 3), comparisons in corticosterone (**e**, one-way ANOVA, $n = 5$/each, $F(2, 12) = 1.449$, $P = 0.4774$, missed vs Vgat-Cre-Gi-DREADD at day 3) and glucagon (**f**, one-way ANOVA, $n = 5$/each, $F(2, 12) = 18.93$, $^{***}P = 0.0005$, Vgat-Gi-DREADD vs missed; $^{***}P = 0.0005$, Vgat-Gi-DREADD vs AgRP-Gi-DREADD) at day 3 after the initiation of CNO treatment. 3V the third ventricle, Arc arcuate nucleus. All data presented as mean ± SEM. Scale bar: 100 μM.

reduction in glucose was associated with reduced corts (Fig. 3d) and a trend in reduced glucagon levels (Fig. 3e). Thus, acute inhibition of Arc GABA + neurons, but not AgRP neurons, is sufficient to cause a transient reduction in both T1D glucose and counter-regulatory responses.

Chronic inhibition of Arc neurons on T1D hyperglycemia. Brain leptin infusion effectively reduces T1D hyperglycemia during the whole period of leptin infusion, while acute inhibition through CNO-Gi-DREADD only produced a transient reduction in T1D glucose, suggesting chronic inhibition of Arc neurons is required to achieve long-term remission on T1D glucose. To specifically examine this, we used conditional AAV-DIO-Kir2.1-P2A-dTomato (DIO-Kir2.1) vectors expressing a mutated form of the Kir2.1 channel, which is known to effectively reduce neuron activity and excitability[32–34]. To verify Kir2.1 expression and function, we first delivered the virus to one side of the Arc (Fig. 4a, left panels) of AgRP-Cre (top panels) or Vgat-Cre mice (bottom panels). In T1D, as expected, the noninjected side exhibited abundant c-Fos, while the injected side showed significantly reduced levels of c-Fos expression (Fig. 4a, middle and right panels). These results suggest that Kir2.1 expression leads to chronic neuron inhibition.

Using STZ-T1D AgRP-Cre or Vgat-Cre mice, we bilaterally delivered either the Kir2.1 or control mCherry viruses to the Arc, and monitored weekly glucose levels following viral injection. While control groups exhibited persistent T1D hyperglycemia, Kir2.1 expression in $GABA^{Arc}$ neurons effectively reduced T1D to a normal level and this effect remained during the whole 8-week monitoring period (Fig. 4b). Interestingly, Kir2.1 expression in AgRP neurons caused an intermediate effect (Fig. 4b). Consistent with the glucose effect, feeding was reduced in both groups of mice (Fig. 4c), but body weight showed no obvious

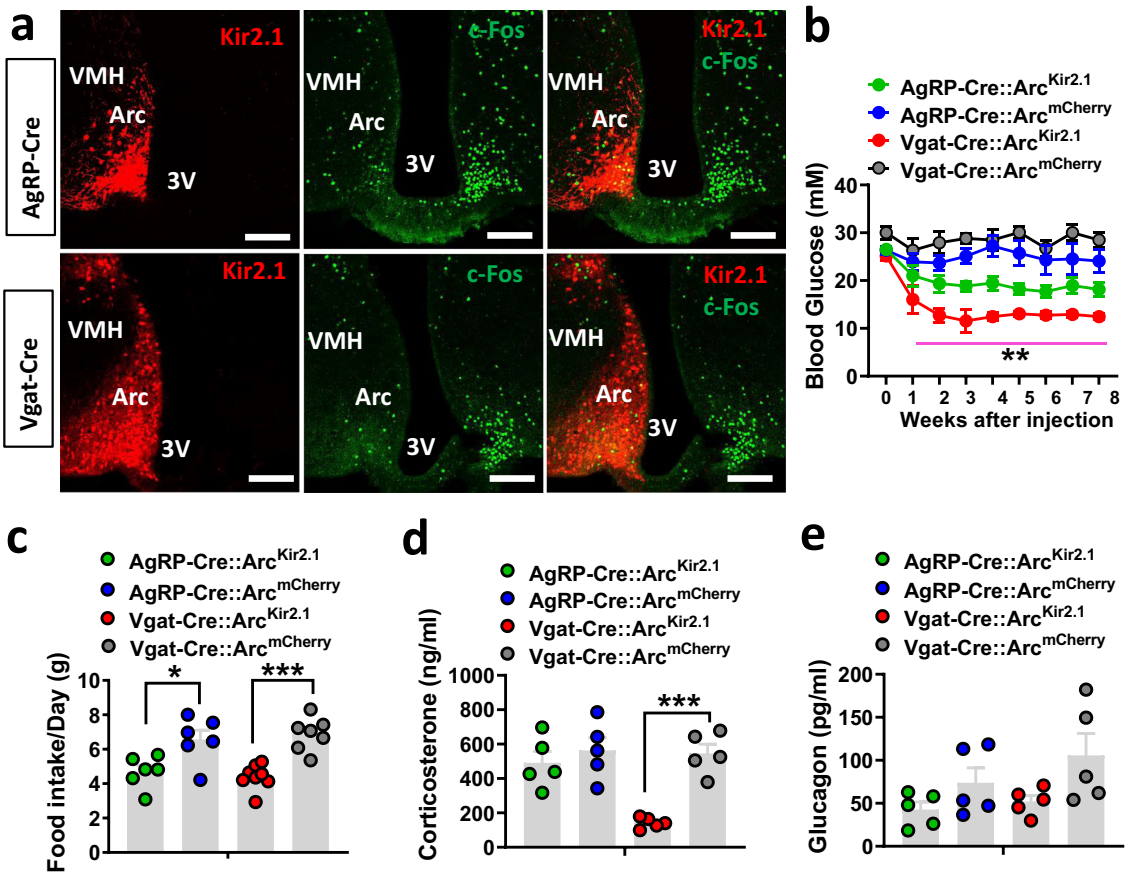


Fig. 4 Chronic inhibition of Arc neurons on T1D glucose. AgRP-Cre or Vgat-Cre mice (8–10 week-old males) were first made STZ-T1D and then injected with AAV-DIO-Kir2.1-P2A-dTomato vectors or control AAV-Flex-mCherry to bilateral Arc. **a** Representative sections showing comparison in the expression of Kir2.1 (red) and c-Fos (green) in the Arc of AgRP-Cre mice (top) and Vgat-Cre (bottom), in which the Kir2.1 vector was delivered to one side of the Arc. Representative pictures from $n = 2$ mice. **b**–**e** Weekly glucose levels following injections of the viral vectors (**b**, two-way ANOVA, $n = 6$ for AgRP-mCherry, AgRP-Kir2.1, or Vgat-mCherry, and $n = 7$ for Vgat-Kir2.1, $F(3, 189) = 120.1$, $P = 0.0641$, AgRP-mCherry vs AgRP-Kir2.1; $^{**}P < 0.0001$, Vgat-mCherry vs Vgat-Kir2.1), food intake during week 3–4 after viral delivery (**c**, two-way ANOVA, $n = 6$ for both AgRP-mCherry and AgRP-Kir2.1, $n = 9$ for Vgat-mCherry, and $n = 8$ for Vgat-Kir2.1, $F(3, 23) = 11.68$, $^{*}P = 0.0149$, AgRP-mCherry vs AgRP-Kir2.1; $^{***}P = 0.0003$, Vgat-mCherry vs Vgat-Kir2.1) and blood levels of corticosterone (**d**, two-way ANOVA, $n = 5$/each, $F(3, 16) = 12.16$, $P = 0.8091$, AgRP-mCherry vs AgRP-Kir2.1; $^{***}P = 0.0006$, Vgat-mCherry vs Vgat-Kir2.1) and glucagon (**e**, two-way ANOVA, $n = 5$/each, $F(3,6) = 2.904$, $P = 0.06$, Vgat-mCherry vs Vgat-Gi-DREADD at week 8 after viral injection. 3V the third ventricle, Arc arcuate nucleus. All data presented as mean ± SEM. Scale bar: 100 μM.

changes (Supplementary Fig. 6e). Cort levels were suppressed by Kir2.1 expression in Vgat-Cre mice but not in AgRP mice (Fig. 4d), while both groups exhibited a trend of reduced glucagon levels (Fig. 4e). These results demonstrate that Kir2.1 expression in GABA^{Arc}, but not AgRP neurons, is sufficient to restore T1D hyperglycemia, mimicking brain leptin action on T1D glucose. Together, these results reveal an important role for both Arc AgRP and non-AgRP neurons in mediating the leptin action.

AgRP neurons are not required for T1D hyperglycemia or for leptin action on reducing T1D glucose. To directly examine the role of Arc non-AgRP neurons in T1D hyperglycemia, we bred Vgat-Cre with the previously established strain AgRP^{DTR} mice, which can be used to lesion AgRP neurons with diphtheria toxin (DTX) administration[35]. In Vgat-Cre::AgRP^{DTR} mice, DTX treatment at P3 effectively killed AgRP neurons (Fig. 5a). These mice were then treated with STZ at 7–8 weeks of age, and monitored for changes in blood glucose. Interestingly, blood glucose levels were not different between DTX and control groups, both of which exhibited typical glucose levels in T1D (Fig. 5b), suggesting that the presence of AgRP neurons is not required for the development of T1D hyperglycemia. The DTX-treated T1D mice were then divided into two groups, one treated with saline and the other with i.c.v. leptin infusion. While saline had no effects on T1D hyperglycemia, leptin effectively reduced T1D hyperglycemia to normal levels (Fig. 5c), suggesting that the presence of AgRP neurons is not required for leptin action on reducing T1D glucose. Further measurements showed that i.c.v. leptin indeed reduced c-Fos expression (Fig. 5d), glucagon, (Fig. 5e), and cort (Fig. 5f) associated with T1D development, consistent with brain leptin effects. No changes in body weight (Supplementary Fig. 6f) but reduced feeding were observed in the leptin-treated group (Supplementary Fig. 6g), consistent with the leptin-mediated restoration of euglycemia.

Loss of LepR^{Arc} neurons in nutrient sensing in STZ-T1D and reversal by leptin. LepR^{Arc} neurons become activated upon fasting when glucose is low, suggesting they are glucose-inhibited neurons. However, these neurons in T1D, an uncontrolled hyperglycemic condition, were also activated, suggesting that LepR^{Arc} neurons in T1D may be defective in nutrient sensing. To test this, we examined c-Fos expression in LepR^{Arc} neurons in both control and T1D mice. Compared to fed conditions (Fig. 6a), LepR^{Arc} neurons responded with dramatic c-Fos

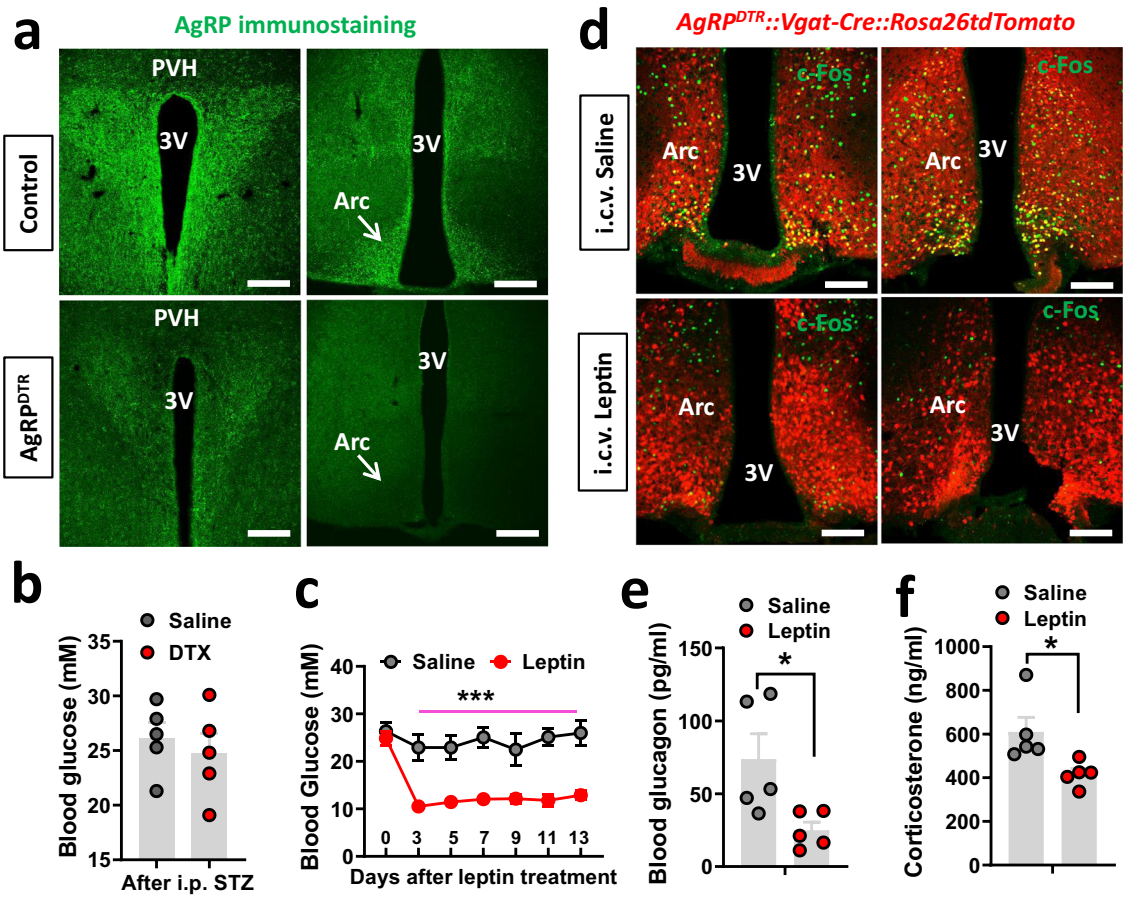
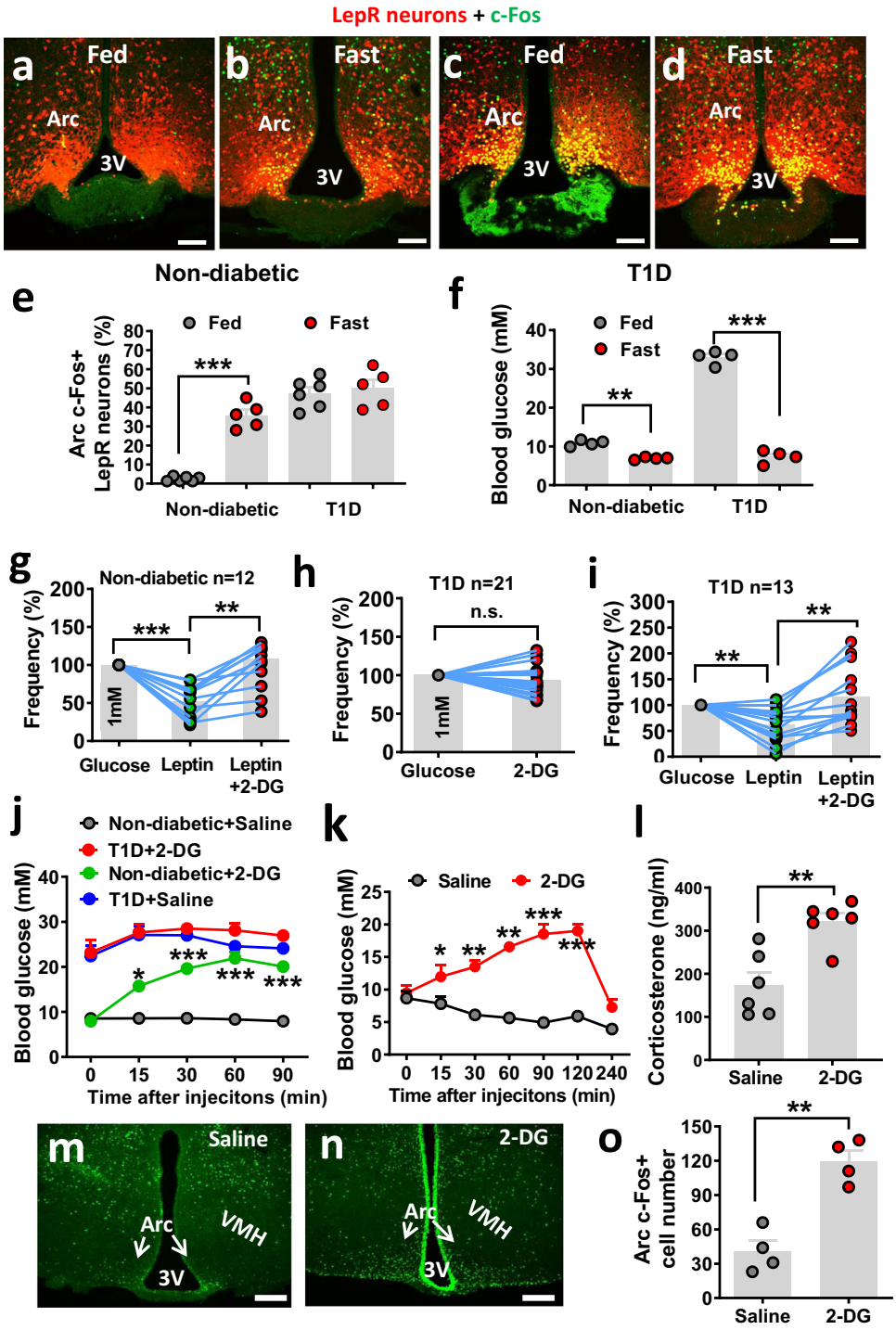


Fig. 5 AgRP neurons are not required for T1D hyperglycemia development and for leptin action in reducing T1D glucose. Vgat-Cre::Ai9::AgRP^{DTR} mice were treated with DTX/saline at P3, made STZ-T1D at 8–9-weeks old, and then implanted with i.c.v. minipump for a 2-week leptin infusion. **a** Representative pictures from $n = 3$ mice showing immunostaining for AgRP in the Arc (right panels) and PVH (left panels) of both saline-treated controls (top) and the DTX-treated group (bottom). **b** Comparisons in blood glucose between saline and DTX-treated groups after STZ treatment (two-tailed unpaired Student's t tests, $n = 5$/each, $t = 0.6019$, df = 8, $P = 0.5639$). **c** Reponses in glucose levels in DTX-treated Vgat-Cre::Ai9::AgRP^{DTR} mice that received i.c.v. treatment of saline or leptin during the 14-day leptin treatment period (two-way ANOVA, $n = 5$/each, $F(1, 56) = 150.4$, $^{***}P < 0.0001$, saline vs leptin at day 13). **d** Representative sections from $n = 2$ mice showing expression of c-Fos (green) in Arc GABA + neurons (red) in i.c.v. saline-treated (left panel) and leptin-treated mice (right panel). **e**, **f** Comparisons in glucagon (**e**, two-tailed unpaired Student's t tests, $n = 5$/each, $^{*}P = 0.0266$) and corticosterone (**f**, two-tailed unpaired Student's t tests, $n = 5$/each, $^{*}P = 0.027$) at day 13 with i.c.v. leptin treatment. 3V the third ventricle, Arc arcuate nucleus. All data presented as mean ± SEM. Scale bar: 100 μM.

induction in response to fasting (Fig. 6b, e). Similar to the aforementioned results, these same neurons in T1D showed abundant c-Fos expression even fed ad libitum (Fig. 6c), and fasting failed to further increase c-Fos expression (Fig. 6d, e). As expected, blood glucose levels in the control group were significantly reduced in fasting (8.1 mM) compared to fed conditions (10.0 mM). Strikingly, glucose levels in T1D mice showed a much greater reduction (30.2–8.2 mM) in T1D mice (Fig. 6f). Thus, in T1D mice, the dramatic reduction in glucose levels (>20 mM) in response to fasting failed to initiate a significant change in c-Fos expression, which is in contrast to a dramatic increase in c-Fos expression in control mice, even with a small reduction in glucose (<2 mM). These contrasting results suggest that LepR^{Arc} neurons lose the ability in nutrient sensing in vivo. To directly test this, we monitored the activity of LepR^{Arc} neurons through electrophysiological recordings. For this, we primarily focused on neurons with observable changes in neuronal firing in response to altered levels of glucose and/or leptin (Supplementary Fig. 7a). With recordings from 89 Arc LepR neurons, we noted a clear effect in firing with changes in glucose and leptin (Supplementary Fig. 7b). Among them, most of them were inhibited by leptin or glucose, and ~67% of these neurons were inhibited by both leptin and glucose (Supplementary Fig. 7b). Given our data described above on potential effects of leptin and glucose inhibition on Arc neurons in T1D glucose levels, we next chose to focus on those neurons that were inhibited by glucose or leptin.

To explore the mechanism of leptin action on nutrient sensing, we tested the response of LepR^{Arc} neurons to 2-deoxy glucose (2-DG), a glucopenic agent that causes nutrient deprivation. The leptin inhibitory action on LepR^{Arc} neurons was reversed by 2-DG (Fig. 6g), suggesting that the leptin inhibition requires nutrient supply. Interestingly, LepR^{Arc} neurons in T1D were not sensitive to 2-DG (Fig. 6h), consistent with the notion that these neurons lose nutrient sensing. In contrast, in the presence of leptin, LepR^{Arc} neurons in T1D gained inhibitory responses to increased glucose and leptin inhibition was also reversed by 2-DG (Fig. 6i), suggesting that the effect of nutrients, e.g., glucose and 2-DG, requires the presence of leptin. These results suggest that the mechanism underlying leptin action lies in facilitating nutrient sensing of LepR neurons.

To further examine the physiology associated with the reversal effect of 2-DG on leptin inhibitory action, we tested the effect of 2-DG on glucose in both control and STZ-induced T1D mice. As



expected, i.p. 2-DG induced a significant increase in glucose levels in controls (Fig. 6j). However, it failed to further increase glucose levels in T1D mice (Fig. 6j). However, it could not be ruled out that the failure in increasing glucose levels might be due to a ceiling effect. To further address this and specifically examine the effect of 2-DG in the brain, we tested the effect of i.c.v injection of 2-DG on leptin's ability to reduce T1D hyperglycemia. We first generated STZ-induced T1D with glucose normalization by i.c.v. infusion of leptin as described previously[7]. These mice were then randomly divided into two groups, one injected with i.c.v. saline and the other with i.c.v. 2-DG. Both groups had food removed during the testing. While the saline-injected group gradually reduced glucose levels, i.c.v. 2-DG induced a rapid increase in glucose levels (Fig. 6k), suggesting that 2-DG potently reversed the leptin action on reducing T1D hyperglycemia. The rapid increase in glucose levels was followed by a gradual drop to baseline levels at 4 h after 2-DG injection (Fig. 6k), which is consistent with a typical duration of hyperglycemia responses normally induced by 2-DG, and confirms that the rapid increase in glucose levels is not due to loss of leptin action. Interestingly, the increase in glucose levels was associated with higher corticosterone levels (Fig. 6l), suggesting that the reversal of glucose was mediated by the reversal of counter-regulatory hormone levels. Moreover, while Arc neurons in saline-treated mice showed negligible c-Fos expression (Fig. 6m, o), those in 2-DG-treated mice showed significantly more c-Fos (Fig. 6n, o).

Fig. 6 LepR^{Arc} neurons in T1D lose nutrient sensing and restoration by leptin. a–d LepR-Cre::Ai9 reporter mice (8–10 weeks of age, males) were used either as controls (**a**, **b**) or made STZ-T1D (**c**, **d**), and were used either at fed (**a** and **c**) or overnight fasting conditions (**b**, **d**). Representative pictures from $n = 5$–6 mice showing in **e** in **a**–**d** showing that c-Fos immunostaining was performed and colocalized with LepR neurons. **e**, **f** Comparison in the percentage of LepR^{Arc} neurons that are c-Fos positive (**e**, two-way ANOVA, $n = 6$ for non-diabetic fed and T1D fast, and $n = 5$ for non-diabetic fed and T1D fast, $F(1, 12) = 36.21$, $^{***}P < 0.0001$, non-diabetic fed vs fast; $P = 0.7375$, T1D fed vs fast)) and blood glucose levels (**f**, two-way ANOVA, $n = 5$/each, $F(1. 13) = 526.1$, $^{**}P = 0.002$, non-diabetic fed vs fast; $^{***}P < 0.0001$, T1D fed vs fast) between fed and fasting or between controls and STZ groups. 3 the third ventricle, Arc: arcuate nucleus. Scale bar: 100 μM. **g–i** Electrophysiological recording was performed on LepR^{Arc} neurons on brain sections from LepR-Cre reporter mice (8–10 weeks of age, males), which were used as controls (**g**, one-way ANOVA, $F(11, 22) = 1.101$, $n = 13$/each, $^{***}P < 0.0001$, glucose vs leptin; $^{**}P = 0.0079$, leptin vs leptin/2-DG) or made T1D (**h**, two-tailed unpaired Student's t tests, $n = 21$/each, $t = 0.1622$, df = 40, $P = 0.1126$, and **i**, one-way ANOVA, $n = 14$/each, $F(12, 24) = 2.285$, $^{**}P = 0.0026$, glucose vs leptin; $^{**}P = 0.0011$, leptin vs leptin/2-DG) and LepR^{Arc} neurons were recorded for firing frequency in response to leptin and/or 2-DG. Data were expressed relative to baseline firing rates for each recorded neuron. **j** Comparison in glucose levels in nondiabetic controls and T1D mice treated with i.p. injection of either saline or 2-DG during a period of 90 min after the injection (two-way ANOVA, $n = 6$/each, $F(3, 50) = 159.2$, $^{***}P < 0.0001$, non-diabetes—saline vs non-diabetes-2-DG, $P = 0.4716$, T1D-saline vs T1D-2-DG). **k–o** Groups of wild-type mice (8–10 weeks of age, males) were first made T1D and were then implanted with both i.c.v. minipump for leptin infusion and i.c.v. cannulas for brain injection of 2-DG or saline. Brain injections of 2-DG or saline were performed after leptin-mediated euglycemia restoration. Blood glucose was measured following i.c.v. injection of 2-DG at the indicated time points (**k**, two-way ANOVA, $n = 6$/each, $F(1, 35) = 240.1$, $^{***}P < 0.0001$, saline vs 2-DG at the 120-min time point) and corticosterone levels were measured at 90 min after 2-DG injections (**l**, two-tailed unpaired Student's t tests, $t = 4.108$, df = 10; $n = 6$/each, $^{**}P = 0.0021$). Brain sections were used for c-Fos immunostaining from i.c.v. saline (**m**) and 2-DG treatments (**n**) at 90 min after i.c.v. 2-DG injection, and neuron number with c-Fos expression was compared between these two groups (**o**, two-tailed unpaired Student's t tests, $t = 5.885$, df = 6, $n = 4$/each, $^{**}P = 0.0011$). Data presented as mean ± SEM. 3V the third ventricle, Arc arcuate nucleus, VMH ventromedial hypothalamus. Scale bar: 100 μM.

Taken together, these results suggest that leptin inhibition of Arc LepR neurons in T1D is mediated by replenishing the nutrient supply, which is reversed by 2-DG.

Leptin action on LepR^{Arc} neurons in reducing T1D hyperglycemia involves the AMPK pathway. AMP kinase (AMPK) is known to be a key energy sensor in neurons[36]. To test a potential involvement of AMPK in leptin-mediated glucose nutrient sensing in LepR^{Arc} neurons, we performed immunohistochemistry for phospho-AMPK (p-AMPK), the activated form of AMPK that is known to be increased during energy deprivation. Compared to controls (Fig. 7a), LepR^{Arc} neurons in T1D exhibited a dramatic increase of p-AMPK (Fig. 7a, b). Notably, p-AMPK expression in T1D was mostly colocalized with LepR neurons. Leptin treatment significantly reduced p-AMPK in LepR neurons (Fig. 7a, b), which was reversed by 2-DG (Fig. 7a, b) indicating a specific role for leptin action in facilitating nutrients to these neurons. Interestingly, p-AMPK and c-Fos were highly colocalized in the Arc (Fig. 7c), suggesting that activation of Arc LepR neurons is due to nutrient deprivation. To examine the role of AMPK activation in T1D hyperglycemia, we treated STZ-induced T1D mice, in which glucose levels were normalized by i.c.v. leptin infusion, with saline or AICAR, a specific agonist of AMPK. While glucose in the saline group gradually reduced during the testing period, AICAR effectively reversed the leptin action and increased glucose levels (Fig. 7d), which was associated with increased glucagon levels (Fig. 7e), consistent with a reversal of suppressing effects on counter-regulatory hormones by leptin action in reducing T1D hyperglycemia. These results suggest that leptin action on Arc LepR neuron activity involves the AMPK pathway, further confirming that leptin action on T1D glucose is mediated through suppressing the activation of LepR neurons owing to energy deprivation.

Discussion

Insulin deficiency is the cause of T1D; however, accumulating evidence suggests an involvement of brain dysfunction in T1D pathogenesis, as demonstrated by central leptin action on euglycemia restoration independent of insulin action[3]. T1D models exhibit a severe reduction of leptin levels, suggesting a physiologic contribution of leptin loss toward uncontrolled hyperglycemia in T1D. Despite much interest in the brain mechanisms underlying the leptin action, the brain location and the nature of the defects remain largely elusive. Based on combined mouse genetics, selective brain targeting and pharmacology, electrophysiological recordings, and the investigation of STZ-induced T1D models, our studies collectively reveal the following important insights: (1) GABAergic LepR^{Arc} neurons mediate leptin action on reducing T1D hyperglycemia, (2) Arc GABAergic non-AgRP neurons play a critical role in mediating the leptin action, (3) the presence of AgRP neurons is not required for either T1D development or for leptin action on reducing T1D hyperglycemia, (4) LepR^{Arc} neurons in T1D are in an activated state owing to energy deprivation, and (5) leptin action is mediated by inhibiting the activated LepR^{Arc} neurons in T1D through reversing energy deprivation (Fig. 7f).

This study mainly uses a T1D rodent model induced by STZ to examine the insulin-independent effect of leptin. It is important to note that the term of T1D referred here is specifically for the state of untreated insulinopenic diabetes induced by STZ, which is distinct from the typical type 1 diabetes in humans that receive insulin treatments with largely controlled glucose levels. Our results demonstrate that GABAergic LepR^{Arc} neurons mediate T1D hyperglycemia and leptin action on reducing T1D glucose. Among various LepR neurons in the brain, only LepR^{Arc} neurons were selectively activated in T1D. The physiological importance of this activation is reflected from the striking effects on T1D glucose by direct manipulation of Arc neuron activity. Both acute and chronic activation of GABA^{Arc} neurons reversed leptin action on reducing T1D, while inhibition of these neurons was sufficient to produce leptin-mimicking action on reducing T1D hyperglycemia. Due to technical limitations in using LepR-Cre to target LepR^{Arc} neurons, which caused varied offsite targeting to nearby glutamatergic neurons in the ventromedial hypothalamus (VMH), we instead used Vgat-Cre to selectively target GABA^{Arc} neurons. Since the function of LepR is mediated by GABAergic neurons in both body weight[21] and T1D glucose[6], it is most likely that GABAergic LepR^{Arc} neurons mediate the effects we observed in our study. The revealed importance of GABAergic LepR^{Arc} is consistent with previous observations on the noninvolvement of VMH LepR neurons in mediating leptin action on T1D glucose[15]. Thus, heightened activation of GABAergic LepR^{Arc} represents one major pathogenic cause of T1D hyperglycemia. Therefore, strategies aiming to inhibit these neurons should represent an effective therapy to achieve leptin-mimicking euglycemia restoration in T1D.

Our results revealed previously unappreciated importance of non-AgRP Arc neurons in T1D pathogenesis and mediating

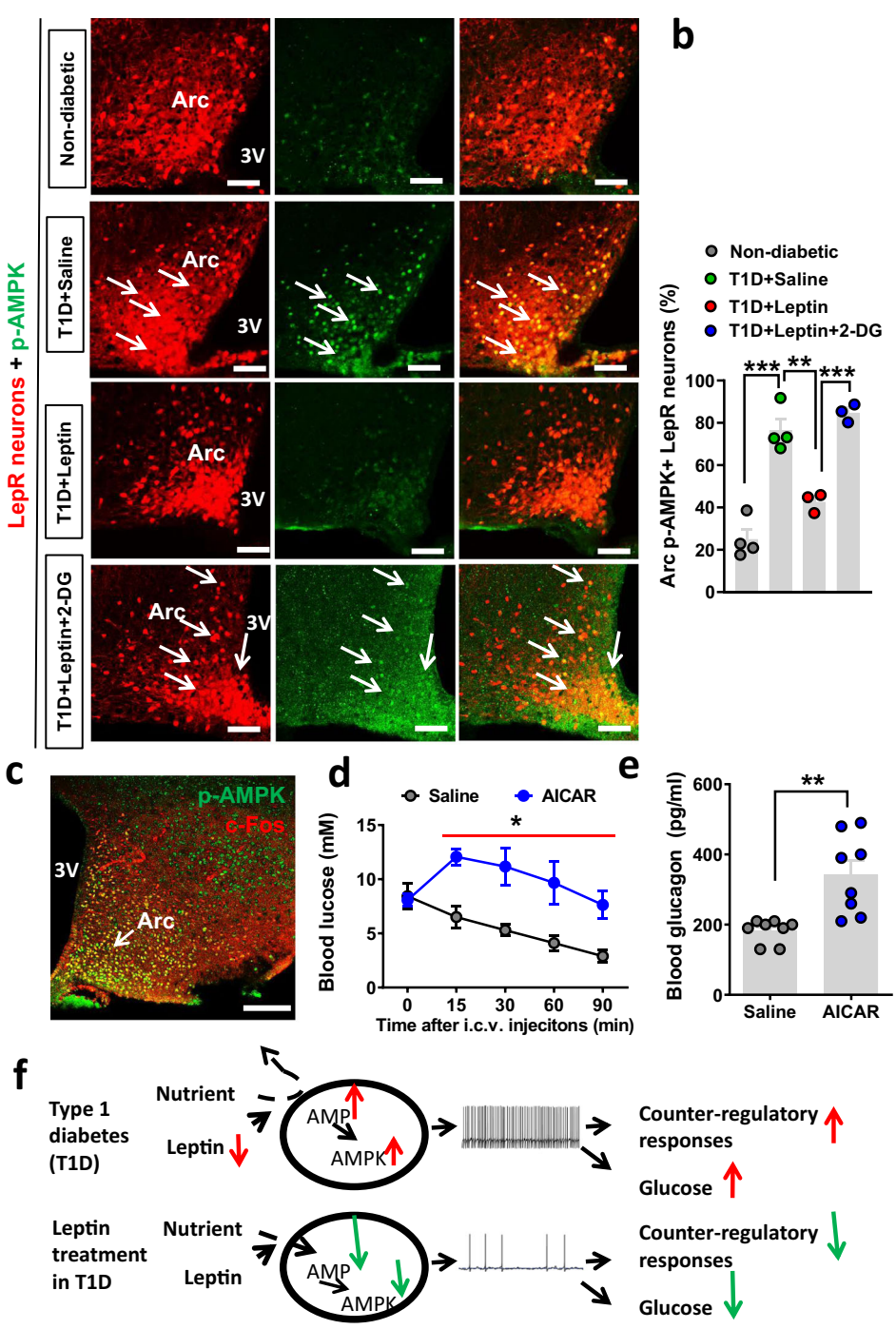


Fig. 7 T1D hyperglycemia and leptin action on reducing T1D hyperglycemia involve the AMPK pathway. a Representative immunostaining images from $n = 3$–4 mice as shown in **b** for p-AMPK in hypothalamic sections were shown from control (**a**, Non-diabetic), T1D with saline treatment (**a**, T1D + saline), T1D with leptin treatment (**a**, T1D + leptin), and T1D with both leptin and 2-DG treatments (T1D + leptin+2-DG) at fed conditions. **b** Comparison in the percentage of $LepR^{Arc}$ neurons with p-AMPK expression among the four groups (one-way ANOVA, $n = 4$ for nondiabetic controls and T1D-saline and $n = 3$ for T1D-leptin and T1D-leptin-2-DG, $F(3, 10) = 42.27$, $^{***}P < 0.0001$, nondiabetes vs T1D-saline; $^{**}P = 0.0051$, T1D-saline vs T1D-leptin; $^{***}P = 0.004$, T1D-leptin vs T1D-leptin-2_DG). **c** Representative pictures from $n = 1$ mouse showing colocalization between p-AMPK (green) and c-Fos (red) in the Arc of T1D LepR-Cre mice. **d**, **e** Wild-type mice (8–9 weeks of age, males) were made T1D and then i.c.v. treated with leptin to restore euglycemia. These mice were then treated with i.c.v. injections of either saline or AICAR, an agonist of AMPK. Comparisons in blood glucose were shown following i.c.v. AICAR (**d**, two-way ANOVA, $n = 3$/each, $F(1, 20) = 35.91$, $^{*}P = 0.0374$, saline vs AICAR at the 90-min time point) and in blood glucagon at 90 min after AICAR injection (**e**, two-tailed unpaired Student's t tests, $n = 8$/each, $t = 3.862$, df = 14; $n = 9$/each, $^{**}P = 0.0017$). **f** Diagram depicting hyperglycemia in T1D caused by heightened Arc GABAergic neuron activity due to energy deprivation and low leptin levels (top) and euglycemia restoration by leptin inhibition of neuron activity through reversing energy deprivation (bottom). 3: the third ventricle and Arc: arcuate nucleus. Data presented as mean ± SEM. 3V the third ventricle, Arc arcuate nucleus; Scale bar: 100 μM.

leptin action on T1D glucose. Previous studies suggest the importance of the melanocortin pathway, and especially AgRP neurons, in mediating leptin action[16–19]. Given the extensive research focus on AgRP neurons, the roles for non-AgRP Arc neurons have largely been neglected. Mice with AgRP neuron lesions developed T1D hyperglycemia in response to STZ and importantly, leptin action in reducing T1D hyperglycemia in these mice remained intact, suggesting that the presence of AgRP neurons is neither required for T1D hyperglycemia nor for mediating leptin action on reducing T1D hyperglycemia. Our results showed that activation of AgRP neurons exhibited a delayed reversal of leptin action, while chronic inhibition of these neurons led to a partial reduction in T1D glucose. These findings contrast a complete reversal of leptin action and leptin-mimicking effect by respective activation and inhibition of $GABA^{Arc}$ neurons, suggesting an important role for Arc GABAergic non-AgRP neurons in mediating the leptin action. A mild role for AgRP neurons in mediating the leptin action is supported by a recent study with DREADD-mediated manipulation of AgRP neuron activity[20]. Given the demonstrated c-Fos expression in a subset of GABAergic non-AgRP Arc neurons in T1D, these Arc GABAergic non-AgRP neurons may represent an important novel brain site for T1D pathogenesis. Of note, previously identified non-AgRP Trh/Cxcl12 GABAergic neurons in the Arc may represent one such group[22]. Further delineation of the functional identity of these neurons in their underlying neural pathway may reveal new insights on leptin action on reducing T1D hyperglycemia.

We provided several lines of evidence supporting that $LepR^{Arc}$ neurons are activated by energy deprivation in T1D. $LepR^{Arc}$ neurons were similarly activated in T1D and fasting, a condition with nutritional deprivation. Importantly, brain leptin infusion was potent in reducing circulating glucose in fasting associated with suppressing counter-regulatory hormone levels, all effects mimicking leptin action on reducing T1D hyperglycemia. Supporting this, except for blood glucose levels, T1D and fasting share many common features in blood hormones and physiology, including low insulin and leptin levels, and augmented counter-regulator responses[37]. In addition, $LepR^{Arc}$ neurons in T1D show a dramatic increase in the activation of AMPK, which is known to be an intracellular energy status sensor[36]. The colocalization of p-AMPK and c-Fos in the Arc provides direct evidence supporting that energy deprivation causes LepR neuron activation. Consistently, activation of AMPK also occurs in the hypothalamus during fasting and can be reversed by leptin[36]. It is striking that the sign of energy deprivation in $LepR^{Arc}$ neurons is accompanied with uncontrolled severe hyperglycemia in T1D. Moreover, $LepR^{Arc}$ neurons failed to respond to dramatic changes in blood glucose. In contrast to abundant induction of c-Fos in control $LepR^{Arc}$ neurons in response to a reduction of <2 mM glucose in controls, no changes were observed in c-Fos in T1D $LepR^{Arc}$ neurons with a change of >20 mM glucose. These lines of evidence collectively support a state of defective nutrient sensitivity of $LepR^{Arc}$ neurons in T1D. Colocalization of c-Fos and p-AMPK in T1D $LepR^{Arc}$ neurons suggests that these neurons are "locked" in a state of energy deprivation, signaling starvation and leading to heightened counter-regulatory responses, hyperglycemia, and other changes associated with starvation, all typical symptoms of T1D.

Our data suggest that leptin action on T1D $LepR^{Arc}$ neuron inhibition and hyperglycemia is mediated by reversal of energy deprivation in T1D $LepR^{Arc}$ neurons. Leptin effectively reduces the heightened activity of $LepR^{Arc}$ neurons in T1D, in a similar fashion to that occurring in fasting states. In addition, this action is accompanied by reversing the activation of AMPK. Importantly, leptin action can be reversed by 2-DG, a nutrient-depriving agent. Conversely, T1D $LepR^{Arc}$ neurons were not sensitive to 2-DG, but gained sensitivity in the presence of leptin, providing direct supporting evidence that leptin mediates nutrient sensitivity of these neurons. The reversal of energy deprivation by leptin is further corroborated by the effect of 2-DG in reversing leptin action on reducing T1D hyperglycemia, as well as inhibiting the heightened activity of Arc neurons, suggesting that leptin inhibition may be mediated by replenishing energy supply to these neurons. The mechanism underlying the leptin action in reversing energy deprivation is not clear, but may involve increased uptake of nutrient substrates, including blood glucose or lactate from glial cells[38,39]. Supporting this, previous observations suggest that glucose and leptin exert synergistic effects on intracellular leptin signaling[40]. In line with this, leptin action on presynaptic GABAergic input to POMC neurons is reduced by glucose and increased by the activation of AMP kinase[41], and AMPK plays a role in mediating leptin and glucose effects on LepR neurons[24,36,40,42]. Increased intracellular nutrient supply may inhibit neuron activity through membrane channels[28].

In our recording experiments, we focused on $LepR^{Arc}$ neurons that were inhibited by leptin, as these neurons are presumed to be the most relevant to T1D hyperglycemia due to their heightened activity associated with low leptin levels. The remaining leptin-excited $LepR^{Arc}$ neurons, including POMC neurons, may also be involved in glucose homeostasis[26]. However, as Arc GABAergic $LepR^{Arc}$ neurons are the primary mediator of the leptin action in T1D, POMC neurons, which are non-GABAergic[21], may contribute little to T1D hyperglycemia and leptin action in reducing T1D glucose.

Notably, a recent human clinical trial with a combination of insulin and leptin treatment of T1D shows that leptin reduces the dose of insulin for human T1D treatment, but without a dramatic effect on glucose[43]. Although this failed clinical trial, which is in contrast to the demonstrated leptin effect in rodents, may be due to many reasons, including potential differences between humans and rodents, one key difference in human T1D patients is that they are always on insulin treatment, and the leptin level is only reduced 50%, compared to non-T1D humans[5,44,45], presumably due to the reason that insulin is capable of increasing leptin levels[46,47]. In contrast, rodent T1D models are essentially insulinopenic and as a result, leptin levels are extremely low[1,2,46,48]. It is thus conceivable that an additional leptin dose on top of the mildly reduced leptin level in human T1D may not be able to provide additional beneficial effects. In other words, the beneficial effect of brain leptin action may have been reflected by the effects of insulin treatments[49]. Further studies are warranted to specifically address this possibility. In summary, our current study reveals that uncontrolled insulinopenic T1D represents a state of chronic fasting in terms of chronic activation of $LepR^{Arc}$ neurons owing to energy deprivation. Together, these data demonstrate that leptin action on reducing T1D hyperglycemia is mediated through reversing energy deprivation in $LepR^{Arc}$ neurons, leading to inhibition of these neurons, and reduced counter-regulatory responses. Thus, understanding the mechanism underlying leptin action on reversal in energy deprivation is imperative for a full understanding of T1D pathogenesis and more efficient treatment strategies against T1D.

Methods

Animals. All mice were housed with ad libitum access to water and food in a temperature-controlled room (21–22 °C) with a 12:12-h light–dark cycle. Animal testing and research follow all relevant ethical regulations. Animal care and procedures were approved by the Animal Welfare Committee of The University of Texas Health Science Center at Houston (Protocol # 18-021). LepR-Cre mice were bred to (ROSA)26Sortm9(CAG-tdTomato) (also called Ai9) reporter to generate LepR-Cre::Ai9 mice for electrophysiological recording or colocalization with c-Fos immunohistochemistry. AgRP-Cre and Vgat-Cre mice were obtained from the Jax Laboratory, and these mice were also bred with (ROSA)26Sortm1.1(CAG-cas9*,-EGFP) to allow visualization of AgRP and GABAergic neurons with GFP expression (GFP reporters). All mice that were used for stereotaxic injections were at least 8–10-weeks old. $AgRP^{DTR}$ mice were provided by Dr. Qi Wu of Baylor

College of Medicine and AgRP lesion with the injection of DTX (Sigma, St. Louis, MO). The experiments on the nonobese diabetes model (NOD, Jax lab) were performed in Shanghai University of Traditional Chinese Medicine (SUTCM) and the procedures were approved by the Animal Welfare Committee of SUTCM (Approval number: SZY20160900).

STZ-induced T1D. STZ (Sigma-Aldrich, St. Louis, MO) dissolved in cold-sterile acetate buffer, pH 4.5, was injected intraperitoneally (i.p.) to 6–8-week-old male mice at 150 mg/Kg (two times at 1-week intervals). Nondiabetic control mice received i.p. injection of acetate buffer alone. T1D was defined as nonfasting blood glucose >23 mM on 3 consecutive days.

Icv pump infusion studies. Recombinant mouse leptin (A.F. Parlow, National Hormone and Peptide Program, Torrance, CA) dissolved in phosphate-buffered saline (PBS, pH 8.0) was loaded into 14-day mini-osmotic pumps (DURECT Corporation, Cupertino, CA) that were connected with commercial brain infusion kits (DURECT Corporation). Pumps were surgically implanted in the mouse interscapular cavity 7 days after the establishment of T1D. All mice were anesthetized with ketamine (100 mg/Kg) and xylazine (10 mg/Kg), and then cannulas were stereotaxically positioned into the lateral cerebral ventricles using the coordinates: - 0.30 mm from the bregma, ± 1.0 mm lateral, and −2.5 mm of the skull. Leptin was continuously delivered at the speed of 50 ng per hour (0.25 μL/h) to the ventricles. T1D mice receiving the same amount of icv vehicle infusion were taken as controls. CNO (Sigma, St. Louis, MO) was i.p. injected at the dose of 1 mg/kg.

From day 3 after icv surgery, blood glucose levels, food intake, and body weight of all animals were recorded once every two days. All measurements were performed between 10:00 AM and 12:00 AM. Glucose levels were measured by using tail vein blood with OneTouch Glucometer.

For dual intracerebroventricular cannulation surgery, T1D mice were anesthetized and then cannulas were positioned into the left lateral cerebral ventricles with the coordinates: bregma, −0.5 mm, midline, −1.8 mm, and dorsal surface, −2.2 mm at a −10° angle. Meanwhile, minipumps with leptin (0.1 mg/ml, 100 μl/pump) were implanted into the right lateral cerebral ventricles with the coordinates: bregma, −0.5 mm, midline, +1.8 mm, and dorsal surface, −2.2 mm with a + 10° angle. 2-DG (2 mg/3 μl/mouse) was i.c.v. injected after 3-day recovery while leptin was pumping into the brain as well and blood glucose levels were measured.

Stereotaxic injections and viral vectors. Stereotaxic surgeries to deliver viral constructs were performed based on a revised previous protocol[7]. Briefly, mice were anesthetized with a ketamine/xylazine cocktail (100 and 10 mg/kg, respectively), and their heads affixed to a stereotaxic apparatus. Viral vectors were delivered through a 0.5-μL syringe (Neuros Model 7000.5 KH, point style 3, Hamilton, Reno, NV, USA) mounted on a motorized stereotaxic injector (Quintessential Stereotaxic Injector, Stoelting, Wood Dale, IL, USA) at a rate of 30 nL/min. Viral preparations were made through the Baylor NeuroConnectivity Core and Gene Vector Core with either serotype 5, 9, or DJ and titered at more than ~10^{12} particles/mL. Viral delivery was targeted to the Arc through four local injections with two each side (200 nL/side, anteroposterior (AP): −1.35 and −1.5 mm, mediolateral (ML): ± 0.2 mm, and dorsoventral (DV): −5.9 mm). AAV-DIO-hM3D(Gq)-mCherry, AAV-DIO-hM4D(Gi)-mCherry, AAV-EF1a-Flex-EGFP-P2A-mNachBac, or AAV-EF1a-DIO-Kir2.1-P2A-dTomato were delivered bilaterally into the Arc of AgRP-Cre or Vgat-Cre mice. For LepR-Cre, a volume of was injected into bilateral Arc instead. Two mutations (E224G and Y242F) were made in the Kir2.1 construct so that its activity will be less rectified by membrane potentials, thereby more effective in reducing neuron activity[50]. AAV-Flex-GFP or AAV-Flex-mCherry injections were used as a control group.

Blood collection and tissue processing. Blood samples were collected from all mice with deep anesthesia into a chilled tube containing 15 μl EDTA. Plasma was isolated by centrifugation (3000×*g* at 4 °C for 15 min), and then stored at −80 °C. After blood collection, all mice were transcardially perfused with 0.9% normal saline and followed by 10% formalin. Brain and pancreas were harvested and cryoprotected in 30% sucrose for further analysis. Plasma glucagon, insulin, and corticosterone were measured by the Vanderbilt University Hormone Assay & Analytical Services Core (Nashville, TN).

Immunohistochemistry (IHC). Brain sections were sliced with microtome (Leica, Germany) at 30-μm thickness. Phosphor-STAT3 (p-STAT3) was immunostained with rabbit anti-p-STAT3 antibody (1:400, Cell Signaling, Danvers, MA), p-AMPK (Cell Signaling, Danvers, MA) used at 1:1000, and c-Fos antibody (Millipore) used at 1:1000, the specificity of which was confirmed previously[51], or all brain sections were incubated with antibodies using free-floating methods with 24-well plates[52], and visualized with AlexaFluor 488- conjugated donkey anti-rabbit IgGs (1:500, Jackson ImmunoResearch Laboratories, West Grove, PA). The sections were photographed under a TCS SP5 confocal microscope (Leica). Neurons with clear immunostaining of c-Fos or p-AMPK were counted from four to five matched sections containing Arc from individual mice ($n = 3$–4/group) and the number of was averaged and compared using the indicated statistical methods.

Brain slice electrophysiological recordings. Coronal brain slices (250–300 μm) containing the arcuate nucleus of the hypothalamus (ARC) were cut in ice-cold artificial cerebrospinal fluid (aCSF) containing the following (in mM): 125 NaCl, 2.5 KCl, 1 $MgCl_2$, 2 $CaCl_2$, 1.25 NaH_2PO_4, 25 $NaHCO_3$, and 11 D-glucose bubbling with 95% O_2/5% CO_2. Slices containing the ARC were maintained for recovery for at least 1 h at 32–34 °C. Individual slices were transferred to a recording chamber mounted on an upright microscope (Olympus BX51WI) and continuously superfused (2 ml/min) with ACSF warmed to 32–34 °C by passing it through a feedback-controlled in-line heater (TC-324B, Warner Instruments). Cells were visualized through a ×40 water-immersion objective with differential interference contrast (DIC) optics and infrared illumination. Whole-cell current-clamp recordings were made from neurons with the tdTomato reporter fluorescence within the Arc. Patch pipettes (3–5 MΩ) were filled with a K^+-based low Cl^- an internal solution containing (in mM) 145 K-gluconate, 1 $MgCl_2$, 10 HEPES, 0.2 EGTA, 4 ATP, 0.3 GTP, and 10 phosphocreatine, pH 7.35, 270–285 mOsm. To test the glucose dose effect on neuronal firing, the osmolarity of the solution was balanced with sucrose. Mouse leptin (Harbor-UCLA Medical Center) at a concentration of 80 nM was perfused at 2 ml/min for up to 3 min to examine the effects of leptin on LepR neurons. To test $LepR^{Arc}$ neurons from T1D mice, brain sections were obtained 1 week after the establishment of T1D conditions with blood-glucose concentration >25 mM. For recording, we used bath 1 mM as a starting glucose concentration to mimicking a low glucose level, aiming for a higher level of baseline activity for leptin inhibitory action. We increased glucose levels from 1 to 10 mM, which grossly mimics high brain glucose levels in T1D, to examine the effect of glucose on neuron activity change.

Hormone measurement. Cheek blood from mice was collected and the serum was stored in a −80 °C freezer until measurement. Hormone measurements were performed either by ELISA kits from Millipore or by RIA kits at the Hormone Assay Core Facility of Vanderbilt University.

Statistical analysis. All data were presented as mean ± SEM. Statistical analyses were performed using Student's *t* tests or ANOVA tests with Tukey post hoc test as specified for each study (GraphPad Prism, GraphPad Software, La Jolla, CA). A P value <0.05 was considered significant.

Reporting summary. Further information on research design is available in the Nature Research Reporting Summary linked to this article.

Data availability

All data generated or analyzed during this study are included in this published article. Source data are provided with this paper.

Received: 19 February 2020; Accepted: 7 April 2021;
Published online: 11 May 2021

References

1. Wang, M. Y. et al. Leptin therapy in insulin-deficient type I diabetes. *Proc. Natl Acad. Sci. USA* **107**, 4813–4819 (2010).
2. Yu, X., Park, B. H., Wang, M. Y., Wang, Z. V. & Unger, R. H. Making insulin-deficient type 1 diabetic rodents thrive without insulin. *Proc. Natl Acad. Sci. USA* **105**, 14070–14075 (2008).
3. Fujikawa, T., Chuang, J. C., Sakata, I., Ramadori, G. & Coppari, R. Leptin therapy improves insulin-deficient type 1 diabetes by CNS-dependent mechanisms in mice. *Proc. Natl Acad. Sci. USA* **107**, 17391–17396 (2010).
4. Denroche, H. C. et al. Leptin therapy reverses hyperglycemia in mice with streptozotocin-induced diabetes, independent of hepatic leptin signaling. *Diabetes* **60**, 1414–1423 (2011).
5. Oberlin, D. & Buettner, C. How does leptin restore euglycemia in insulin-deficient diabetes? *J. Clin. Investig.* **127**, 450–453 (2017).
6. Fujikawa, T. et al. Leptin engages a hypothalamic neurocircuitry to permit survival in the absence of insulin. *Cell Metab.* **18**, 431–444 (2013).
7. Xu, Y., Chang, J. T., Myers, M. G. Jr., Xu, Y. & Tong, Q. Euglycemia restoration by central leptin in type 1 diabetes requires STAT3 signaling but not fast-acting neurotransmitter release. *Diabetes* https://doi.org/10.2337/db15-1160 (2016).
8. Lee, Y., Wang, M. Y., Du, X. Q., Charron, M. J. & Unger, R. H. Glucagon receptor knockout prevents insulin-deficient type 1 diabetes in mice. *Diabetes* **60**, 391–397 (2011).
9. Damond, N. et al. Blockade of glucagon signaling prevents or reverses diabetes onset only if residual beta-cells persist. *eLife* **5**, https://doi.org/10.7554/eLife.13828 (2016).
10. Perry, R. J. et al. Leptin reverses diabetes by suppression of the hypothalamic-pituitary-adrenal axis. *Nat. Med.* **20**, 759–763 (2014).

11. Perry, R. J., Petersen, K. F. & Shulman, G. I. Pleotropic effects of leptin to reverse insulin resistance and diabetic ketoacidosis. *Diabetologia* **59**, 933–937 (2016).
12. Morton, G. J., Meek, T. H., Matsen, M. E. & Schwartz, M. W. Evidence against hypothalamic-pituitary-adrenal axis suppression in the antidiabetic action of leptin. *J. Clin. Investig.* **125**, 4587–4591 (2015).
13. Meek, T. H. & Morton, G. J. The role of leptin in diabetes: metabolic effects. *Diabetologia* **59**, 928–932 (2016).
14. Singha, A. et al. Leptin receptors in RIP-Cre(25Mgn) neurons mediate anti-dyslipidemia effects of leptin in insulin-deficient mice. *Front. Endocrinol.* **11**, 588447 (2020).
15. Meek, T. H. et al. Leptin action in the ventromedial hypothalamic nucleus is sufficient, but not necessary, to normalize diabetic hyperglycemia. *Endocrinology* **154**, 3067–3076 (2013).
16. Meek, T. H. et al. Role of melanocortin signaling in neuroendocrine and metabolic actions of leptin in male rats with uncontrolled diabetes. *Endocrinology* **155**, 4157–4167 (2014).
17. da Silva, A. A., do Carmo, J. M., Freeman, J. N., Tallam, L. S. & Hall, J. E. A functional melanocortin system may be required for chronic CNS-mediated antidiabetic and cardiovascular actions of leptin. *Diabetes* **58**, 1749–1756 (2009).
18. Xu, J. et al. Genetic identification of leptin neural circuits in energy and glucose homeostases. *Nature* **556**, 505–509 (2018).
19. Goncalves, G. H., Li, W., Garcia, A. V., Figueiredo, M. S. & Bjorbaek, C. Hypothalamic agouti-related peptide neurons and the central melanocortin system are crucial mediators of leptin's antidiabetic actions. *Cell Rep.* **7**, 1093–1103 (2014).
20. Uner, A. G. et al. Role of POMC and AgRP neuronal activities on glycaemia in mice. *Sci. Rep.* **9**, 13068 (2019).
21. Vong, L. et al. Leptin action on GABAergic neurons prevents obesity and reduces inhibitory tone to POMC neurons. *Neuron* **71**, 142–154 (2011).
22. Campbell, J. N. et al. A molecular census of arcuate hypothalamus and median eminence cell types. *Nat. Neurosci.* **20**, 484–496 (2017).
23. Kim, G. H. et al. Leptin recruits Creb-regulated transcriptional coactivator 1 to improve hyperglycemia in insulin-deficient diabetes. *Mol. Metab.* **4**, 227–236 (2015).
24. Mountjoy, P. D., Bailey, S. J. & Rutter, G. A. Inhibition by glucose or leptin of hypothalamic neurons expressing neuropeptide Y requires changes in AMP-activated protein kinase activity. *Diabetologia* **50**, 168–177 (2007).
25. Qiu, J., Fang, Y., Ronnekleiv, O. K. & Kelly, M. J. Leptin excites proopiomelanocortin neurons via activation of TRPC channels. *J. Neurosci.* **30**, 1560–1565 (2010).
26. Berglund, E. D. et al. Direct leptin action on POMC neurons regulates glucose homeostasis and hepatic insulin sensitivity in mice. *J. Clin. Investig.* **122**, 1000–1009 (2012).
27. Djogo, T. et al. Adult NG2-Glia are required for median eminence-mediated leptin sensing and body weight control. *Cell Metab.* **23**, 797–810 (2016).
28. Baver, S. B. et al. Leptin modulates the intrinsic excitability of AgRP/NPY neurons in the arcuate nucleus of the hypothalamus. *J. Neurosci.* **34**, 5486–5496 (2014).
29. Williams, K. W. et al. Segregation of acute leptin and insulin effects in distinct populations of arcuate proopiomelanocortin neurons. *J. Neurosci.* **30**, 2472–2479 (2010).
30. Gao, Y. et al. TrpC5 mediates acute leptin and serotonin effects via pomc neurons. *Cell Rep.* **18**, 583–592 (2017).
31. Qiu, J., Wagner, E. J., Ronnekleiv, O. K. & Kelly, M. J. Insulin and leptin excite anorexigenic pro-opiomelanocortin neurones via activation of TRPC5 channels. *J. Neuroendocrinol.* **30**, https://doi.org/10.1111/jne.12501 (2018).
32. Zhu, C. et al. Profound and redundant functions of arcuate neurons in obesity development. *Nat. Metab.* **2**, 763–774 (2020).
33. Zhu, C. et al. Disrupted hypothalamic CRH neuron responsiveness contributes to diet-induced obesity. *EMBO Rep.* **21**, e49210 (2020).
34. Kim, E. R. et al. Paraventricular hypothalamus mediates diurnal rhythm of metabolism. *Nat. Commun.* **11**, 3794 (2020).
35. Luquet, S., Perez, F. A., Hnasko, T. S. & Palmiter, R. D. NPY/AgRP neurons are essential for feeding in adult mice but can be ablated in neonates. *Science* **310**, 683–685 (2005).
36. Minokoshi, Y. et al. AMP-kinase regulates food intake by responding to hormonal and nutrient signals in the hypothalamus. *Nature* **428**, 569–574 (2004).
37. Xu, Y. & Tong, Q. Central leptin action on euglycemia restoration in type 1 diabetes: restraining responses normally induced by fasting? *Int. J. Biochem. Cell Biol.* https://doi.org/10.1016/j.biocel.2016.09.027 (2016).
38. Magistretti, P. J. & Allaman, I. Lactate in the brain: from metabolic end-product to signalling molecule. *Nat. Rev. Neurosci.* **19**, 235–249 (2018).
39. Yellen, G. Fueling thought: Management of glycolysis and oxidative phosphorylation in neuronal metabolism. *J. Cell Biol.* **217**, 2235–2246 (2018).
40. Su, H., Jiang, L., Carter-Su, C. & Rui, L. Glucose enhances leptin signaling through modulation of AMPK activity. *PLoS ONE* **7**, e31636 (2012).
41. Lee, D. K., Jeong, J. H., Chun, S. K., Chua, S. Jr. & Jo, Y. H. Interplay between glucose and leptin signalling determines the strength of GABAergic synapses at POMC neurons. *Nat. Commun.* **6**, 6618 (2015).
42. Claret, M. et al. AMPK is essential for energy homeostasis regulation and glucose sensing by POMC and AgRP neurons. *J. Clin. Investig.* **117**, 2325–2336 (2007).
43. Vasandani, C., Clark, G. O., Adams-Huet, B., Quittner, C. & Garg, A. Efficacy and safety of Metreleptin therapy in patients with type 1 diabetes: a pilot study. *Diabetes Care* **40**, 694–697 (2017).
44. Hanaki, K., Becker, D. J. & Arslanian, S. A. Leptin before and after insulin therapy in children with new-onset type 1 diabetes. *J. Clin. Endocrinol. Metab.* **84**, 1524–1526 (1999).
45. Hathout, E. H. et al. Changes in plasma leptin during the treatment of diabetic ketoacidosis. *J. Clin. Endocrinol. Metab.* **84**, 4545–4548 (1999).
46. Havel, P. J. et al. Marked and rapid decreases of circulating leptin in streptozotocin diabetic rats: reversal by insulin. *Am. J. Physiol.* **274**, R1482–R1491 (1998).
47. Sivitz, W. I. et al. Plasma leptin in diabetic and insulin-treated diabetic and normal rats. *Metabolism* **47**, 584–591 (1998).
48. German, J. P. et al. Leptin deficiency causes insulin resistance induced by uncontrolled diabetes. *Diabetes* **59**, 1626–1634 (2010).
49. Zouhar, P. et al. UCP1-independent glucose-lowering effect of leptin in type 1 diabetes: only in conditions of hypoleptinemia. *Am. J. Physiol. Endocrinol. Metab.* **318**, E72–E86 (2020).
50. Xue, M., Atallah, B. V. & Scanziani, M. Equalizing excitation-inhibition ratios across visual cortical neurons. *Nature* **511**, 596–600 (2014).
51. Fan, S. et al. An indirect action contributes to C-Fos induction in paraventricular hypothalamic nucleus by neuropeptide Y. *Sci. Rep.* **6**, 19980 (2016).
52. Xu, Y. et al. Glutamate mediates the function of melanocortin receptor 4 on Sim1 neurons in body weight regulation. *Cell Metab.* **18**, 860–870 (2013).

Acknowledgements

This study was supported by NIH R01 DK114279 and R21NS108091 (Q.T.), R01DK109934 and DOD W81XWH-19-1-0429 (Q.T. and B.R.A.), NIH R01 DK120858 (Q.T. and Yong X.), NIH R01DK117281 and R01DK101379 (Yong X.), NIH R01DK 109194 and USDA/CRIS grant 3095-5-001-059 (Q.W.), and NIH R01MH117089 and McKnight Foundation (M.X.). We also acknowledge the Neuroconnectivity Core funded by NIH IDDRC grant 1 U54 HD083092 and Baylor College of Medicine Gene Vector Core for providing AAV vectors. S.F. was supported by the Graduate Student Overseas Study Program (B11-1-8) from Shanghai University of Chinese Traditional Medicine. We would like to acknowledge the Tong lab members for helpful discussion, Dr. Zhengmei Mao for help with microscopy. Q.T. is the holder of Cullen Chair in Molecular Medicine at McGovern Medical School.

Author contributions

S.F. conducted the research with help from Yuanzhong X., Y.L., Z.J., J.C.M., J.C., and H. L.; Q.W., M.X., B.R.A., and Yong X. provided essential reagents; Q.T. and C.H. conceived and designed the experiments, and wrote the paper with significant inputs from Q.W. and Yong X.

Competing interests

The authors declare no competing interests.

Additional information

Supplementary information The online version contains supplementary material available at https://doi.org/10.1038/s41467-021-22940-4.

Correspondence and requests for materials should be addressed to C.H. or Q.T.

Peer review information *Nature Communications* thanks Mark Evans and the other anonymous reviewer(s) for their contribution to the peer review of this work. Peer reviewer reports are available.

Reprints and permission information is available at http://www.nature.com/reprints

Publisher's note Springer Nature remains neutral with regard to jurisdictional claims in published maps and institutional affiliations.

Open Access This article is licensed under a Creative Commons Attribution 4.0 International License, which permits use, sharing, adaptation, distribution and reproduction in any medium or format, as long as you give appropriate credit to the original author(s) and the source, provide a link to the Creative Commons license, and indicate if changes were made. The images or other third party material in this article are included in the article's Creative Commons license, unless indicated otherwise in a credit line to the material. If material is not included in the article's Creative Commons license and your intended use is not permitted by statutory regulation or exceeds the permitted use, you will need to obtain permission directly from the copyright holder. To view a copy of this license, visit http://creativecommons.org/licenses/by/4.0/.

© The Author(s) 2021

frontiers in Cellular Neuroscience

ORIGINAL RESEARCH
published: 02 February 2021
doi: 10.3389/fncel.2021.635837

Dynamic Cholinergic Tone in the Basal Forebrain Reflects Reward-Seeking and Reinforcement During Olfactory Behavior

Elizabeth Hanson[1], *Katie L. Brandel-Ankrapp*[2] *and Benjamin R. Arenkiel*[1]*

[1] Department of Molecular and Human Genetics, Baylor College of Medicine, Houston, TX, United States,
[2] Postbaccalaureate Research Education Program, Baylor College of Medicine, Houston, TX, United States

Sensory perception underlies how we internalize and interact with the external world. In order to adapt to changing circumstances and interpret signals in a variety of contexts, sensation needs to be reliable, but perception of sensory input needs to be flexible. An important mediator of this flexibility is top-down regulation from the cholinergic basal forebrain. Basal forebrain projection neurons serve as pacemakers and gatekeepers for downstream neural networks, modulating circuit activity across diverse neuronal populations. This top-down control is necessary for sensory cue detection, learning, and memory, and is disproportionately disrupted in neurodegenerative diseases associated with cognitive decline. Intriguingly, cholinergic signaling acts locally within the basal forebrain to sculpt the activity of basal forebrain output neurons. To determine how local cholinergic signaling impacts basal forebrain output pathways that participate in top-down regulation, we sought to define the dynamics of cholinergic signaling within the basal forebrain during motivated behavior and learning. Toward this, we utilized fiber photometry and the genetically encoded acetylcholine indicator GAChR2.0 to define temporal patterns of cholinergic signaling in the basal forebrain during olfactory-guided, motivated behaviors and learning. We show that cholinergic signaling reliably increased during reward seeking behaviors, but was strongly suppressed by reward delivery in a go/no-go olfactory-cued discrimination task. The observed transient reduction in cholinergic tone was mirrored by a suppression in basal forebrain GABAergic neuronal activity. Together, these findings suggest that cholinergic tone in the basal forebrain changes rapidly to reflect reward-seeking behavior and positive reinforcement and may impact downstream circuitry that modulates olfaction.

Keywords: acetylcholine, olfaction, basal forebrain, go/no-go, reward, discrimination, GABA, top-down

OPEN ACCESS

Edited by:
Shaina M. Short,
The University of Utah, United States

Reviewed by:
Christiane Linster,
Cornell University, United States
Jocelyn M. Richard,
University of Minnesota Twin Cities, United States

***Correspondence:**
Benjamin R. Arenkiel
arenkiel@bcm.edu

Specialty section:
This article was submitted to Cellular Neurophysiology, a section of the journal Frontiers in Cellular Neuroscience

Received: *30 November 2020*
Accepted: *11 January 2021*
Published: *02 February 2021*

Citation:
Hanson E, Brandel-Ankrapp KL and Arenkiel BR (2021) Dynamic Cholinergic Tone in the Basal Forebrain Reflects Reward-Seeking and Reinforcement During Olfactory Behavior. Front. Cell. Neurosci. 15:635837. doi: 10.3389/fncel.2021.635837

INTRODUCTION

Rapid and precise sensory processing is critical for properly interpreting the external world. As a chemical sense, olfaction requires the ability to sample a vast, non-continuous sensory space with a wide range of stimulus intensities (Ache and Young, 2005). For this, the olfactory system must quickly separate and identify trace amounts of volatilized signals from a complex, noisy background (Rokni et al., 2014). However, as an animal moves through the world, the contexts in which it

encounters odors, as well as its own internal drives, are constantly changing. Therefore, olfactory processing must be flexible as well as sensitive in order to facilitate these changing needs. Flexible olfactory processing depends, in part, on top-down regulation (Restrepo et al., 2009; Pashkovski et al., 2020). Top-down regulation is a feature of sensory systems through which information about an animal's context, internal state, or previous experience modulates circuit function to sculpt the way stimuli are perceived (Gilbert and Sigman, 2007). In olfaction, for example, top-down regulatory mechanisms are recruited during active sensing in ways that improve odor detection and discrimination (Jordan et al., 2018), allow odor detection within a single sniff (Laing, 1986; Rinberg et al., 2006), and facilitate adaptive filtering during high frequency bouts of sniffing (Verhagen et al., 2007). Top-down regulation also allows for rapid changes in odor responses depending on context (Kay and Laurent, 1999; Beshel et al., 2007; Kudryavitskaya et al., 2020), and directly influences plasticity within the olfactory system (Fletcher and Wilson, 2003; Fletcher and Chen, 2010; Lepousez et al., 2014; Hanson et al., 2020).

An important source of top-down regulation in olfaction comes from the horizontal limb of the diagonal band of Broca (HDB) in the basal forebrain (Zaborszky et al., 1986; Mandairon et al., 2006; Gracia-Llanes et al., 2010; Ma and Luo, 2012; Rothermel et al., 2014). Basal forebrain neurons mediate state-dependent top-down regulation through signaling mechanisms that span diverse time scales ranging from milliseconds to hours (Buzsaki et al., 1988; Détári et al., 1999; Muñoz and Rudy, 2014). Fast, phasic signals from the basal forebrain mediate effects of attention on sensory processing, decision making, and sensory cued task performance (Parikh et al., 2007; Lin and Nicolelis, 2008; Pinto et al., 2013; Muñoz and Rudy, 2014; Hangya et al., 2015; Gritton et al., 2016). It has long been hypothesized that basal forebrain cholinergic signaling in particular mediates attentional effects on sensory processing circuits (Mandairon et al., 2006; Herrero et al., 2008; Chaudhury et al., 2009; Ghatpande and Gelperin, 2009; Goard and Dan, 2009; Ma and Luo, 2012; Chapuis and Wilson, 2013; Zhan et al., 2013; Rothermel et al., 2014). However, it has also been found that that non-cholinergic neuronal activity better predicts behavioral variables associated with attention in an auditory-cued go/no-go task (Hangya et al., 2015). Additionally, a recent study has described anticipatory activity among both cholinergic and non-cholinergic neurons in the basal forebrain during an olfactory-cued go/no-go task (Nunez-Parra et al., 2020). Importantly, in agreement with these earlier studies (Dannenberg et al., 2015; Xu et al., 2015), cholinergic neurons were also noted to collateralize within the basal forebrain to influence the activity of neighboring non-cholinergic neurons during task performance (Nunez-Parra et al., 2020). Together, this evidence suggests that non-cholinergic basal forebrain neurons mediate effects of attention on sensory processing, and it raises the question of how communication between cell types within the basal forebrain controls state-dependent basal forebrain output.

Parallel cholinergic and GABAergic projections from the basal forebrain to the olfactory bulb mediate distinct features of top-down regulation (Böhm et al., 2020). Separately, the cholinergic and GABAergic projections control gain, signal-to-noise ratio, habituation, oscillatory activity, and odor discrimination (Ma and Luo, 2012; Nunez-Parra et al., 2013; Rothermel et al., 2014; Ogg et al., 2018; Villar et al., 2020). Though both types of basal forebrain projections are important modulators of olfactory bulb odor and sniff responses, the upstream mechanisms that control basal forebrain output remain largely unknown. Ultimately, understanding how the basal forebrain mediates state-dependent changes in olfactory processing requires a more detailed knowledge of signaling within the HDB, and how it controls HDB output during olfaction and complex olfactory-guided behavior.

Here we describe temporal patterns of cholinergic signaling within the HDB during an olfactory-cued go/no-go discrimination task where mice learn to associate one of two odors with a reward. Historically, monitoring acetylcholine directly, *in vivo*, with high temporal resolution, has been challenging. However, with the advent of the genetically encoded GPCR Activation-Based (GRAB) fluorescent sensor for acetylcholine (GACh2.0) we directly recorded rapid fluctuations in acetylcholine levels from freely moving, behaving animals (Jing et al., 2018). Combining targeted sensor expression with implanted fiber optics and fiber photometry, we directly recorded acetylcholine signaling from the basal forebrain chronically, during freely moving behavior. We found that acetylcholine levels within the basal forebrain are dynamic and bidirectionally regulated during performance of a go/no-go discrimination task. Reward seeking behavior reliably evoked rapid increases in HDB acetylcholine, while positive feedback transiently suppressed cholinergic tone. These dynamics suggest that local cholinergic signaling is rapidly modulated in the HDB circuitry and may impact basal forebrain output pathways important for regulating olfaction.

RESULTS

Fiber Photometry of a Genetically Encoded Acetylcholine Sensor Reveals Real-Time Cholinergic Signaling in the Basal Forebrain

Defining the temporal profile of basal forebrain cholinergic signaling during complex behavior is a necessary step in determining how local cholinergic signaling impacts HDB circuit function and state-dependent output. To directly monitor cholinergic signals within the basal forebrain we injected wildtype mice with an adeno-associated virus (AAV) engineered to drive pan-neuronal expression of the acetylcholine sensor GACh2.0 (AAV hsyn-GACh). At the same time, we implanted a fiberoptic over the HDB (**Figure 1A**). GACh is a genetically-encoded fusion of a conformationally sensitive GFP and muscarinic acetylcholine receptor that fluoresces in response to binding acetylcholine. Imaging GACh fluorescence with fiber photometry allowed us to directly record changes in cholinergic tone within the HDB. Viral expression and implant targeting were verified *post-hoc* in all mice via immunofluorescence and histology (**Figure 1B**). After implantation and injection, mice

were allowed to recover and given 3 weeks to express the sensor prior to photometric recordings (**Figure 1C**). We first examined cholinergic signaling in freely moving mice during exploration of an open field arena. For this, we video-recorded mice exploring an open field while simultaneously using fiber photometry to record activity-dependent changes in GACh fluorescence in the HDB (**Figures 1C,D**). During open field exploration, we observed both excitation and suppression events (**Figure 1E**). Notably, detected events were not correlated with motion or position in the open field (**Figure 1F**), and the amplitude of fluorescence signals (dF/F) were not correlated with speed (cm/s) over time (Pearson's correlation $= -0.043 \pm 0.025$, $N = 4$ animals, 1 session per animal). These results revealed frequent spontaneous cholinergic signaling events in the HDB during behavior, which was not triggered by, or directly correlated with, voluntary locomotion.

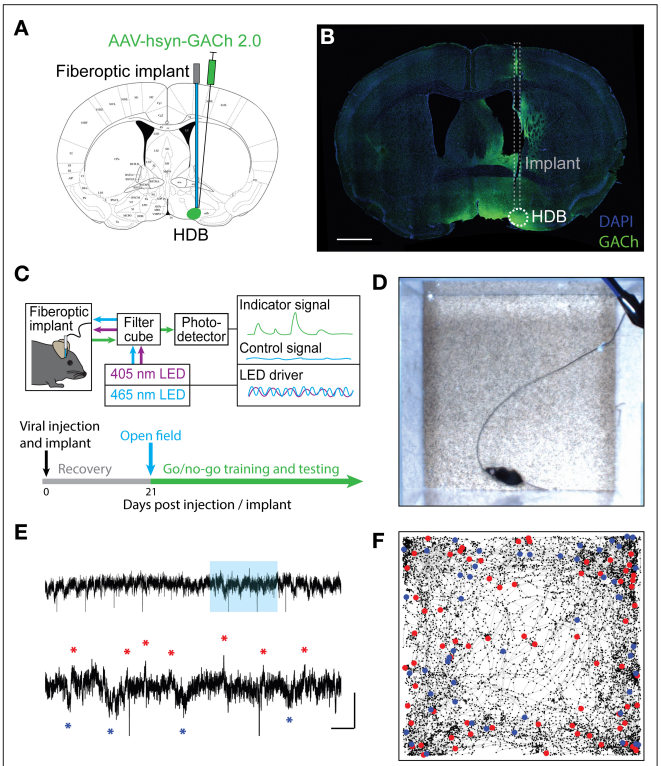


FIGURE 1 | Fiber photometry of a genetically encoded acetylcholine sensor in the HDB reveals real-time cholinergic signaling during freely moving behavior. **(A)** Coronal section schematic showing AAV injection and implant targeting the HDB. **(B)** IHC of a coronal section showing GACh2.0 expression and implant targeting in the HDB. Scale bar = 1 mm. **(C)** Schematic of photometry system showing light paths, LED control systems, filtering, and photodetection. Timeline of surgery, recovery, and photometry recording during open field exploration, followed by behavioral training and testing. **(D)** Still frame from video of open field exploration with photometric recording. **(E)** (Top panel) Isosbestic-subtracted GACh dF/F trace during open-field arena exploration. Y scale bar = 1 dF/F and X scale bar = 60 s. (Bottom panel) zoom of blue shaded portion of trace in top panel with excitation events marked with red asterisks and suppression events marked with blue asterisks. Y Scale bar = 1 dF/F, X scale bar = 10 s. **(F)** Track of mouse location over 20 min of open field exploration with locations corresponding to increases in HDB cholinergic signaling (excitation events) marked with red dots and decreases (suppression events) marked with blue dots.

Basal Forebrain Cholinergic Signaling Rapidly Fluctuates With Reward-Seeking and Positive Reinforcement

If HDB cholinergic signaling influences state-dependent basal forebrain output, we reasoned that the cholinergic reporter responses may dynamically change with behavioral states during the performance of complex, olfactory-guided, operant behaviors. To test this, we recorded photometry signals from freely moving mice performing an olfactory-cued go/no-go discrimination task ($N = 33$ sessions, 6 animals) (**Figures 2A,B**). Mice first underwent a shaping period of 10–14 days where they learned the mechanics of the task without photometry recording. During shaping, mice were trained to self-initiate trials by poking their nose into a port where they were presented with one of two odors. They then learned to distinguish between the delivery of an S+ odor, which indicated the availability of a water droplet at a separate reward port, and an S– odor, which indicated that no reward was available. A correct response to the S+ odor where a reward was obtained was considered a "Hit." A correct response to the S– odor where a new trial was initiated without reward-seeking was considered a "Correct Reject." An incorrect attempt to seek a reward after the S– odor was considered a "False Alarm" and an incorrect trial re-initiation after presentation of the S+ odor was considered a "Miss" (**Figure 2A**). Notably, this freely moving go/no-go task did not include punishment in response to False Alarms. Thus, feedback during odor-association learning was limited to positive reinforcement of a water reward in Hit trials, and negative reinforcement of a 4 s timeout after false alarms. This form of negative reinforcement is only mildly aversive, as demonstrated by a bias toward reward seeking trials (i.e., False Alarm Rate > Miss Rate) in all sessions where odors were effectively learned. Another feature of the freely moving task was that animals were required to self-initiate trials and reward seeking. Thus, the timing of trial initiation and reward seeking was determined entirely by the mouse, and it required both active engagement with the task and locomotion (**Figure 2B**).

Following the shaping period, we next recorded photometric signals from the basal forebrain while mice learned to discriminate novel odor pairs. As mice learned new odor pairs, accuracy within a block of 20 trials (calculated as (*Hits* + *Correct Rejects*)/(*Total Trials*)) increased. An odor pair was considered "learned" after two consecutive trial blocks with accuracy > 85% (**Figure 2C**). Once proficient at the task, mice typically learned new odor-reward associations within a single training session of 200–300 trials (Trials to learn $= 104.6 \pm 8.3$, $N = 56$ sessions, 12 animals). Using the timing of IR beam breaks at the odor port and reward port, individual trials of the go/no-go task were segmented into periods before and after trial initiation and, in the case of Hit and False Alarm trials, before and after reward seeking. Aligning trials by initiation times, and separating them by trial type, revealed distinct temporal patterns of cholinergic signaling in each trial (**Figure 2D**). Averaging across trials showed that bidirectional

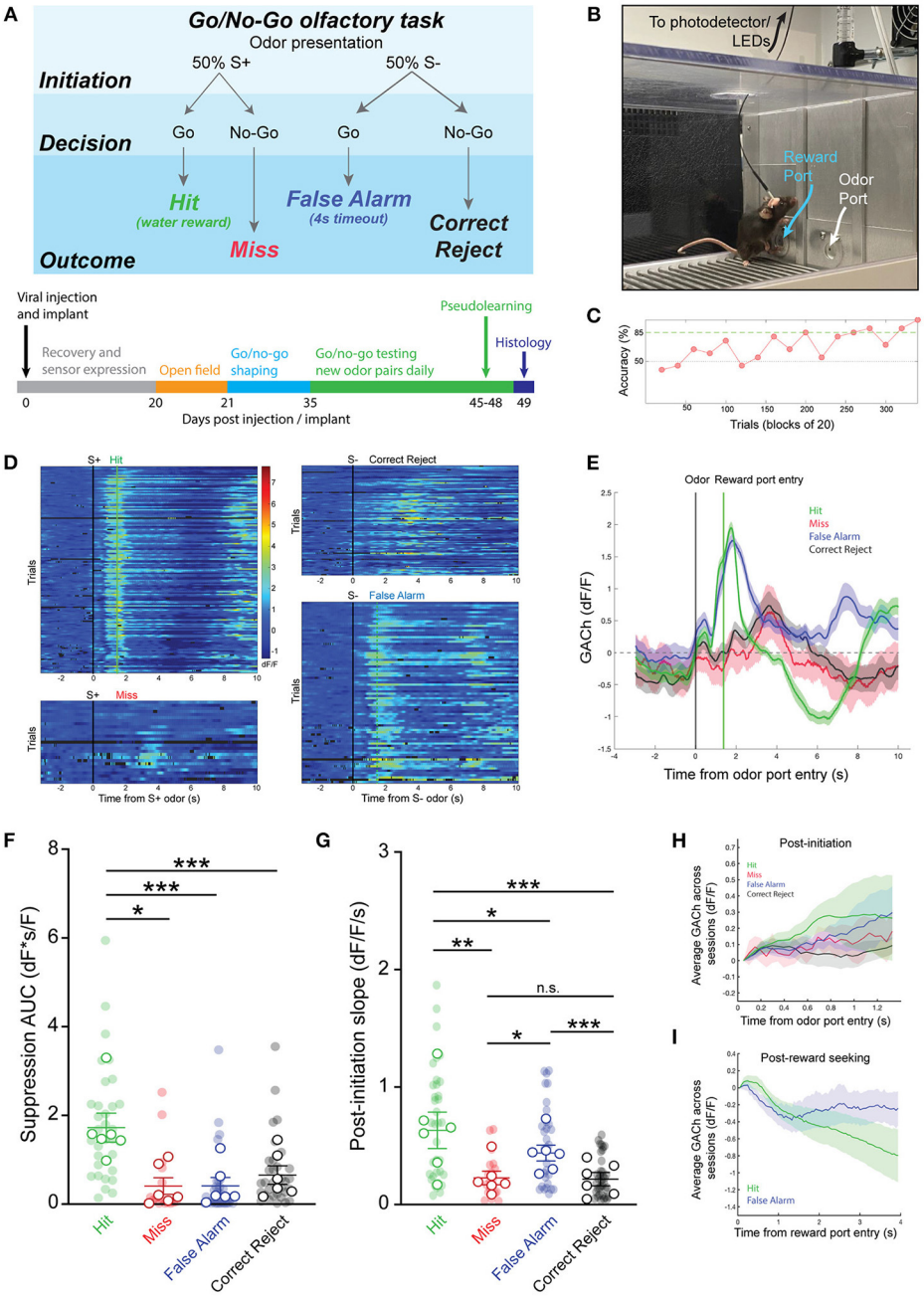


FIGURE 2 | Basal forebrain cholinergic signaling reflects reward-seeking and positive reinforcement in an olfactory-cued go/no-go discrimination task. **(A)** (Top panel) Schematic of olfactory-cued go/no-go discrimination task showing odor presentation, decisions, and possible trial outcomes (Hit, Miss, False Alarm, and Correct Reject). (Bottom panel) Timeline of surgery, recovery, and behavioral shaping and testing with photometry recording. **(B)** Picture of mouse performing go/no-go task during photometric recording. **(C)** Accuracy in blocks of 20 trials for a go/no-go testing session with novel odors highlighting chance (50%) and criteria (85%) levels. Accuracy is from the same session as the trials shown in **(D,E)**. **(D)** Heatmap showing isosbestic-subtracted GACh dF/F from individual trials in a single go/no-go testing session. Trials are aligned by trial initiation time and divided by trial outcome. **(E)** Average GACh dF/F traces for each trial type in the session shown in **(D)**. Shaded areas represent 95% confidence intervals. Black line marks trial initiation time. Green line marks the average reward port entry time in Hit and False Alarm trials. **(F)** Area under the curve of suppression below baseline across trial types and testing sessions. Transparent circles represent individual testing sessions. Hollow circles represent mean values from all sessions completed by individual mice. Lines and error bars show mean ± SEM of means from each animal. $^{*}p < 0.05$, $^{***}p < 0.001$ two-way nested repeated measures ANOVA with Tukey correction for multiple comparisons. **(G)** Slopes of GACh dF/F after trial initiation across trial types and testing sessions. Transparent circles represent individual testing sessions. Hollow circles represent mean values from all sessions completed by individual mice. Lines and error bars show mean ± SEM of means from each animal. $^{*}p < 0.05$, $^{**}p < 0.01$, $^{***}p < 0.001$ two-way nested repeated measures ANOVA with Tukey correction for multiple comparisons. **(H)** Average of mean GACh dF/F traces for across all sessions, separated by trial type, and baseline subtracted at the time of trial initiation. Shaded areas represent 95% confidence intervals. **(I)** Mean GACh dF/F traces for Hit and False alarm trials, averaged across all sessions, aligned to reward port entry time. Shaded areas represent 95% confidence intervals.

changes in HDB cholinergic signaling were consistent within trial types, but distinct across trials (**Figure 2E**).

A notable feature of the signal specific to Hit trials was the suppression of HDB cholinergic tone following reward delivery. The magnitude of the suppression, calculated as the area under the curve (AUC), was significantly larger in Hit trials (1.73 ± 0.33 dF*s/F) compared to Miss trials (0.42 ± 0.18 dF*s/F, $p < 0.05$), False Alarm trials (0.42 ± 0.12 dF*s/F, $p < 0.001$), or Correct Reject trials (0.66 ± 0.21 dF*s/F, $p < 0.001$) across animals and odor-pairs (**Figure 2F**). At the same time, in both Hit and False Alarm trials, HDB acetylcholine rapidly increased leading up to beam breaks at the reward port. Quantifying the slopes of the traces after odor delivery revealed that Hit trials exhibited steeper slopes (0.63 ± 0.12 dF/F/s) than Miss trials (0.23 ± 0.06 dF/F/s, $p < 0.01$), False Alarm trials (0.44 ± 0.07 dF/F/s, $p < 0.05$), and Correct Reject trials (0.22 ± 0.06 dF/F/s, $p < 0.001$). However, slopes in False Alarm trials were also significantly steeper compared to Miss ($p < 0.05$) and Correct Reject trials ($p < 0.001$) (**Figure 2G**). When post-initiation traces for each trial type were averaged across all sessions from every animal, however, the large variability between animals and sessions led to wide confidence intervals (**Figure 2H**). This supported a nested analysis within animals to compare trial types within sessions in a pairwise manner. However, even taking into account the variability in amplitude and timing across animals and sessions, the average traces from Hit and False Alarm trials showed a trend toward steeper slopes compared to the Correct Reject and Miss trials. Finally, to account for variability in the time to seek a reward in Hit and False Alarm trials, we aligned those traces to the reward-port entry times (as opposed to the trial initiation time), and averaged across all animals and sessions (**Figure 2I**). Correct Reject and Miss trials were excluded from this analysis since they did not include a reward port entry. Averaged post-reward seeking traces, with baseline subtracted at the time of reward-port entry, showed initial decreases in both trial types after reward-port entry. However, False Alarm trials quickly returned to baseline while Hit trials were further suppressed. Together, these data revealed increases in basal forebrain cholinergic tone which corresponded to reward seeking behavior in both Hit and False Alarm trials. However, only subsequent reward delivery in Hit trials led to a large, slow suppression of HDB cholinergic tone.

Reward-Seeking and Reinforcement Linked Patterns of HDB Cholinergic Signaling Are Independent of Learning

We next questioned whether patterns of cholinergic signaling in the HDB changed over the course of new odor-reward association learning. To determine this, we selected experiments with slower rates of learning, in which at least 3 blocks were performed with < 70% success, but criteria for learning were eventually met within 300 trials ($N = 16$ sessions, 5 animals). This paradigm allowed us to compare, within a testing session, cholinergic signaling from pre-learning blocks (blocks with < 70% accuracy), to responses after an odor association had been effectively learned (first two consecutive blocks and subsequent blocks > 85% accuracy) (**Figure 3A**). Comparing pre-learning vs. learned blocks revealed similar patterns of cholinergic signaling in the HDB during both reward seeking and after reward delivery in both Hit and False Alarm trials (**Figure 3B**). In agreement with the data from whole sessions (**Figure 2**), we found that the magnitude of the reward-related suppression in learned blocks was larger in Hit (1.60 ± 0.54 dF*s/F) than in False Alarm trials (0.57 ± 0.36 dF*s/F, $p < 0.05$). However, there was no difference in the magnitude of the reward-related suppression between pre-learning (Hit = 1.48 ± 0.42 dF*s/F, False Alarm = 0.47 ± 0.20 dF*s/F) compared to learned blocks in either Hit ($p = 0.96$) or False Alarm trials ($p = 0.99$) (**Figure 3C**). Additionally, across animals and odor pairs, the slope of the cholinergic signal after odor presentation was the same between pre-learning (Hit = 1.31 ± 0.32 dF/F/s, False Alarm = 0.90 ± 0.17 dF/F/s) and learned blocks (Hit = 1.41 ± 0.40 dF/F/s, False Alarm = 0.81 ± 0.19 dF/F/s) for both Hit ($p = 0.84$) and False Alarm trials ($p = 0.89$) (**Figure 3D**). These data suggest that HDB cholinergic signaling increases during reward seeking behavior and decreases with reward delivery, regardless of whether the odor-reward association has been effectively learned. These data, however, do not address whether patterns of HDB cholinergic signaling drive the formation of an odor-reward association, or depend on the context of an odor reward association.

Reward Related Suppression of HDB Cholinergic Signaling Is Task Dependent and Relies on Association Between Odor Cue and Reward

We next sought to determine whether patterns of basal forebrain cholinergic signaling were influenced by the context of the olfactory task, including the requirement for odor discrimination and the reliable association between odor and reward. An alternative possibility was that the observed pattern in HDB cholinergic signaling may simply reflect reward seeking and consumption behaviors, independent of odor discrimination or odor-reward association. While task dependence would suggest that HDB cholinergic signaling is involved in top-down regulation, the latter possibility would suggest that HDB cholinergic signaling responds to bottom-up cues. To distinguish between these possibilities, we recorded basal forebrain cholinergic signals during a version of the go/no-go task, in which there was no association between the odor presented and the availability of the reward (pseudo-learning, $N = 10$ sessions, 4 animals). In the pseudo-learning paradigm, S+ and S– odors were each presented 50% of the time, and a water reward was available on 50% of the trials at random (**Figure 4A**). This version of the task retains odor presentations, odor detection, reward seeking, and reward delivery, removing only the odor-reward association and the need for odor discrimination. Importantly, this also uncouples expectation from odor-evoked responses. During pseudo-learning, mice typically obtained ∼50% success rate with a mix of trial types biased toward positive, reward-seeking responses (Pseudo FA

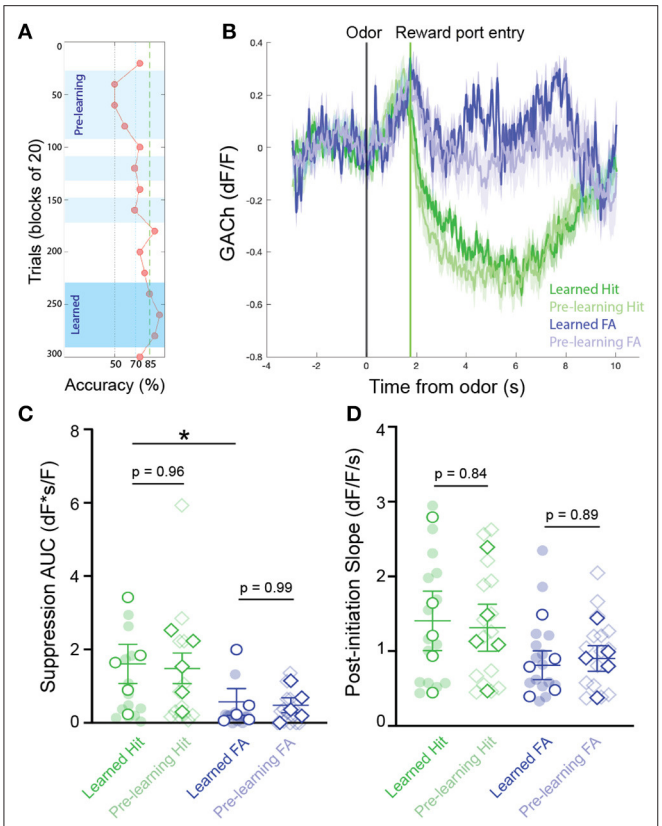


FIGURE 3 | Temporal profile of cholinergic signaling in the HDB does not change with within-session discrimination learning. **(A)** Accuracy in blocks of 20 trials for a go/no-go testing session highlighting blocks analyzed as "pre-learning" (light blue shading) and "learned" (dark blue shading). **(B)** Average GACh dF/F traces for Hit and False Alarm trials separated into pre-learning and learned trials. Shaded areas represent 95% confidence intervals. Black line marks trial initiation time. Green line marks the average reward port entry time. **(C)** Area under the curve of suppression below baseline across trial types in pre-learning and learned blocks. Transparent circles and diamonds represent individual testing sessions. Hollow opaque circles and diamonds represent mean values from all sessions completed by individual mice. Lines and error bars show mean ± SEM of means from each animal. *$p < 0.05$, two-way nested repeated measures ANOVA with Tukey correction for multiple comparisons. **(D)** Slopes of GACh dF/F after trial initiation across trial types in pre-learning and learned blocks. Transparent circles and diamonds represent individual testing sessions. Hollow opaque circles and diamonds represent mean values from all sessions completed by individual mice. Lines and error bars show mean ± SEM of means from each animal. Two-way nested repeated measures ANOVA with Tukey correction for multiple comparisons.

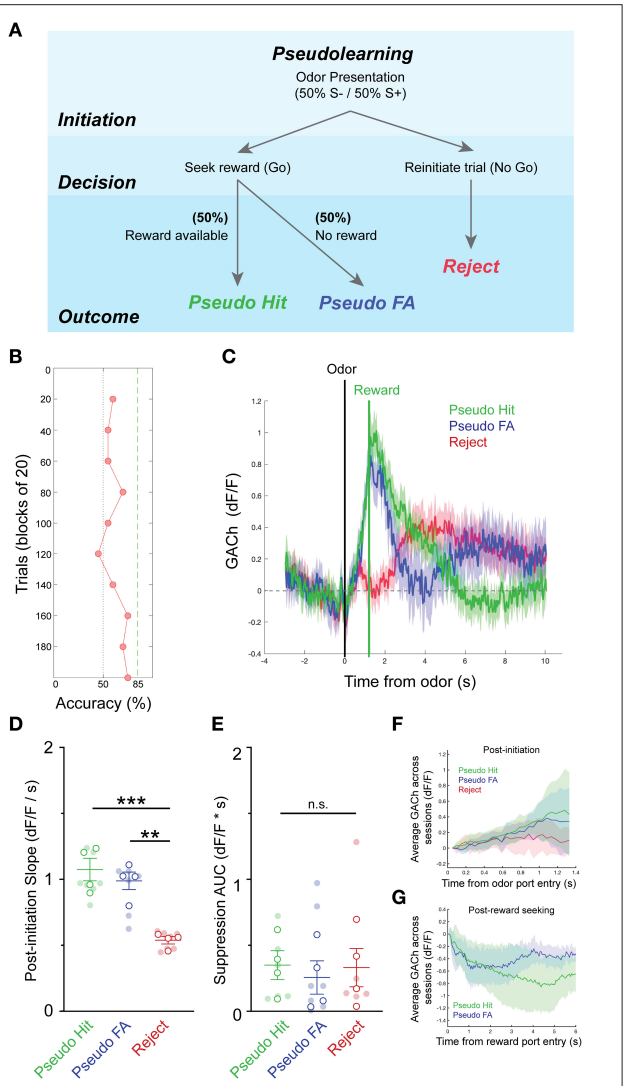


FIGURE 4 | Pseudo-learning reveals task-dependence of dynamic basal forebrain cholinergic tone. **(A)** Schematic of olfactory-cued go/no-go pseudo-learning task showing odor presentation, decisions, and possible trial outcomes (Pseudo-Hit, Pseudo-False Alarm, Reject). **(B)** Accuracy in blocks of 20 trials for a pseudo-learning testing session showing performance near chance. **(C)** Average GACh dF/F traces for Pseudo-Hit, Pseudo-False Alarm and Reject trials. Shaded areas represent 95% confidence intervals. Black line marks trial initiation time. Green line marks the average reward port entry time in reward-seeking trials. **(D)** Slopes of GACh dF/F after trial initiation across trial types and testing sessions. Transparent circles represent individual testing sessions. Hollow circles represent mean values from all sessions completed by individual mice. Lines and error bars show mean ± SEM of means from each animal. **$p < 0.01$, *** $p < 0.001$, two-way nested repeated measures ANOVA with Tukey correction for multiple comparisons. **(E)** Area under the curve of suppression below baseline across trial types and testing sessions. Transparent circles represent individual testing sessions. Hollow circles represent mean values from all sessions completed by individual mice. Lines and error bars show mean ± SEM of means from each animal. Two-way nested repeated measures ANOVA with Tukey correction for multiple comparisons. **(F)** Average of mean GACh dF/F traces for across all sessions, separated by trial type, and baseline subtracted at the time of trial initiation. Shaded areas represent 95% confidence intervals. **(G)** Mean GACh dF/F traces for Hit and False alarm trials, averaged across all sessions, aligned to reward port entry time. Shaded areas represent 95% confidence intervals.

and Pseudo Hit trials), and against negative (Reject) responses (**Figure 4B**).

Averaging across trials of the pseudo-learning task showed similar patterns of basal forebrain cholinergic signaling between Pseudo-Hit and Pseudo-FA trials, both of which differed from Reject trials (**Figure 4C**). In both Pseudo-Hits and Pseudo-FA trials, cholinergic signaling increased after odor presentation as mice seek rewards. This was reflected in significantly shallower slopes after trial initiation for Reject trials (0.54 ± 0.03 dF/F/s), compared to Pseudo-Hit trials (1.07 ± 0.09 dF/F/s, $p < 0.001$),

and Pseudo-FA trials (0.99 ± 0.07 dF/F/s, $p < 0.01$) (**Figure 4D**), suggesting that increased HDB acetylcholine reflects reward seeking behavior independent of an odor-reward association. Strikingly, however, we did not observe a slow suppression in cholinergic tone following reward delivery in Pseudo-Hit trials. The total magnitude of suppression was not larger in Pseudo-Hit trials (0.35 ± 0.12 dF*s/F) compared to Pseudo-FA (0.26 ± 0.13 dF*s/F, $p = 0.96$) or Reject trials (0.33 ± 0.15 dF*s/F, $p = 0.98$) (**Figure 4E**). Averaging across all sessions and animals revealed a trend toward a steadily increasing slope in Hit and False Alarm trials, while Reject trials flattened (**Figure 4F**). Aligning the False Alarm and Hit trials to the reward port entries revealed an initial decrease in traces from both trial types, though neither trial type showed strong prolonged suppression (**Figure 4G**). Together, these data indicate that the reward-related suppression of basal forebrain cholinergic tone does not merely reflect reward delivery or reward consumption. Rather, the suppression depends on the task context and requires an association between odor and reward. This suggests that anticipation of an available reward linked to an odor presentation is an important driver of the post-reward suppression.

HDB GABAergic Neuronal Activity Mirrors Cholinergic Tone in Response to Positive Reinforcement

Having revealed dynamic cholinergic signaling in the HDB during olfactory-guided behavior, we next examined a potential target of local cholinergic signaling. Basal forebrain GABAergic neurons express both metabotropic and nicotinic acetylcholine receptors, and have been shown to respond to local cholinergic signaling (Yang et al., 2014; Xu et al., 2015). We hypothesized that HDB GABAergic neuronal activity would be controlled, in part, by local cholinergic signaling and that GABAergic neuronal activity would follow a similar pattern of activation and suppression across phases of go/no-go task performance. To test this, we selectively expressed GCaMP in HDB GABAergic neurons by injecting an AAV encoding cre-dependent GCaMP6M (AAV flex-GCaMP6M) into Vgat-Cre mice (**Figure 5A**). We then recorded GABAergic neuronal activity via fiber photometry during performance of the go/no-go task. After behavioral shaping, new odor learning was accomplished within sessions of 200–300 trials (**Figure 5B**). Aligning individual trials by trial initiation time revealed bidirectional modulation of GABAergic neuronal activity with excitation following odor deliver and suppression following reward delivery in Hit trials (**Figures 5C,D**). Similar to the changes we observed in cholinergic tone, HDB GABAergic neuronal activity was reliably suppressed following reward delivery. Areas under the curve of the suppression below baseline were significantly larger in Hit trials (8.36 ± 1.25 dF*s/F) than in False Alarm (1.69 ± 0.48 dF*s/F, $p < 0.001$), Correct Reject (0.85 ± 0.30 dF*s/F, $p < 0.001$), or Miss trials (1.72 ± 0.94 dF*s/F, $p < 0.001$) (**Figure 5E**). In contrast to changes in cholinergic tone, however, HDB GABAergic neurons responded to both the S+ and S– odors. This was reflected in positive slopes of the GCaMP signal following trial initiation in Hit (1.67 ± 0.33 dF/F/s, $p < 0.05$), Miss (1.61 ± 0.26 dF/F/s, $p < 0.01$), False Alarm (1.64 ± 0.32 dF/F/s, $p < 0.05$), and Correct Reject trials (1.33 ± 0.24 dF/F/s, $p = < 0.05$) (**Figure 5F**). Additionally, slopes from different trial types were not significantly different from each other ($p = 0.34$). Even with large variability, comparing post-initiation traces for the four trial types, averaged across sessions and animals, further showed a ubiquitous and rapid GABAergic response to both S+ and S– odors (**Figure 5G**). This consistent response to both the S+ and S– odors implied that basal forebrain GABAergic neurons receive bottom-up olfactory information, and that their activity may reflect odor detection or active sensing. Finally, in contrast to the cholinergic signal, aligning False Alarm and Hit trials to reward port entries revealed no initial decrease in False Alarm trials, but a large and sustained suppression in Hit trials (**Figure 5H**). Together these data raise the intriguing possibility that HDB acetylcholine levels decrease in anticipation of a reward, while HDB GABAergic neuronal activity is suppressed by the reinforcement itself.

DISCUSSION

Sensory perception relies on a combination of bottom-up sensory input, and top-down behavioral state-dependent regulation. The basal forebrain serves as a key mediator of top-down regulation related to the behavioral states of attention, arousal, and wakefulness (Muir et al., 1993; Voytko et al., 1994; Szymusiak, 1995; Sarter and Bruno, 1999; Hasselmo and McGaughy, 2004; Herrero et al., 2008; Goard and Dan, 2009; Anaclet et al., 2015; Kim et al., 2015; Zant et al., 2016). Many of these effects are thought to be mediated by cholinergic signaling at downstream sensory circuits. Supporting this, in olfactory, visual, and auditory circuits, cholinergic neuromodulation has been shown to increase gain, improve signal to noise ratios, increase pattern separation, and increase the weight of bottom-up sensory input (Mandairon et al., 2006; Herrero et al., 2008; Chaudhury et al., 2009; Ghatpande and Gelperin, 2009; Goard and Dan, 2009; Ma and Luo, 2012; Chapuis and Wilson, 2013; Zhan et al., 2013; Rothermel et al., 2014). However, mounting evidence suggests that parallel GABAergic outputs from the basal forebrain also play a significant role sculpting downstream circuit activity (Nunez-Parra et al., 2013, 2020; Kim et al., 2015; Xu et al., 2015; Böhm et al., 2020; Villar et al., 2020).

In olfaction, input from the basal forebrain significantly impacts the earliest stages of signal transduction in the olfactory bulb. Separately, the cholinergic, and GABAergic projection pathways from the HDB drive distinct changes in olfactory bulb neuronal activity. For example, GABAergic projections from the HDB synapse onto inhibitory granule cells and periglomerular interneurons in the olfactory bulb where they mediate disinhibition and desynchronization of Mitral Cell firing bulb (Gracia-Llanes et al., 2010; Sanz Diez et al., 2019; Villar et al., 2020). Moreover, experiments implementing chemogenetic inhibition showed that basal forebrain GABAergic projections are required for effective odor discrimination (Nunez-Parra et al., 2020). On the other hand, other experiments have revealed that basal forebrain cholinergic projections to the olfactory

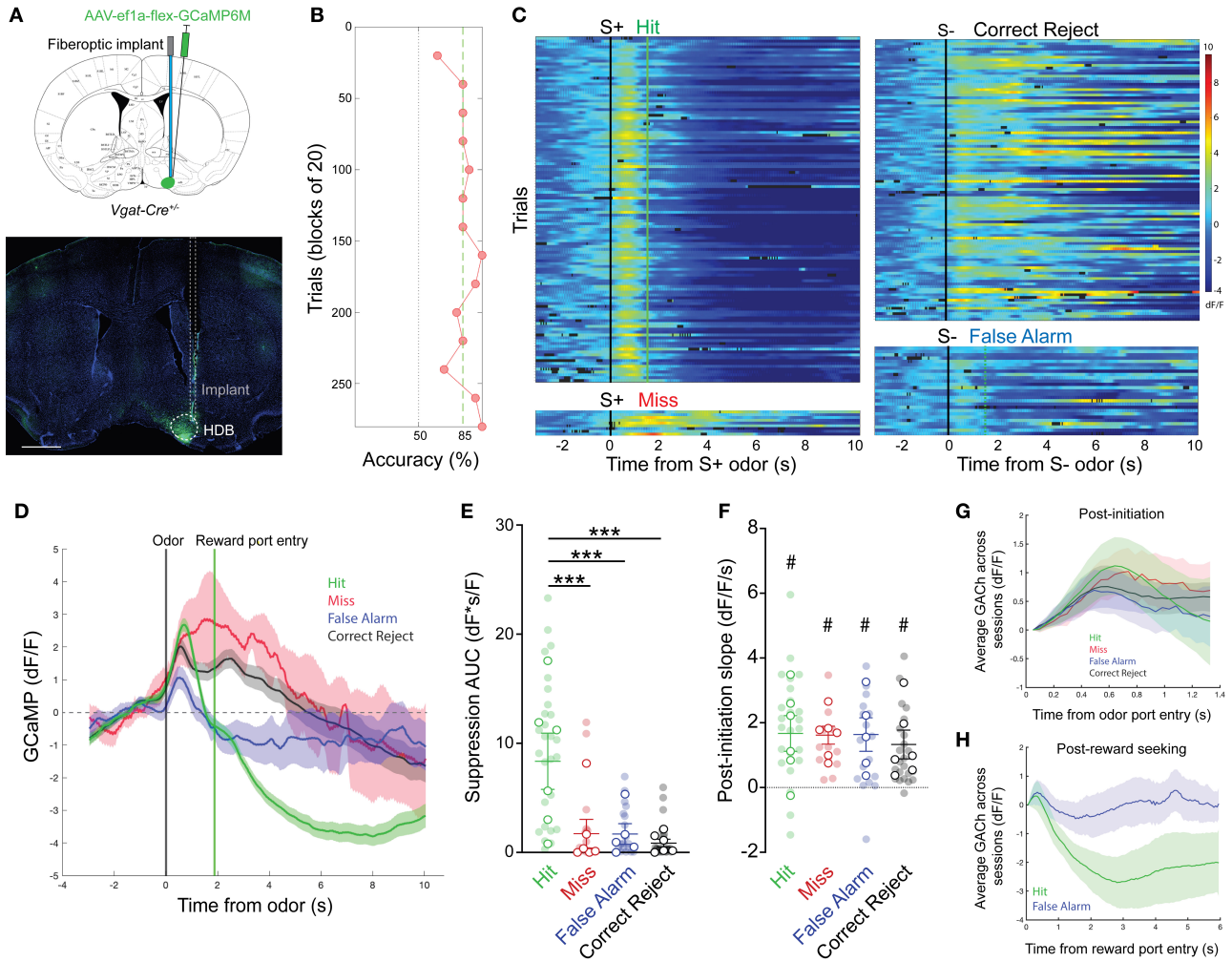


FIGURE 5 | HDB GABAergic neuronal activity mirrors cholinergic tone in response to positive reinforcement. **(A)** (Top panel) Coronal section schematic showing AAV injection and implant targeting the HDB. (Bottom panel) IHC of a coronal section showing GCaMP6M expression and implant targeting in the HDB. Scale bar = 1 mm. **(B)** Accuracy in blocks of 20 trials for a go/no-go testing session with novel odors highlighting chance (50%) and criteria (85%) levels. Accuracy is from the same session as the trials shown in **(D,E)**. **(D,C)** Heatmap showing isosbestic-subtracted GCaMP dF/F from individual trials in a single go/no-go testing session. Trials are aligned by trial initiation time and divided by trial outcome. **(D)** Average GCaMP dF/F traces for each trial type in the session shown in **(C)**. Shaded areas represent 95% confidence intervals. Black line marks trial initiation time. Green line marks the average reward port entry time in Hit and False Alarm trials. **(E)** Area under the curve of suppression below baseline across trial types and testing sessions. Transparent circles represent individual testing sessions. Hollow circles represent mean values from all sessions completed by individual mice. Lines and error bars show mean ± SEM of means from each animal. $^{***}p < 0.001$ two-way nested repeated measures ANOVA with Tukey correction for multiple comparisons. **(F)** Slopes of GCaMP dF/F after trial initiation across trial types and testing sessions. Transparent circles represent individual testing sessions. Hollow circles represent mean values from all sessions completed by individual mice. $\#p < 0.05$, nested one sample *t*-test comparing trial type values to 0. Two-way nested repeated measures ANOVA with Tukey correction for multiple comparisons shows $p = 0.36$ for differences between trial types. **(G)** Average of mean GCaMP dF/F traces for across all sessions, separated by trial type, and baseline subtracted at the time of trial initiation. Shaded areas represent 95% confidence intervals. **(H)** Mean GCaMP dF/F traces for Hit and False alarm trials, averaged across all sessions, aligned to reward port entry time. Shaded areas represent 95% confidence intervals.

bulb increase excitability, modulate signal to noise ratios in mitral cell firing, and can rapidly dishabituate olfactory bulb odor responses (Ma and Luo, 2012; Rothermel et al., 2014; Ogg et al., 2018). Finally, more recent studies have directly compared optogenetic stimulation of basal forebrain cholinergic and GABAergic terminals within the olfactory bulb (Böhm et al., 2020), describing that local stimulation of cholinergic terminals increased mitral cell firing during sniffing regardless of odor presentation, whereas stimulation of GABAergic terminals decreased spontaneous mitral cell firing and increased firing during sniffing only when odors were presented. Together, these findings imply that basal forebrain cholinergic and GABAergic neurons mediate distinct features of top-down regulation, and that both types of basal forebrain projections modulate olfactory bulb odor and sniff responses.

Importantly, cholinergic and GABAergic neurons in the basal forebrain work together to modulate downstream circuit function (Dannenberg et al., 2015; Böhm et al., 2020). An

outstanding question is how parallel cholinergic and GABAergic output pathways are coordinated during behavior at the level of the basal forebrain. In the current study, we show that cholinergic signaling within the basal forebrain is dynamically regulated during olfactory-guided behavior. We also show that distinct changes in basal forebrain cholinergic tone correspond to changes in neighboring GABAergic neuronal activity. These results raise the possibility that cholinergic signaling within the basal forebrain dynamically impacts basal forebrain output pathways, potentially relaying behavioral state information from the basal forebrain to the olfactory system.

Bidirectional Changes in Basal Forebrain Cholinergic Tone During Olfactory Task Performance

Though basal forebrain neuronal activity has been characterized across a variety of behavioral states and in a number of sensory discrimination and association learning tasks (Mandairon and Linster, 2009; Devore et al., 2015; Hangya et al., 2015; Xu et al., 2015; Harrison et al., 2016; Nunez-Parra et al., 2020), how this activity is regulated by local signaling within the basal forebrain remains largely unknown. To investigate local cholinergic signaling within the basal forebrain we used a GPCR Activation-Based sensor for acetylcholine (Jing et al., 2018) combined with fiber photometry. This approach allowed us to record changes in acetylcholine from the basal forebrain with sub-second temporal resolution, in freely behaving animals.

With this approach we were able to record rapid changes in cholinergic tone from the HDB during free exploration of an open field arena, and during olfactory-cued operant behavior. Basal forebrain neuronal activity has been previously correlated with locomotion and slow changes in arousal (Sarter and Bruno, 1999; Goard and Dan, 2009; Xu et al., 2015). However, while we observed frequent spontaneous activation and suppression signaling events during exploration, significant changes in GACh fluorescence were not correlated with locomotion. This highlights an interesting discrepancy between cholinergic neuron activity and the local cholinergic signaling itself. Our data indicate that basal forebrain acetylcholine changes on a rapid timescale, which was not solely reflective of slow changes in behavioral state. Instead, changes in basal forebrain cholinergic tone were temporally precise based on behavioral action. This raises the possibility that changes in HDB cholinergic tone reflect rapid changes in behavioral states that align with complex olfactory-guided behavior.

To examine cholinergic signaling dynamics during complex olfactory guided behavior, we tested mice on a freely moving, olfactory-cued go/no-go discrimination task. The task included self-initiation of trials, followed by periods of active sensing, odor detection, discrimination, reward-seeking, and positive/negative reinforcement. We hypothesized that cholinergic signaling would be dynamically regulated within trials of the go/no-go task, reflecting changing needs for basal forebrain mediated top-down regulation during different behaviors, and in response to reinforcement. Supporting this hypothesis, we observed rapid, bidirectional changes in acetylcholine that were time-locked to phases of the go/no-go task. Specifically, we found that acetylcholine increased rapidly in the basal forebrain during reward-seeking behavior. Once the availability of a reward was ascertained, acetylcholine responses decreased rapidly. Finally, if a reward was successfully obtained, acetylcholine decreased slowly, but transiently, below baseline levels. Recent studies reported decreased activity in a subset of basal forebrain neurons following both stimulus presentation and reward delivery (Nunez-Parra et al., 2020). However, in a small population of identified cholinergic neurons, no reliable changes in firing rate were detected with reward delivery. This discrepancy may further suggest a disconnect between neuronal activity and local cholinergic tone. Alternatively, these data may reflect differences in the task requirements between a freely moving task and previously described head-fixed experiments (Nunez-Parra et al., 2020). Ultimately, the complex cholinergic signaling dynamics that we observed suggest that local cholinergic signaling corresponds to distinct features of the go/no-go task, perhaps reflecting reward-seeking behavior and subsequent reward delivery. The reward-related suppression of cholinergic signaling in Hit trials was particularly interesting given the implication that a baseline cholinergic tone in the basal forebrain is selectively suppressed in response to positive feedback.

Task-Dependent and Learning-Independent Patterns of Cholinergic Signaling in the Basal Forebrain

These observations led us to question whether cholinergic signaling dynamics in the basal forebrain were (1) a driver of odor-reward association learning, (2) a consequence of association learning, or (3) independent of odor-reward association, and instead linked to the performance of task-related behaviors. To directly investigate these possibilities, we examined cholinergic signaling dynamics over the course of odor-reward association learning, and in the absence of odor-reward associations. If task-linked cholinergic signaling dynamics are a consequence of odor-reward association learning, we might have expected temporal profiles of cholinergic signaling to change over the course of single sessions, where new odor-reward associations are being learned. For example, reward expectation scales with increasing success over a go/no-go session as new odor-reward associations are effectively learned (Tremblay et al., 1998). Thus, if increased cholinergic signaling in the basal forebrain reflects reward expectation, we would expect reporter responses to change over the course of learning within sessions. Indeed, a recent study recording neuronal activity in the basal forebrain found that a higher percentage of cholinergic and non-cholinergic neurons changed their firing rates in response to an odor cue after an odor-reward association was learned in a go/no-go task (Nunez-Parra et al., 2020). However, examining cholinergic tone directly, we find that changes in acetylcholine during go/no-go trials are stable over the course of odor-reward association learning. Neither increased acetylcholine during reward-seeking, nor suppressed acetylcholine following reward delivery, change over the course of a learning session.

Intriguingly, rapid changes in basal forebrain cholinergic tone during reward seeking did not reflect the strength of reward expectation. Such stability of basal forebrain cholinergic signaling over the course go/no-go testing sessions suggests that acetylcholine release within the basal forebrain is either an upstream driver of learning—relating specific perceptual decisions to positive and negative outcomes—or it may be all together independent of odor-reward associations—reflecting only reward-seeking and reward-consumption behaviors.

To distinguish between these possibilities, we examined cholinergic signaling during pseudo-learning, a version of the go/no-go task in which rewards were randomly available 50% of the time, regardless of the odor presented. Pseudo-learning preserves odor detection (the animals can only seek a reward after receiving an odor presentation), reward seeking, and reward delivery, but removes the association between odor and reward. If basal forebrain cholinergic signaling is simply a reflection of behavioral responses (i.e., reward seeking and consumption) rather than changing behavioral states (i.e., expectation, attention, surprise, etc.), we would have expected to observe the same stable patterns of cholinergic signaling with reward-seeking and reward delivery that we observed in the go/no-go discrimination task. Alternatively, if basal forebrain cholinergic signaling serves a role in relating the odor-discrimination context of the task to reward seeking behavioral choices or positive reinforcement outcomes, we would expect to observe differences in the patten of HDB cholinergic signaling when the rules of the task are changed. Indeed, in the pseudo-learning task, removing the cue-reward association led to a decrease in the reward-related suppression of basal forebrain cholinergic tone. However, increased cholinergic tone during reward seeking behavior occurred regardless of odor-reward association. Surprisingly, patterns of basal forebrain cholinergic signaling were stable over the course of pseudo-learning sessions. It's possible that this was because mice quickly realized that the context of the task had changed and rapidly altered their strategy to fit the new rules of the pseudo-learning task. If so, the reward-related suppression of cholinergic signaling may not only reflect reward delivery but also take into account knowledge of the task itself.

Odor Evoked Activity and Reward Related Suppression of Basal Forebrain GABAergic Neurons During Olfactory Task Performance

GABAergic neurons in the HDB express cholinergic receptors and respond to local acetylcholine release (Yang et al., 2014; Xu et al., 2015). At the same time, GABAergic output from the HDB mediates distinct forms of top-down regulation important for state-dependent active sensing and odor discrimination (Nunez-Parra et al., 2013; Böhm et al., 2020). Having found that local cholinergic tone is dynamically regulated during performance of an olfactory-cued go/no-go task, we next examined whether changes in local cholinergic tone corresponded to changes in basal forebrain GABAergic neuronal activity. We reasoned that if HDB GABAergic neuronal activity is dynamically controlled by local cholinergic signaling, we might expect to observe correlations between temporal profiles of GABAergic neuronal activity and cholinergic tone during olfactory discrimination tasks. However, in contrast to the observed cholinergic signaling patterns, we observed GABAergic responses to both the S+ and S– odors across all trial types, regardless of reward seeking behavior. Intriguingly, recent studies report that stimulating GABAergic projections to the olfactory bulb enhanced sniff-locked odor responses from a subset of mitral cells, while suppressing spontaneous activity (Böhm et al., 2020). Inhibiting these projections, on the other hand, reduced odor discrimination (Nunez-Parra et al., 2013). In this context, our data show that HDB GABAergic neurons respond broadly during odor discrimination, and they suggest that they may mediate enhanced odor discrimination during active sniffing.

At the same time, we observed similar changes in cholinergic tone and GABAergic neuronal activity in response to positive reinforcement. Both GABAergic neuronal activity and cholinergic tone were suppressed following reward delivery in Hit trials. Suppression below baseline implies that a population of GABAergic neurons in the basal forebrain are tonically active. Notably, tonic and rhythmic neuronal firing has been observed in basal forebrain, and is strongly dependent on behavioral state (Nunez, 1996; Détári et al., 1999; Szymusiak et al., 2000). The similarity between the suppression of basal forebrain GABAergic neuronal activity and local cholinergic signaling following reward delivery suggests that activity of basal forebrain GABAergic neurons is influenced by local cholinergic tone. Importantly however, our data do not distinguish whether basal forebrain GABAergic neurons are a target of tonic excitement from local acetylcholine. Indeed, other studies have reported that cholinergic collateralization within the basal forebrain directly activates local non-cholinergic and/or GABAergic neurons (Yang et al., 2014; Dannenberg et al., 2015; Xu et al., 2015; Nunez-Parra et al., 2020). In this context, our data raise the possibility that higher ambient cholinergic tone and increased tonic activity of basal forebrain GABAergic neurons in awake states create an environment where such signals can be bidirectionally modulated to solidify learned cue-reward associations.

Here we have revealed rapid, bidirectional changes in cholinergic tone within the basal forebrain during complex, olfactory-guided behavior. Characterization of the cholinergic signal itself through visualization of the GACh reporter signal is a first step toward understanding how cholinergic drive influences basal forebrain circuitry, and thus, top-down regulation of sensory processing. Future work will be needed to determine the mechanistic impact of dynamic cholinergic tone on specific HDB projection neuron populations. The current data, however, support the idea that cholinergic tone changes rapidly in the basal forebrain during olfactory-guided behavior, making local cholinergic signaling an intriguing candidate for coordinating fast state-dependent effects on HDB circuits and projection outputs.

MATERIALS AND METHODS

Animals

Mice were maintained on a 12 h light-dark cycle and were treated in compliance with the US Department of Health

and Human Services and Baylor College of Medicine IACUC guidelines. C56Bl6/J and Vgat-cre mice underwent surgery at 2–4 months old. Equal numbers of male and female mice were included in each experiment. Vgat-Cre (*Slc32a1*tm2(cre) Lowl, Stock: 028862) mice were originally purchased from Jackson Laboratories.

Surgical Procedures

Mice were anesthetized with 4% isoflurane in O2 and maintained under anesthesia with 1–2% isoflurane in O_2. Craniotomies were made over the sites of stereotaxic injections and fiberoptic implants that were guided by Angle Two software (Leica) normalized to Bregma. To target viral expression to the HDB, a unilateral injection of virus was made into the left HDB (from Bregma: ML −1.0 mm, AP 0.1 mm, DV −5.45 mm). Viruses were packaged in-house and included AAV-hsyn-GACh2.0, Serotype DJ8 injected into C57Bl6/J (WT) mice and AAV-ef1α-flex-GCaMP6M, Serotype DJ8, injected into Vgat-cre mice. The plasmid containing GACh2.0 was a generous gift from the Yulong Li Lab (Jing et al., 2018). Two hundred and fifty Nanoliters of virus was injected into the HDB over 10 min. Following viral injection, the injection needle was removed and a custom fiber optic implant (0.48 na, 200 um core diameter, RWD systems) was lowered to a target 0.1 mm dorsal to the injection target. The implant was then fixed in place with Metabond dental cement (Parkell). Mice were allowed to recover for 3 weeks before behavioral experiments. HDB targeting was verified in all cases with immunofluorescence imaging of the implant track and viral expression within the HDB.

TABLE 1 | Monomolecular odors used in go/no-go shaping and testing.

Odorant	*Molar Mass (g/mol)*	*Vapor Pressure (mmHg)*	*Functional Group*
(–) Carvone	150.22	0.16	Cyclic ketone, 10C, 1 double bond
(+) Carvone	150.22	0.16	Cyclic ketone, 10C, 1 double bond
1-Butanol	74.12	7	Straight chain alcohol, 4C
1-heptanol	116.2	0.2163	Straight chain alcohol, 7C
1-Hexanol	102.18	1	Straight chain alcohol, 6C
1-Pentanol	88.15	44.6	Straight chain alcohol, 5C
Acetophenone	120.15	0.397	Aromatic ketone
alpha-Pinene	136.24	3	Cyclic, 7C, 1 double bond
Citral	152.24	0.22	Aldehyde, 10C
Ethyl Acetate	88.11	93.2	Ester, 4C
Eucalyptol	154.249	1.9	Cyclic ether, monoterpinoid
Eugenol	164.2	0.0221	Aromatic alcohol, ether
Isoamyl acetate	130.19	4	Ester, 7C
(–) Limonene	150.22	0.16	Cyclic monoterpene, 10C, 2 double bonds
(+) Limonene	150.22	0.16	Cyclic monoterpene, 10C, 2 double bonds
Menthone	154	0.895	Cyclic ketone, 10C, no double bonds
Methyl Acetate	74.08	173	Ester, 3C
Methyl Salicylate	152.15	0.0343	Aromatic alcohol, ester

Go/No-Go Behavior

Prior to photometric recording, mice underwent behavioral shaping, allowing them to learn the mechanics of the go/no-go task. Mice progressed through 5 behavioral shaping stages over the course of 10–14 days as described previously (Quast et al., 2016; Liu et al., 2017). Briefly, mice were water-restricted to no < 85% of their baseline weight for 2 d before shaping. Water was restricted to 40 mL per kg, per day during the restriction period. Mice trained using a go/no-go paradigm in a behavioral chamber with infrared nose pokes (Med Associates Inc.). All mice were first trained to poke their nose into the odor port for at least 300 ms, before moving to the side water port to retrieve water reward within 5 s (**Figure 2**). Water rewards were dispensed at an average volume of 5.0 with a standard deviation of 0.56 μL per Hit trial. After preliminary training sessions (∼30–60 min/d for ∼5–6 d) mice were trained to respond to the S+ odor cue (1% Eugenol in mineral oil) by moving to the water port for a reward and were trained to respond to the S– odor (1% Methylsalicylate in mineral oil) by refraining from poking into the reward port and, instead, initiating a new trial. We required mice to sample odors for at least 100 ms before responding and to respond within 5 s after trial initiation. False alarms (incorrect response to S– odor) caused a 4 s timeout punishment. S+ and S– stimuli (**Table 1**) were presented to the mice in random sequences during training. Mice were trained for 20 trials per block and ∼10–15 blocks per day. Throughout shaping and testing accuracy was calculated by block of 20 trials. Odors pairs were considered "learned" after two consecutive blocks > 85% accuracy (calculated as (*Hits* + *Correct Rejects*)/(*Total Trials*)). After 3–6 d of odor training, the mice performed at over 85% correct responses. Mice were then tested on new odors (**Table 1**) diluted to 1% in mineral oil during photometric recording. For pseudo learning (**Figure 4**), S+ and S– odors were presented randomly, each 50% of the time, as in the go/no-go discrimination task. Reward availability was also randomly determined with rewards available upon reward-port entry 50% of the time.

Photometry

To allow stimulation and recording of fluorescent transients through the same fiberoptic implant, we utilized a fiber photometry system from Doric lenses. Two light emitting diodes (465 and 405 nm wavelength) were coupled to a filter cube by 0.48 na, 400 um core diameter fiber optic cables. The filter cube separated excitation and emission wavelengths, directing the excitation wavelengths along a 0.48 na, 200 um core diameter fiber optic toward the mouse through a rotary connector attached to the behavior box. Emission wavelengths were carried from the mouse to the filter cube along the same fiber, then directed to a femtowatt photodetector (Newport) through a 0.48 na, 600 um core diameter fiber optic cable. Excitation and emission were controlled and recorded, respectively, in Doric Studio software. Both GACh2.0 and GCaMP6M were excited at 465 to record either acetylcholine (for GACh2.0) or calcium binding

(for GCaMP). Additionally, excitation at the isosbestic point for GCaMP (405 nm) generates emission which is insensitive to calcium binding. Thus, a photometric recording of GCaMP with excitation at 405 nm is a useful control for motion artifacts and other calcium-independent noise. For GACh2.0, the isosbestic point is near 405 allowing it to serve as a control signal in a similar manner. To record from the control channel (excited at 405 nm) and the experimental channel (excited at 465 nm) simultaneously, we employed a "locked-in" strategy where each LED was modulated at a different high frequency. Emission resulting from both modes of excitation was recorded by the same photodetector and the signal was demodulated online in Doric Studio to separate the control channel form the experimental channel. Both signals were then converted to df/f and the control channel was subtracted from the experimental channel to reduce noise.

Histology

For immunohistochemistry, mice were deeply anesthetized then transcardially perfused with PBS followed by 4% PFA. Brains were removed and immersion fixed in 4% PFA overnight at 4°C. Brains were transferred to 30% sucrose and allowed to equilibrate, then they were frozen and sectioned at 40 μm on a cryostat (Leica). The sections were washed in 0.3% PBS-T, then incubated in a blocking solution composed of 10% normal goat serum, 0.3% PBS-T, and 3M glycine for 1 h at room temperature or overnight at 4°C. Following blocking, slices were incubated in chicken ∞ GFP primary antibody (1:1,000, Abcam, ab13970) diluted in blocking buffer overnight at 4°C. The next day slices were washed 3× in 0.3% PBS-T then incubated in Goat ∞ Chicken:488 secondary antibody (1:1,000, Invitrogen, A32931) for 2 h at room temperature. Slices were then washed 3× in 0.3% PBS-T with Hoescht included in the middle wash. After the final wash slices were transferred to 0.5× PBS and mounted on glass slides with glycerol-based mounting media (Southern Biotech). Slices were imaged on a Leica SP8 Confocal with 10× air objectives.

Statistics and Data Analysis

For correlations of speed with dF/F, isosbestic-subtracted dF/F traces were compared to motion in the open field experiment. One session was analyzed per mouse. Mice were tracked in open field videos using deep lab cut (Mathis et al., 2018). Using the x and y positions of the mouse output by deep lab cut, speed was calculated as $speed\,(t) = \left(\sqrt{(x_t - x_{t-1})^2 + \left(y_t - y_{t-1}\right)^2}\right) t/\Delta t$ and then aligned to the corresponding isosbestic-subtracted photometry trace. The correlations between speed and photometry traces were calculated for each mouse with a Pearson's correlation. For go/no-go photometry analysis, isosbestic-subtracted dF/F traces were extracted and segmented according to the timing of IR beam breaks during go/no-go behavior using custom MATLAB scripts. Photometry traces for individual trials were separated by trial outcome and averaged within sessions. Importantly, we do not apply trial-to-trial or trial-averaged baseline subtraction or amplitude normalization. Thus, values reported reflect isosbestic-subtracted dF/F. Ninety five percentage of confidence intervals were calculated within sessions using traces from individual trials. For learning-related analyses (**Figure 3**) sessions with 3 or more blocks < 70% accuracy and with 2 or more consecutive blocks > 85% accuracy were sub-selected from the larger dataset. Hit and False Alarm trials from blocks < 70% accuracy were grouped and analyzed separately as "pre-learning" trials. Hit and False Alarm trials from the first two consecutive blocks > 85% accuracy and from subsequent blocks > 85% accuracy were grouped and analyzed separately as "learned" trials. In all cases, post-initiation slopes were calculated by linearly fitting the data after trial initiation before. Areas under the curve were calculated by summing negative values of average traces after trial initiation and dividing by sampling rate. In all cases, comparisons of post-initiation slopes and areas under the curve between trial types utilized a nested, two-way, repeated measures ANOVA. This analysis maintains the relationship between trial types within a single session (repeated measures). Additionally, nesting multiple sessions recorded from the same animal provides a conservative statistical measure which consider all sessions from a single animal together. In the case of post-initiation slopes of GCaMP traces from GABAergic neurons, values were also compared to 0 using a nested one-sample *t*-test. All reported values reflect means from the nested analyses ± SEM and in all cases $p < 0.05$ was considered significant.

DATA AVAILABILITY STATEMENT

The raw data supporting the conclusions of this article will be made available by the authors, without undue reservation.

ETHICS STATEMENT

The animal study was reviewed and approved by Baylor College of Medicine IACUC.

AUTHOR CONTRIBUTIONS

EH designed and conducted experiments, analyzed data, and wrote the manuscript. KB-A conducted experiments, analyzed data, and helped write and edit the manuscript. BA acquired funding, provided guidance on experimental design, data analysis, interpretation, and helped edit the manuscript. All authors contributed to the article and approved the submitted version.

FUNDING

This project was supported by NIH NINDS R01NS078294 (BA) and U01NS111692 (BA), NIH NICHD U54HD083092 (BA), NIH NIDDK R01DK109934 (BA), DOD-PRMP PR180451 (BA), NIH NINDS T32 NS043124-15 (EH), and NIH NIGMS R25 GM 069234 (KB-A).

ACKNOWLEDGMENTS

We would like to thank the Postbaccalaureate Research Education Program (PREP) at Baylor college of

medicine for their support of KB-A, the neurobehavioral core at Baylor College of Medicine for sharing behavioral equipment, and the Arenkiel lab for many helpful discussions.

REFERENCES

Ache, B. W., and Young, J. M. (2005). Olfaction: diverse species, conserved principles. *Neuron* 48, 417–430. doi: 10.1016/j.neuron.2005.10.022

Anaclet, C., Pedersen, N. P., Ferrari, L. L., Venner, A., Bass, C. E., Arrigoni, E., et al. (2015). Basal forebrain control of wakefulness and cortical rhythms. *Nat. Commun.* 6:8744. doi: 10.1038/ncomms9744

Beshel, J., Kopell, N., and Kay, L. M. (2007). Olfactory bulb gamma oscillations are enhanced with task demands. *J. Neurosci.* 27, 8358–8365. doi: 10.1523/JNEUROSCI.1199-07.2007

Böhm, E., Brunert, D., and Rothermel, M. (2020). Input dependent modulation of olfactory bulb activity by HDB GABAergic projections. *Sci. Rep.* 10:10696. doi: 10.1038/s41598-020-67276-z

Buzsaki, G. Y., Bickford, R. G., Ponomareff, G., Thal, L. J., Mandel, R., and Gage, F. H. (1988). Nucleus basalis and thalamic control of neocortical activity in the freely moving rat. *J. Neurosci.* 8, 4007–4026. doi: 10.1523/JNEUROSCI.08-11-04007.1988

Chapuis, J., and Wilson, D. A. (2013). Cholinergic modulation of olfactory pattern separation. *Neurosci. Lett.* 545, 50–53. doi: 10.1016/j.neulet.2013.04.015

Chaudhury, D., Escanilla, O., and Linster, C. (2009). Bulbar acetylcholine enhances neural and perceptual odor discrimination. *J. Neurosci.* 29, 52–60. doi: 10.1523/JNEUROSCI.4036-08.2009

Dannenberg, H., Pabst, M., Braganza, O., Schoch, S., Niediek, J., Bayraktar, M., et al. (2015). Synergy of direct and indirect cholinergic septo-hippocampal pathways coordinates firing in hippocampal networks. *J. Neurosci.* 35, 8394–8410. doi: 10.1523/JNEUROSCI.4460-14.2015

Détári, L., Rasmusson, D. D., and Semba, K. (1999). The role of basal forebrain neurons in tonic and phasic activation of the cerebral cortex. *Prog. Neurobiol.* 58, 249–277. doi: 10.1016/S0301-0082(98)00084-7

Devore, S., Pender-Morris, N., Dean, O., Smith, D., and Linster, C. (2015). Basal forebrain dynamics during nonassociative and associative olfactory learning. *J. Neurophysiol.* 115, 423–433. doi: 10.1152/jn.00572.2015

Fletcher, M. L., and Chen, W. R. (2010). Neural correlates of olfactory learning: critical role of centrifugal neuromodulation. *Learn. Mem.* 17, 561–570. doi: 10.1101/lm.941510

Fletcher, M. L., and Wilson, D. A. (2003). Olfactory bulb mitral-tufted cell plasticity: odorant-specific tuning reflects previous odorant exposure. *J. Neurosci.* 23, 6946–6955. doi: 10.1523/JNEUROSCI.23-17-06946.2003

Ghatpande, A. S., and Gelperin, A. (2009). Presynaptic muscarinic receptors enhance glutamate release at the mitral/tufted to granule cell dendrodendritic synapse in the rat main olfactory bulb. *J. Neurophysiol.* 101, 2052–2061. doi: 10.1152/jn.90734.2008

Gilbert, C. D., and Sigman, M. (2007). Brain states: top-down influences in sensory processing. *Neuron* 54, 677–696. doi: 10.1016/j.neuron.2007.05.019

Goard, M., and Dan, Y. (2009). Basal forebrain activation enhances cortical coding of natural scenes. *Nat. Neurosci.* 12, 1444–1449. doi: 10.1038/nn.2402

Gracia-Llanes, F. J., Crespo, C., Blasco-Ibáñez, J. M., Nacher, J., Varea, E., Rovira-Esteban, L., et al. (2010). GABAergic basal forebrain afferents innervate selectively GABAergic targets in the main olfactory bulb. *Neuroscience* 170, 913–922. doi: 10.1016/j.neuroscience.2010.07.046

Gritton, H. J., Howe, W. M., Mallory, C. S., Hetrick, V. L., Berke, J. D., and Sarter, M. (2016). Cortical cholinergic signaling controls the detection of cues. *Proc. Natl. Acad. Sci. U.S.A.* 113, E1089–E1097. doi: 10.1073/pnas.1516134113

Hangya, B., Ranade, S. P., Lorenc, M., and Kepecs, A. (2015). Central cholinergic neurons are rapidly recruited by reinforcement feedback. *Cell* 162, 1155–1168. doi: 10.1016/j.cell.2015.07.057

Hanson, E., Swanson, J., and Arenkiel, B. R. (2020). GABAergic input from the basal forebrain promotes the survival of adult-born neurons in the mouse olfactory bulb. *Front. Neural. Circuits* 14:17. doi: 10.3389/fncir.2020.00017

Harrison, T. C., Pinto, L., Brock, J. R., and Dan, Y. (2016). Calcium imaging of basal forebrain activity during innate and learned behaviors. *Front. Neural. Circuits* 10:36. doi: 10.3389/fncir.2016.00036

Hasselmo, M. E., and McGaughy, J. (2004). High acetylcholine levels set circuit dynamics for attention and encoding and low acetylcholine levels set dynamics for consolidation. *Prog. Brain Res.* 145, 207–231. doi: 10.1016/S0079-6123(03)45015-2

Herrero, J. L., Roberts, M. J., Delicato, L. S., Gieselmann, M. A., Dayan, P., and Thiele, A. (2008). Acetylcholine contributes through muscarinic receptors to attentional modulation in V1. *Nature* 454, 1110–1114. doi: 10.1038/nature07141

Jing, M., Zhang, P., Wang, G., Feng, J., Mesik, L., Zeng, J., et al. (2018). A genetically encoded fluorescent acetylcholine indicator for *in vitro* and *in vivo* studies. *Nat. Biotechnol.* 36, 726–737. doi: 10.1038/nbt.4184

Jordan, R., Fukunaga, I., Kollo, M., and Schaefer, A. T. (2018). Active sampling state dynamically enhances olfactory bulb odor representation. *Neuron* 98, 1214–1228. doi: 10.1016/j.neuron.2018.05.016

Kay, L. M., and Laurent, G. (1999). Odor-and context-dependent modulation of mitral cell activity in behaving rats. *Nat. Neurosci.* 2, 1003–1009. doi: 10.1038/14801

Kim, T., Thankachan, S., McKenna, J. T., McNally, J. M., Yang, C., Choi, J. H., et al. (2015). Cortically projecting basal forebrain parvalbumin neurons regulate cortical gamma band oscillations. *Proc. Natl. Acad. Sci. U.S.A.* 112, 3535–3540. doi: 10.1073/pnas.1413625112

Kudryavitskaya, E., Marom, E., Pash, D., and Mizrahi, A. (2020). Flexible representations of odour categories in the mouse olfactory bulb. *bioRxiv*. doi: 10.1101/2020.03.21.002006

Laing, D. G. (1986). Identification of single dissimilar odors is achieved by humans with a single sniff. *Physiol. Behav.* 37, 163–170. doi: 10.1016/0031-9384(86)90400-2

Lepousez, G., Nissant, A., Bryant, A. K., Gheusi, G., Greer, C. A., and Lledo, P. M. (2014). Olfactory learning promotes input-specific synaptic plasticity in adult-born neurons. *Proc. Natl. Acad. Sci. U.S.A.* 111, 13984–13989. doi: 10.1073/pnas.1404991111

Lin, S.-C., and Nicolelis, M. A. L. (2008). Neuronal ensemble bursting in the basal forebrain encodes salience irrespective of valence. *Neuron* 59, 138–149. doi: 10.1016/j.neuron.2008.04.031

Liu, G., McClard, C. K., Tepe, B., Swanson, J., Pekarek, B., Panneerselvam, S., et al. (2017). Olfactory cued learning paradigm. *Bio Protoc.* 7:e2251. doi: 10.21769/BioProtoc.2251

Ma, M., and Luo, M. (2012). Optogenetic activation of basal forebrain cholinergic neurons modulates neuronal excitability and sensory responses in the main olfactory bulb. *J. Neurosci.* 32, 10105–10116. doi: 10.1523/JNEUROSCI.0058-12.2012

Mandairon, N., Ferretti, C. J., Stack, C. M., Rubin, D. B., Cleland, T. A., and Linster, C. (2006). Cholinergic modulation in the olfactory bulb influences spontaneous olfactory discrimination in adult rats. *Eur. J. Neurosci.* 24, 3234–3244. doi: 10.1111/j.1460-9568.2006.05212.x

Mandairon, N., and Linster, C. (2009). Odor perception and olfactory bulb plasticity in adult mammals. *J. Neurophysiol.* 101, 2204–2209. doi: 10.1152/jn.00076.2009

Mathis, A., Mamidanna, P., Cury, K. M., Abe, T., Murthy, V. N., Mathis, M. W., et al. (2018). DeepLabCut: markerless pose estimation of user-defined body parts with deep learning. *Nat. Neurosci.* 21, 1281–1289. doi: 10.1038/s41593-018-0209-y

Muir, J. L., Page, K. J., Sirinathsinghji, D. J. S., Robbins, T. W., and Everitt, B. J. (1993). Excitotoxic lesions of basal forebrain cholinergic neurons: effects on learning, memory and attention. *Behav. Brain Res.* 57, 123–131. doi: 10.1016/0166-4328(93)90128-D

Muñoz, W., and Rudy, B. (2014). Spatiotemporal specificity in cholinergic control of neocortical function. *Curr. Opin. Neurobiol.* 26, 149–160. doi: 10.1016/j.conb.2014.02.015

Nunez, A. (1996). Unit activity of rat basal forebrain neurons: relationship to cortical activity. *Neuroscience* 72, 757–766. doi: 10.1016/0306-4522(95)00582-X

Nunez-Parra, A., Maurer, R. K., Krahe, K., Smith, R. S., and Araneda, R. C. (2013). Disruption of centrifugal inhibition to olfactory bulb granule cells impairs olfactory discrimination. *Proc. Natl. Acad. Sci.U.S.A.* 110, 14777–14782. doi: 10.1073/pnas.1310686110

Nunez-Parra, A., Rio, C. D., Christian, A., Huntsman, M. M., and Restrepo, D. (2020). The basal forebrain modulates neuronal response in an active olfactory discrimination task. *Front. Cell. Neurosci.* 14:141. doi: 10.3389/fncel.2020.00141

Ogg, M. C., Ross, J. M., Bendahmane, M., and Fletcher, M. L. (2018). Olfactory bulb acetylcholine release dishabituates odor responses and reinstates odor investigation. *Nat. Commun.* 9:1868. doi: 10.1038/s41467-018-04371-w

Parikh, V., Kozak, R., Martinez, V., and Sarter, M. (2007). Prefrontal acetylcholine release controls cue detection on multiple timescales. *Neuron* 56, 141–154. doi: 10.1016/j.neuron.2007.08.025

Pashkovski, S. L., Iurilli, G., Brann, D., Chicharro, D., Drummey, K., Franks, K., et al. (2020). Structure and flexibility in cortical representations of odour space. *Nature* 583, 253–258. doi: 10.1038/s41586-020-2451-1

Pinto, L., Goard, M. J., Estandian, D., Xu, M., Kwan, A. C., Lee, S. H., et al. (2013). Fast modulation of visual perception by basal forebrain cholinergic neurons. *Nat. Neurosci.* 16, 1857–1863. doi: 10.1038/nn.3552

Quast, K. B., Ung, K., Froudarakis, E., Huang, L., Herman, I., Addison, A. P., et al. (2016). Developmental broadening of inhibitory sensory maps. *Nat. Neurosci.* 20, 189–199. doi: 10.1038/nn.4467

Restrepo, D., Doucette, W., Whitesell, J. D., McTavish, T. S., and Salcedo, E. (2009). From the top down: flexible reading of a fragmented odor map. *Trends Neurosci.* 32, 525–531. doi: 10.1016/j.tins.2009.06.001

Rinberg, D., Koulakov, A., and Gelperin, A. (2006). Speed-accuracy tradeoff in olfaction. *Neuron* 51, 351–358. doi: 10.1016/j.neuron.2006.07.013

Rokni, D., Hemmelder, V., Kapoor, V., and Murthy, V. N. (2014). An olfactory cocktail party: figure-ground segregation of odorants in rodents. *Nat. Neurosci.* 17, 1225–1232. doi: 10.1038/nn.3775

Rothermel, M., Carey, R. M., Puche, A., Shipley, M. T., and Wachowiak, M. (2014). Cholinergic inputs from Basal forebrain add an excitatory bias to odor coding in the olfactory bulb. *J. Neurosci.* 34, 4654–4664. doi: 10.1523/JNEUROSCI.5026-13.2014

Sanz Diez, A., Najac, M., and De Saint Jan, D. (2019). Basal forebrain GABAergic innervation of olfactory bulb periglomerular interneurons. *J. Physiol.* 597, 2547–2563. doi: 10.1113/JP277811

Sarter, M., and Bruno, J. P. (1999). Cortical cholinergic inputs mediating arousal, attentional processing and dreaming: differential afferent regulation of the basal forebrain by telencephalic and brainstem afferents. *Neuroscience* 95, 933–952. doi: 10.1016/S0306-4522(99)00487-X

Szymusiak, R. (1995). Magnocellular nuclei of the basal forebrain: substrates of sleep and arousal regulation. *Sleep* 18, 478–500. doi: 10.1093/sleep/18.6.478

Szymusiak, R., Alam, N., and McGinty, D. (2000). Discharge patterns of neurons in cholinergic regions of the basal forebrain during waking and sleep. *Behav. Brain Res.* 115, 171–182. doi: 10.1016/S0166-4328(00)00257-6

Tremblay, L., Hollerman, J. R., and Schultz, W. (1998). Modifications of reward expectation-related neuronal activity during learning in primate striatum. *J. Neurophysiol.* 80, 964–977. doi: 10.1152/jn.1998.80.2.964

Verhagen, J. V., Wesson, D. W., Netoff, T. I., White, J. A., and Wachowiak, M. (2007). Sniffing controls an adaptive filter of sensory input to the olfactory bulb. *Nat. Neurosci.* 10, 631–639. doi: 10.1038/nn1892

Villar, P. S., Hu, R., and Araneda, R. C. (2020). Long-range GABAergic inhibition modulates spatiotemporal dynamics of the output neurons in the olfactory bulb. *bioRxiv*. doi: 10.1101/2020.07.08.194324

Voytko, M., Lou, O. D. S., Richardson, R. T., Gorman, L. K., Tobin, J. R., and Price, D. L. (1994). Basal forebrain lesions in monkeys disrupt attention but not learning and memory [published erratum appears in J Neurosci 1995 Mar; 15 (3): following table of contents]. *J. Neurosci.* 14, 167–186. doi: 10.1523/JNEUROSCI.14-01-00167.1994

Xu, M., Chung, S., Zhang, S., Zhong, P., Ma, C., Chang, W. C., et al. (2015). Basal forebrain circuit for sleep-wake control. *Nat. Neurosci.* 18, 1641–1647. doi: 10.1038/nn.4143

Yang, C., McKenna, J. T., Zant, J. C., Winston, S., Basheer, R., and Brown, R. E. (2014). Cholinergic neurons excite cortically projecting basal forebrain GABAergic neurons. *J. Neurosci.* 34, 2832–2844. doi: 10.1523/JNEUROSCI.3235-13.2014

Zaborszky, L., Carlsen, J., Brashear, H. R., and Heimer, L. (1986). Cholinergic and GABAergic afferents to the olfactory bulb in the rat with special emphasis on the projection neurons in the nucleus of the horizontal limb of the diagonal band. *J. Comp. Neurol.* 243, 488–509. doi: 10.1002/cne.902430405

Zant, J. C., Kim, T., Prokai, L., Szarka, S., McNally, J., McKenna, J. T., et al. (2016). Cholinergic neurons in the basal forebrain promote wakefulness by actions on neighboring non-cholinergic neurons: an opto-dialysis study. *J. Neurosci.* 36, 2057–2067. doi: 10.1523/JNEUROSCI.3318-15.2016

Zhan, X., Yin, P., and Heinbockel, T. (2013). The basal forebrain modulates spontaneous activity of principal cells in the main olfactory bulb of anesthetized mice. *Front. Neural. Circuits* 7:148. doi: 10.3389/fncir.2013.00148

Conflict of Interest: The authors declare that the research was conducted in the absence of any commercial or financial relationships that could be construed as a potential conflict of interest.

Copyright © 2021 Hanson, Brandel-Ankrapp and Arenkiel. This is an open-access article distributed under the terms of the Creative Commons Attribution License (CC BY). The use, distribution or reproduction in other forums is permitted, provided the original author(s) and the copyright owner(s) are credited and that the original publication in this journal is cited, in accordance with accepted academic practice. No use, distribution or reproduction is permitted which does not comply with these terms.